MASTERARBEIT | MASTER'S THESIS

Titel | Title

Characterising the South Atlantic Anomaly via cosmic ray mapping using CHEOPS

verfasst von | submitted by

Luise Janett Pevestorff BSc

angestrebter akademischer Grad | in partial fulfilment of the requirements for the degree of

Master of Science (MSc)

Wien | Vienna, 2025

Studienkennzahl lt. Studienblatt | Degree programme code as it appears on the student record sheet:	UA 066 861
Studienrichtung lt. Studienblatt | Degree programme as it appears on the student record sheet:	Masterstudium Astronomie
Betreut von | Supervisor:	Univ.-Prof. Mag. Dr. Franz Kerschbaum
Mitbetreut von | Co-Supervisor:	Mag. Dr. Roland Ottensamer

Abstract German

Weltraumteleskope sammeln kontinuierlich große Mengen astrophysikalischer Daten. Diese Missionen sind auf die Aufnahme spezifischer wissenschaftlicher Daten spezialisiert, es bleiben begleitende Datensätze oftmals ungenutzt. Der CHaracterizing ExOPlanet Satellite (CHEOPS) der ESA beobachtet Exoplaneten Transits um helle Sterne und ist aufgrund seiner erdnahen Umlaufbahn gelegentlich erhöhter kosmischer Strahlung ausgesetzt, die mit der bordeigenen Datenverarbeitung korrigiert wird. Diese Thesis nutzt in den Rohdaten auftretende Auswirkungen der kosmischen Strahlung, um Veränderungen der Ausdehnung und Lage der South Atlantic Anomaly (SAA), sowie den Polarlichtzonen zu untersuchen. Dafür wurde eine eigene Datenverarbeitungspipeline entwickelt, mit der die einfallende kosmische Strahlung in einem Zeitraum von 4.5 Jahren identifiziert werden kann. Die Pipeline umfasst Vorverarbeitungsschritte wie z.B. Bias-Korrektur, Derotation, Hintergrundkorrektur und Maskierung der sich im Bild befindlichen Sterne. Die Anzahl und Dichte der kosmischen Strahlen sowie der prozentuale Anteil von kosmischer Strahlung betroffener Pixel wurden berechnet und kartografiert. Auf Basis der kartografierten Daten erfolgte eine auf den äußeren Konturen der Anomalien, basierte Analyse, um zeitliche Veränderungen bestimmen zu können. Darüber hinaus wurde ein möglicher Zusammenhang zwischen der Dichte der kosmischen Strahlen und der Sonnenaktivität analysiert. Die Ergebnisse zeigen, dass sich die Ausdehnung der SAA und der Polarlichtzonen im Beobachtungszeitraum von 4,5 Jahren verkleinert. Diese unerwartete Beobachtung könnte mit der im selben Zeitraum stetig gestiegenen Sonnenaktivität in Verbindung stehen. Zudem wurden Lageveränderungen aller drei Regionen festgestellt: Beide Polarlichtzonen verlagerten sich in Richtung des Äquators, während sich die SAA entgegen früherer Langzeitstudien, die eine nordwestliche Drift berichten, in südöstlicher Richtung verschob. Eine positive Korrelation zwischen Sonnenaktivität und der durchschnittlichen Dichte der kosmischen Strahlung wurde ebenfalls beobachtet, insbesondere nach Phasen erhöhter geomagnetischer Aktivität.

Abstract English

Space-based observatories continuously collect vast amounts of astrophysical data. While these missions are optimised for specific scientific goals, ancillary data products are often underused. ESA's CHaracterizing ExOPlanet Satellite (CHEOPS) observes transit light-curves of exoplanets around bright stars. Due to its position in Low Earth Orbit (LEO), the satellite is exposed to cosmic rays, which are corrected for in the onboard data processing pipeline. This thesis utilises the incidental cosmic ray hits that are present in the raw data to investigate temporal variations in size and location of the South Atlantic Anomaly (SAA) and the auroral zones. By developing a dedicated data processing pipeline, cosmic ray hits were identified in CHEOPS' raw data spanning 4.5 years of data acquisition. The pipeline includes preprocessing steps such as bias correction, derotation, background normalisation, and star masking. The number of cosmic rays, the density of cosmic rays as well as the percentage of pixels affected by cosmic rays were calculated across geospatial bins to construct maps of these properties. Subsequently, contour-based analysis was used to determine the boundaries of the regions and track changes over time. Furthermore, possible correlations between the density of cosmic rays and solar activity were investigated. The analysis reveals that both the SAA and auroral zones have decreased in size over the 4.5-year period. This unexpected finding may be linked to increasing solar activity over the 4.5 years of data. Moreover, all three regions exhibit location drifts: both auroral zones drift toward the equator, and the SAA moves southeast, in contrast to previous long-term studies that report a northwest drift. A positive correlation between solar activity and mean cosmic ray density was also observed, particularly following periods of heightened geomagnetic activity.

Acknowledgements

First and foremost, I want to thank Alexis Heitzmann for collaborating with me, providing continuous support, feedback and great discussions to bring this wonderful project to life.

Secondly, I want to thank Franz Kerschbaum and Roland Ottensamer for the ideas and inputs throughout this endeavour, as well as providing me with the opportunity to work on this project.

I am beyond grateful for the unwavering support from my partner Philip who provided additional feedback, editing help and encouragement throughout this process.

Last but not least, I want to thank my family and friends, for always standing by my side and having my back.

Thank You!

Contents

List of Tables

List of Figures

Listings

1. Introduction

Ever since the first space telescope, NASA's Orbiting Astronomical Observatory, was launched in 1966, vast amounts of data on various astrophysical phenomena have been acquired continuously. As space telescopes are optimised to obtain the specific data matching their scientific purpose, other data byproducts are often overlooked. The CHEOPS satellite has been acquiring data since its launch in December 2019, observing more than 100 exoplanets in the process ([Fortier, A. et al., 2024]). CHEOPS' primary data product are transit light curves of such exoplanets around bright stars (Gmag < 12).

CHEOPS's orbit subjects it to a large amount of cosmic rays. During nominal science operation, the internal data processing pipeline applies a cosmic ray correction to the images to ensure high quality photometric data. Thus, cosmic rays hitting the detector occur as a data byproduct. However, this frequently discarded data, can be repurposed for scientific analysis due to the satellite's continuous data acquisition. Specifically, the presence of cosmic rays in the raw CHEOPS data enables their distribution to be mapped over a 4.5-year period. The satellite's orbital period of 99 minutes leads to CHEOPS passing through the South Atlantic Anomaly (SAA), an anomaly in earth's magnetic field, approximately 10 times per day. During the SAA passages, the high radiation environment leads to an increase in cosmic ray detections.

This thesis aims to investigate if anomalies in the Earth's magnetic field as e.g. the South Atlantic Anomaly (SAA) can be characterised using the cosmic rays accidentally detected by CHEOPS and how these anomalies change over time. As part of this thesis, a data processing pipeline was developed to detect the cosmic rays inside the satellites' raw images. These detected cosmic rays are subsequently analysed to answer the scientific questions if and how the SAA and auroral zones are changing in size and location over time, as well as how the solar cycle plays a role in the occurrences of cosmic ray hits.

1.1. Structure of this Document

This thesis is structured as follows: Chapter 1 provides an overview of the research topic and outlines the key contributions of the project. Background information on the CHEOPS satellite, cosmic rays and the earth's magnetic field is given in Chapter 2. The following Chapter 3, details the structure and inner workings of the data processing pipeline as well as the functionality of the analysis routines.

This methodology is divided into the sections of the data processing procedure (Section 3.1) consisting of multiple different steps from the raw image to detected cosmic rays and the applied techniques necessary for analysing the data to characterise the regions of interest (Section 3.2). Chapter 4 presents the results and findings of the data analysis regarding the different research questions. Sections 4.1 and 4.2 detail the findings regarding a change in size and location of the SAA and the auroral zones. The subsequent Chapter 5 discusses and evaluates the aforementioned results. The last chapter, Chapter 6, summarizes the findings of this thesis as well as provides an outlook on future developments regarding the project.

1.2. Contributions

This thesis project was conducted in cooperation with the CHEOPS science team from the University of Geneva. The development of the data processing pipeline as well as the analysis of the results was done in close collaboration with Dr. Alexis Heitzmann. Dr. Heitzmann and myself have developed and designed most of the pipeline as well as analysis techniques in tandem. The process involved working together on the software development, where generally a specific function or part of the pipeline was developed by one of us, subsequently consecutively tested and modified by both. However, there are parts of the code developed individually. To fairly highlight the contributions made by each of us, footnote marks will indicate if a specific function or part of the pipeline was developed individually or if both of us were involved in the development process. The following footnote marks will be used to indicate contributions in alphabetical order: [1]A. Heitzmann, [2]L. Pevestorff, [3]both. This project was published on GitHub under the name CheopsCosmics ([Heitzmann and Pevestorff, 2025]).

2. Background and Theory

2.1. CHEOPS Mission

The CHaracterizing ExOPlanet Satellite (CHEOPS) is a small class ESA mission launched on 18th December 2019 from Kourou, French Guinea, tasked to characterise exoplanet transits using ultra-high precision photometry on bright stars known to host exoplanets ([Benz et al., 2020]).

2.1.1. Spacecraft

The spacecraft features a single instrument, a high-precision photometer connected to a single 300 mm effective aperture telescope with a single Charged Coupled Device (CCD) detector (see Figure 2.1). The CCD covers a wavelength range of 750 nm reaching from visible (350 nm) to near-infrared (1100 nm) wavelengths ([Benz et al., 2020]).

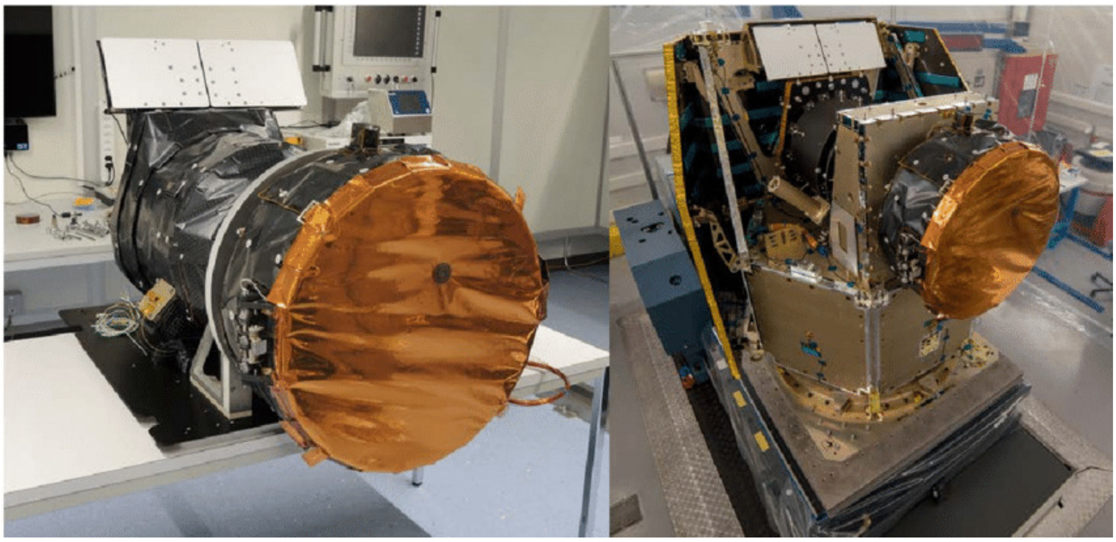

Figure 2.1.: The CHEOPS instrument on its own (left) and integrated onto the satellite (right). Taken from [Beck et al., 2017]. Courtesy of the University of Bern and ADS Spain.

2.1.2. CHEOPS Orbit

The satellite is designed to operate nadir locked in a polar Low Earth Orbit (LEO) at an altitude of ∼700 km. This provides access to a wide range of targets across the sky and a fast data downlink to ground stations. CHEOPS' operates in a dawn-dusk Sun-synchronous orbit at an inclination of ∼98°. Advantages of a dawn-dusk Sun-synchronous orbit include constant lighting condition for the satellite's solar panels and a stable thermal environment as well reduced stray light contamination from the Earth's surface and atmosphere.

2.1.2.1. Mission Design

The CHEOPS mission is the first small class mission of ESA's *Cosmic Vision: Space Science for Europe 2015 - 2025* campaign and was originally designed to operate for 3.5 years with possible extensions to 5 years ([Benz et al., 2020]). As of March 7 2023 the mission has been extended to 2026 with another possible extension until 2029 ([University of Geneva and University of Bern, 2023]). Using a monopropellant propulsion unit, the satellite is able to perform collision avoidance maneuvers. The monopropellant propulsion unit enables the spacecraft to re-enter Earth's atmosphere 25 years after decomissioning ([Benz et al., 2020]).

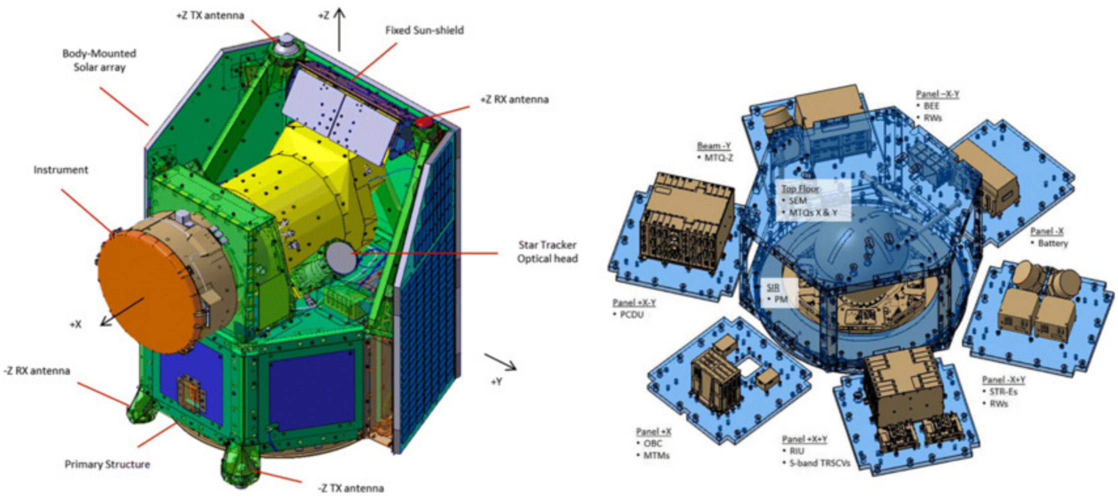

Figure 2.2.: The configuration of the CHEOPS spacecraft with the units housed on the platform. Taken from [Asquier et al., 2015]. Courtesy of ADS Spain.

2.1.2.2. Spacecraft Design

The spacecraft consists of a hexagonal prismatic shaped compact platform body on which solar arrays are mounted. In its entirety the spacecraft has a mass of approximately 275 kg according to [Benz et al., 2020] with dimensions of 1.5 × 1.5 × 1.5 m. The satellite is equipped with a singular telescope (see Sections 2.1.3 and 2.1.3.1) which is split into four different units (see Section 2.1.3. As depicted in Figure 2.2, the hexagonal platform houses two of the four units alsongside the key avionic units and the propulsion module. The two remaining units as well as the star trackers and sun shield are mounted outside the platform ([Asquier et al., 2015]).

The satellite uses its only instrument as a fine guidance sensor with a required pointing stability of 4" RMS over 48 h. As mentioned in [Benz et al., 2020], during operations the Line Of Sight (LOS) aligns with the apparent position of the target star and stays stable while the platform rotates around it in order to maintain thermal balance. In order to facilitate thermal balance, the instrument radiators are directed towards deep space, to receive as little thermal radiation as possible. Energy is supplied by three solar arrays, two lateral panels and one central panel with a total area of 2.5 m^2 permanently facing the sun.

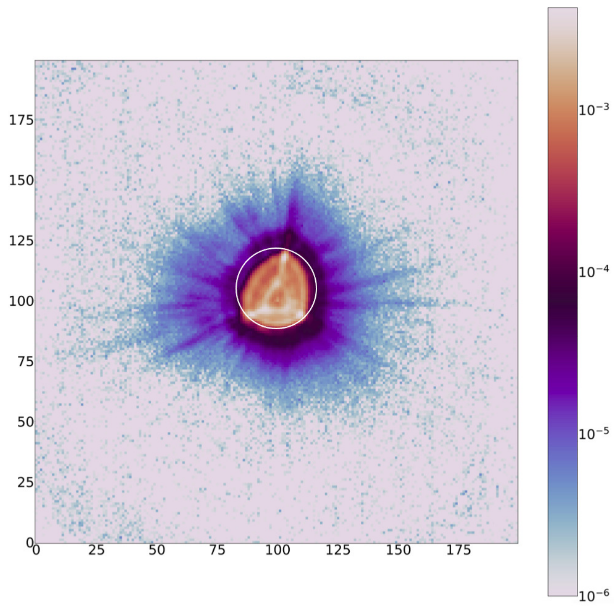

Figure 2.3.: CHEOPS's de-focussed PSF corresponding to a target star in the centre of the CCD. Inside the white circle, 90% of the energy is concentrated, corresponding to a radius of $R = 16.5$ px. Taken from [Fortier, A. et al., 2024].

2.1.3. Instrumentation and Payload

CHEOPS's only payload on the spacecraft platform is an on-axis 335 mm diameter Ritchey-Chrétien telescope, with a 300 mm clear aperture, leading to an effective collecting are of $76,793$ mm^2 and a field of view of 0.32°. The nature of CHEOPS's Low Earth Orbit (LEO) leads to a need to mitigate stray light. In order to ensure the quality of the data the telescope is fitted with baffles. However as stra light cannot be omitted completely, low levels of stray light are corrected for in the Data Reduction Pipeline (DRP).

At higher levels of stray light, above a certain treshold the images are discarded immediately and not downlinked. The Point Spread Function (PSF) of the star is purposely de-focused on the focal plane to reduce pixel to pixel variations (see Figure 2.3). The size of the PSF is defined by the radius of the circle enclosing 90% of the energy from the target star that is received on the CCD. According to [Hoyer, S. et al., 2020], the DRP generates four different lightcurves measured through different apertures.

The first three apertures have a pre-defined radii of 26, 33 and 39 pixels, while the fourth one corresponds to a radius minimising the signal to noise ratio. The user is subsequently able to choose the most appropriate aperture for the dataset. The singular instrument on the spacecraft is a high-precision photometer, operating in the visible and near-infrared range of the electromagnetic spectrum ($0.4\mu m$ to $1.1\mu m$). As mentioned in Section 2.1.2.2, the photometer consists of four separate units:

- Optical Telescope Assembly (OTA)
- Baffle and Cover Assembly (BCA)
- Sensor Electronics Module (SEM)
- Back End Electronics (BEE)

2.1.3.1. Optical Telescope Assembly

The OTA features the optical telescope set-up, as well as the detector and the read-out electronics. Along with the telescope, the Back End Optics (BEO) is part of the optical configuration mounted on a stiff optical bench defining the interface to the platform. The BEO re-images the focal plane of the telescope on the detector, providing an intermediate pupil with a pupil mask to reject stray-light. It also enlarges the final effective focal length of the telescope to 2681 mm (F/8.38) at the nominal wavelength of 750 nm. As mentioned above, the telescope has a field of view of 0.32° full cone, which translates into a $1^{"}/px$ plate scale on the detector with $13\mu m$ pixel run in AIMO.

As seen in Figure 2.5the CCD is hosted on the FPM alongside the readout analogue and digital electronics. As seen in Figure 2.4 the CCD has an image capture area of 1024 × 1024 pixels, with the covered margins of the full frame image being 1076 columns and 1033 rows. Along the side margins of the CCD 16 covered columns of dark pixels and eight columns of blank pixels can be found on either side. In addition, four virtual overscan pixel columns are present on the opposite side of the output amplifier, in this case on the left side, which are generated by four additional shift-read cycles. Along the top margin, three rows of dark pixels and six rows of overscan pixels are present.

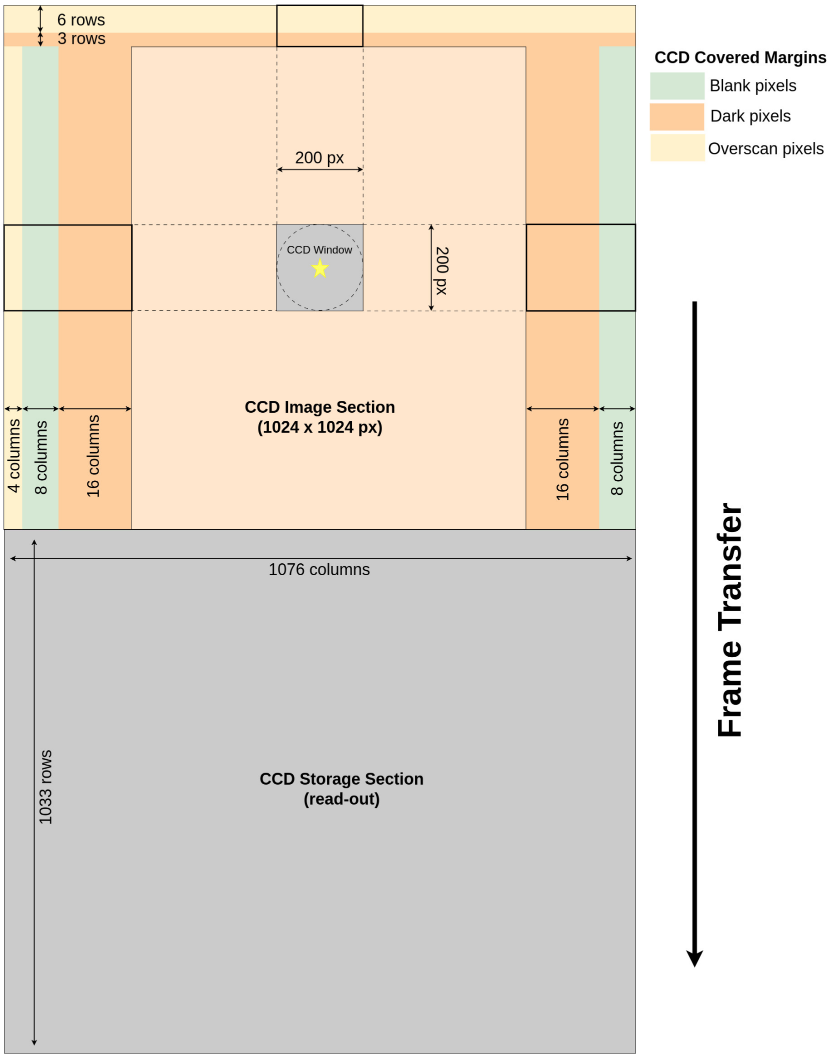

Figure 2.4.: Schematic of the CHEOPS CCD. Image taken from [Benz et al., 2020].

The CCD (as depicted in Figure 2.4) has an image section of 1024 × 1024 pixels. According to [Benz et al., 2020] it is not possible to downlink the full frame image due to restricted telemetry and bandwidth. Therefore, a 200 × 200 pixel window, henceforth referred to as SubArray, centred around the target star plus the covered margins, is cropped out of the full-frame image. The on-board processing software further crops the image to save additional bandwidth. This SubArray is subsequently linked down.

In the case of long exposure images, shorter exposure images are co-added. These co-added SubArrays are afterwards linked down alongside images of a 30 px radius circle around the target, called imagettes. An important property of any CCD is the gain, which, according to [Benz et al., 2020] is defined as "the ratio between the number of electrons per pixel and the number of counts per pixel". The gain of CHEOPS' CCD is 0.5111 ([Hoyer, S. et al., 2020]).

2.1.3.2. Baffle and Cover Assembly

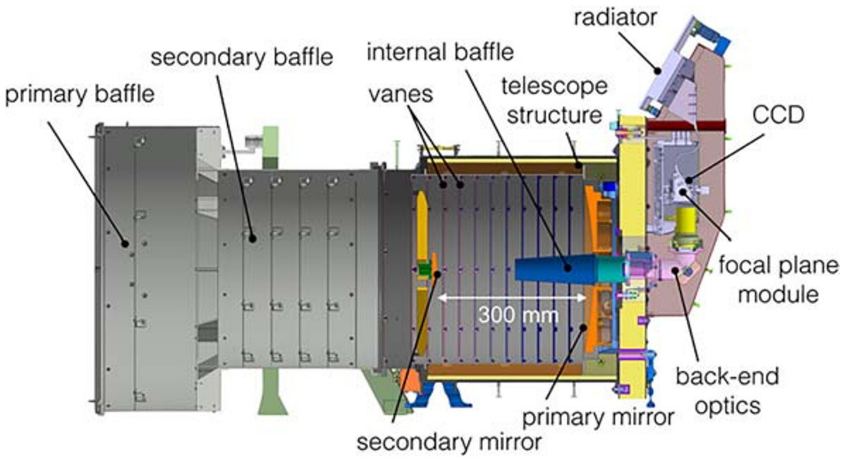

Figure 2.5.: Schematic of CHEOPS' OTA and BCA. Image taken from [Benz et al., 2020].

The OTA and BCA are depicted in Figure 2.5. The BCA is the second unit mounted on the outside on top of the platform. It is mechanically separated from the OTA and a key component of the straylight mitigation tactics. As described in [Benz et al., 2020], the design for the baffle has been adapted from the COnvection, ROtation and planetary Transits (CoRoT) satellite to fit CHEOPS's size and on-axis design. It is constructed out of a cylindrical aluminium tube with circular vanes (see Figure 2.5) and a black coating to mitigate stray light at an angle $> 35°$ with respect to the optical axis. Over all, the baffle system is able to reject stray light between 10^{-10} and 10^{-12} depending on the incident angle.

2.1.3.3. Sensor Electronics Module

The SEM is one of the units located inside the platform and is responsible for the controls of the focal plane. The overall heat load on the telescope is minimised as a result of the SEM being physically decoupled from the FPM. Inside the SEM the Sensor Control Unit as well as the Power Conditioning Unit are housed, interfacing the Back End Electronics (BEE).

As CHEOPS is equipped with a high-precision photometer, the gain of the CCD requires to stay stable persistently. Therefore, the temperature and voltage of the CCD have to remain stable, since these two characteristics are responsible for the gain sensitivity.

2.1.3.4. Back End Electronics

The BEE acts as the main computer of the spacecraft. As described in [Benz et al., 2020] it is responsible for providing power to the payload and data interfaces. The BEE is connected to the SEM, providing power to both itself and the SEM. It contains a data processing unit and a distribution unit interfacing with the SEM as previously suggested. Apart from hosting the In-Flight Software (IFSW), responsible for controlling the SEM and FPM, the BEE performs data handling, centroiding of the image and on-board data processing.

2.1.4. Software

As previously mentioned the BEE handles the IFSW. During an observational run, several computational steps are performed by both the IFSW and the SEM ([Benz et al., 2020]).

2.1.4.1. Nominal Observation

In nominal observation mode, the IFSW will consistently perform the same procedure: Once the CCD is stabilised and paired with the front-end electronics, the computer is updated with parameters for the specific observation and the satellite is pointed in the direction of the targeted star ([Benz et al., 2020]).

The first step of the procedure is the target acquisition. Here, the instrument will gather several full-frame images with the goal of identifying all the stars in the region and will use pattern matching to correct the pointing of the satellite. After the target acquisition is completed, a calibration frame is taken. Once the calibration frame has been obtained, the actual science observation commences. In this so called "window mode" the telescope takes images of a predefined exposure time.

2.1.4.2. On-board Science Data Processing

Once the data has been acquired, CHEOPS on-board science data processing procedure starts to prepare the data for downlinking. First, the full frame images are cropped into 200×200 pixel images with the target star in the centre, as mentioned in Section 2.1.3.1. These SubArrays are now either directly downlinked if the exposure time is 30 seconds or longer, or have to be further reduced if the exposure time is shorter than 30 seconds. In the latter case the individual images are stacked, up to a total exposure time of 60 seconds, by co-adding pixel by pixel. As mentioned in Section 2.1.3.1 circular imagettes with a radius of 30 pixels are downlinked alongside the stacked images. These imagettes enable different corrections inside the PSF. If no stacking is performed, imagettes are not necessary and therefore not obtained. Regardless of exposure time, the CCD margins are cropped, stacked if necessary, and also downlinked.

2.1.5. Science Goals

The CHEOPS Science Team assembled a number of scientific objectives with the aim of exploring the diversity in planetary systems as well as helping facilitate a better understanding of planet formation and evolution (see [Benz et al., 2020]). As a result multiple different scientific objectives have been formulated by [Benz et al., 2020] to encompass a variety of different scientific topics:

- Search for exoplanet transits.
- Determination of the mass-radius relationships of planets with a small radius and/or mass.
- Exploration of the architecture of planetary systems hosting small planets in long-period orbits.
- Study dust clumps in edge-on debris disks around young stars.
- Detection of new planetary systems, focussing on multi-planet systems and systems hosting hot Jupiters, around bright stars.
- Enlargement of the parameter space of planets and host stars, emphasizing on hot stars.
- Discern planet migration scenarios using Transit-Time Variation (TTV).
- Search for exo-Trojans.
- Characterisation of exoplanet atmospheres.

Since the mission extension, the science team has voiced the additional possibility to use CHEOPS for the search of exomoons ([University of Geneva and University of Bern, 2023]).

2.2. Cosmic Rays

Cosmic rays are high energy particles travelling through space at near light speed. There are two types of comic rays, commonly known as primary- and secondary cosmic rays respectively. Possible origins of primary cosmic rays include the Sun, stars outside the Solar System, as well as sources outside the Milky Way, e.g. active galactic nuclei. Cosmic rays are mostly deflected by the Earth's atmosphere and magnetic field, but cosmic ray patricles can interact with particles in the atmosphere, creating a shower of secondary particles able to reach the surface [Spatschek, 2018].

2.2.1. Properties

99% of the cosmic rays originating from outside the Earth's atmosphere are nuclei of common atoms, missing their electron shells. Most of the nuclei (90%) are hydrogen nuclei, 9% are alpha particles, identical to helium-4 nuclei and 1% are HZE ions, which are the nuclei of heavier atoms, where elements up to the actinoid series have been detected. The remaining 1% are solitary electrons, whereas a minute fraction are stable antimatter particles such as positrons and antiprotons [Spatschek, 2018].

Primary cosmic rays can have a variety of origins, the most common being protons originating from the sun after solar energetic particle events caused by coronal mass ejections or solar flares. Others can originate from stars inside or outside the galaxy, accelerated by supernovae. As they travel with a velocity close to light speed and get deflected by magnetic fields of any kind, cosmic rays reach Earth isotropically. Therefore any information about their origins have to be derived from other properties such as energy spectrum and elemental composition [Spatschek, 2018].

2.2.2. Physics

As depicted in Figure 2.6 the kinetic energy of cosmic rays can vary between 1 MeV and 1 EeV depending on the mass and speed of the particle. As seen in the figure low-energy particles make up a large portion of the detected cosmic ray events, whereas particles with increasingly high energies are rare and detections sparse. Once primary cosmic rays enter Earth's atmosphere, interactions with atoms and molecules inside the atmosphere lead the primary cosmic ray to undergo spallation and other nuclear reactions. These processes trigger a cascade of reactions inside the atmosphere, called an air shower.The end product being a secondary cosmic ray. Depending on the primary cosmic ray, the secondary is either a photon, hadron or lepton.

The exact type varies with atmospheric altitude where protons are more abundant in altitudes above 5 km, whereas muons are more abundant at sea level. Other particles such as electrons, positrons, neutrons and pions are also present but their amount is negligible compared to protons and muons.

The above mentioned processes are also possible to occur when the primary cosmic ray interacts with the interstellar medium. [Bonomi et al., 2020] [Becker Tjus and Merten, 2020].

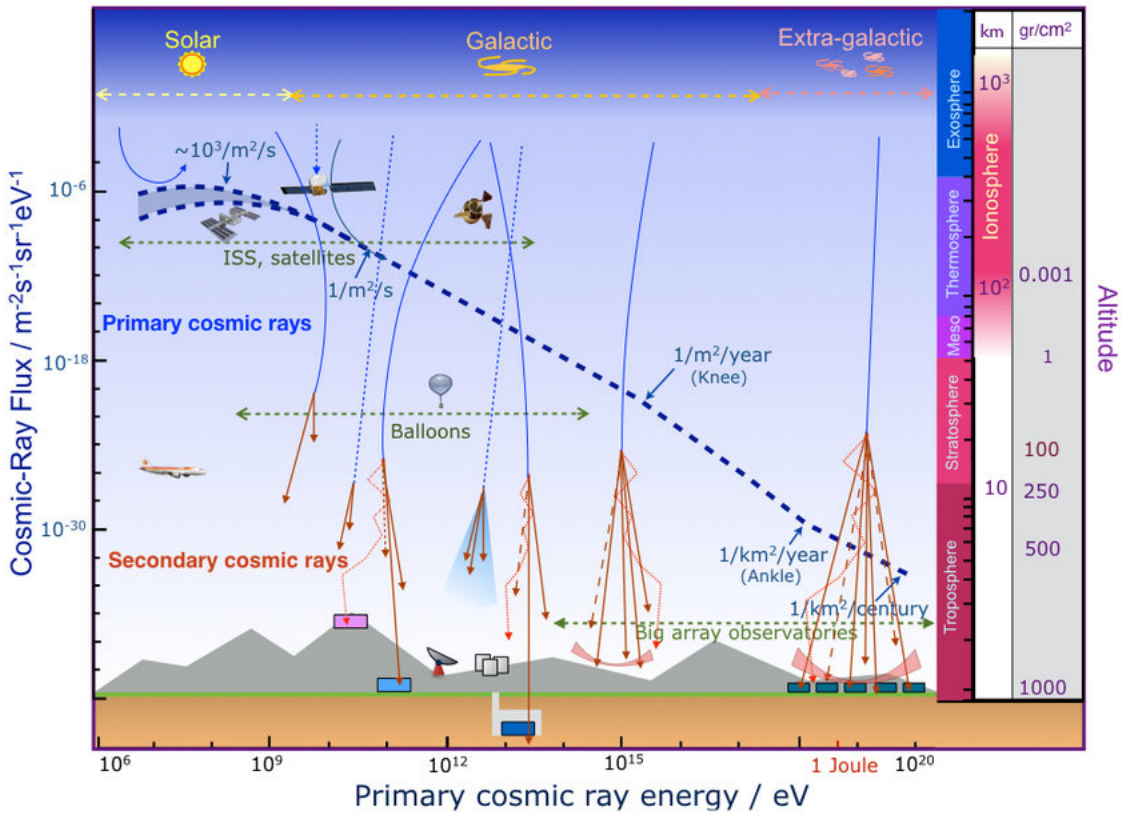

Figure 2.6.: Spectrum of primary cosmic rays as a function of the cosmic ray energy. The dashed blue line shows the flux of the cosmic rays. The layers of the atmosphere as well as air pressure are shown on the right vertical axes. Image taken from [Garzon et al., 2017].

When galactic or extragalactic cosmic rays enter the solar system, they interact with the heliosphere. As cosmic rays get deflected by magnetic fields the intensity of cosmic rays changes with two cycles related to the sun, the 27-day synodic solar rotation cycle and the 11-year solar cycle. The number and intensity of galactic and extragalactic cosmic rays is antiproportional to the 11-year solar cycle. During periods of high solar activity the heliosphere's influence on cosmic rays originating outside the solar system is large, with the result of fewer of these particles entering the solar system. This phenomenon known as "Forbush decrease" is observed mainly after a coronal mass ejection and closely follows the 11-year solar cycle. Due to higher solar activity, more solar flares and coronal mass ejections are taking place. Similarly more solar energetic particle events are happening which result in an an increase of solar cosmic rays in the heliosphere ([Hanslmeier, 2020], [Freiherr von Forstner, Johan L. et al., 2021]).

2.2.3. Detection

Cosmic rays can be detected directly or indirectly in space, high altitude and with ground-based observatories. Primary cosmic rays can be directly detected by different kinds of particle detectors on satellites, spacecrafts or high-altitude balloons, while secondary cosmic rays can be indirectly detected using various ground based methods. On the ground the Pierre-Auger-Observatory in Malargüe, Argentina uses its hybrid design to efficiently detect ultra-high-energy cosmic rays. Here fluorescence telescopes as well as surface detectors are able to simultaneously measure cosmic ray air showers using the Cherenkow effect, providing the ability for cross checks and redundancies [Dawson, 2007].

In space the Alpha Magnetic Spectrometer (AMS-02), mounted on the International Space Station (ISS) is a large acceptance particle physics detector tasked with measuring charge, energy and momentum of particles and nuclei to help the understanding of antimatter, dark matter and the origin of cosmic rays. It is a multipurpose spectrometer consisting of a permanent magnet measuring the momentum of the particle/nucleus and an array of particle detectors used to determine the charge and energy of different particles and nuclei. Over the course of 8.5 years the AMS-02 has recorded more than $24 \cdot 10^9$ cosmic ray events [Ting, 2013].

2.3. Earths Magnetic Field

Earth's magnetic field, also known as "geomagnetic field", is generated by a variety of sources both above and below the Earth's surface. The most important and main source is the geomagnetic dynamo, generated inside the Earth's core. The Earth's core is made up of a spherical solid iron inner core which is surrounded by a liquid iron outer core ([McPherron,]).

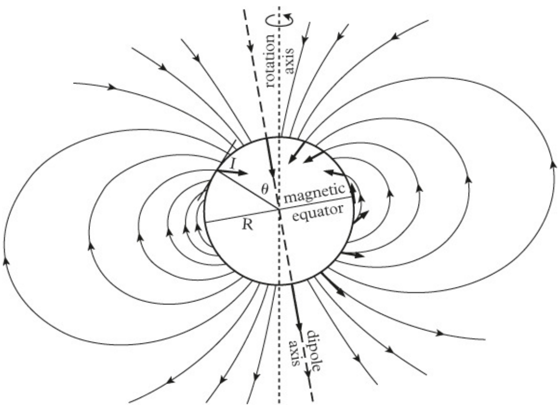

Figure 2.7.: Earth as a magnetic dipole with a tilted dipole axis. The field lines enter in the northern hemisphere and exit in the southern hemisphere. The angles θ and I describe the magnetic coalitude of a position on the surface and the inclination of the field at said position respectively. Taken from [Lowrie, 2023].

The geomagnetic dynamo is produced by the convective flow of the conducting liquid iron, which due to buoyancy forces transports heat radially outward from the inner core. The rotation of Earth produces Coriolis forces perpendicular to the initial flow direction, twisting the initial magnetic field. These forces mould the flow lines into thin columns parallel to the rotation axis, with the fluid inside moving in spiral-like motions. Each columns helicity is opposite to the adjacent columns changing pitch and direction at the equator. An imaginary cylinder (tangent cylinder) with its axis along the rotational axis and radius equal to the inner core can be constructed, touching the inner core at the equator and low magnetic flux on the inside.

The spiral-like motions of the conducting fluid iron inside the other columns twist the magnetic field lines. They subsequently break and reconnect, producing toroidal and poloidal magnetic fields inside the core. As toroidal fields have no radial component and form around the rotational axis, they are parallel to the surface and thus enclosed by the core. When the toroidal field lines interact with the aforementioned spiral flow they in turn twist and reconnect, producing poloidal fields. The poloidal fields are able to escape the core and can be measured on the surface. As the Coriolis force is a result of Earth's rotation, the geometry of the poloidal magnetic fields aligns with the Earth's rotational axis.

The field generated by the geomagnetic dynamo extends out into a region in space, referred to as the magnetosphere. The magnetosphere shields the Earth from the bombardment of charged particles from the Sun and outer space, and is therefore continuously changing. Earth's magnetic field is complex; it consists of combinations of multiple multipole fields overlaid upon each other. Simplistically, it can be viewed as a dipole with a north and a south pole inclined at 11° with respect to the rotational axis of the planet ([McPherron,],[Lowrie, 2023])

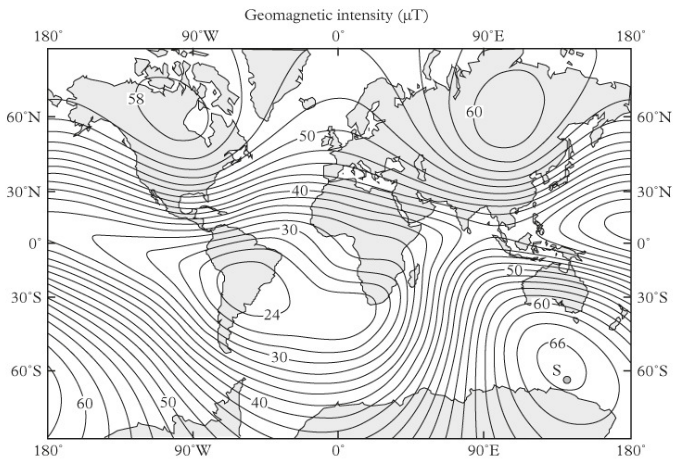

Figure 2.8.: Map of Earth's geomagnetic field intensity at the surface measured in μT. Taken from [Lowrie, 2023].

The external component of the geomagnetic field originates in the ionosphere, the ionized upper part of Earth's atmosphere, due to a process named ionospheric dynamo. Here, the motion of electrically charged particles during daytime generates electrical currents, which in turn produce secondary magnetic fields that are added to the main field generated by the geomagnetic dynamo to form the majority of the geomagnetic field. Other processes like the ring current, the magnetopausal current and the tail current contribute to the generation of the Earth's magnetosphere. The intensity of Earth's magnetic field varies over the surface of the globe and ranges from more than $60\mu T$ near the poles to less than $24\mu T$ close to the equator. In the case of the dipole field the region of the lowest intensity can be expected to lie at the magnetic equator. As mentioned above, the Earth's magnetic field is not a pure dipole, the weakest part of its magnetic field covers a region in the South Atlantic Ocean including parts of eastern South America and South Africa (see Figure 2.8). This magnetic anomaly, aptly named South Atlantic Anomaly is further discussed in Chapter 2.3.2. According to [Merrill and McElhinny, 1983], the intensity of Earth's magnetic field decreases by 5% every 100 years. In the region of the SAA the decrease is ten times as fast. [McPherron,] [Lowrie, 2023]

2.3.1. Earth's Magnetosphere

The region of space surrounding Earth, where charged particles are affected by the Earth's magnetic field. It is formed by solar wind encountering Earth's magnetic field which causes the resulting electrically charged plasma to be trapped within the magnetic field lines. The magnetic field lines are deformed by the solar wind, compressed on one side and stretched on the other as seen in Figure 2.9. The boundary between the solar wind and the Earth's magnetic field is known as the magnetopause ([Lowrie, 2023]).

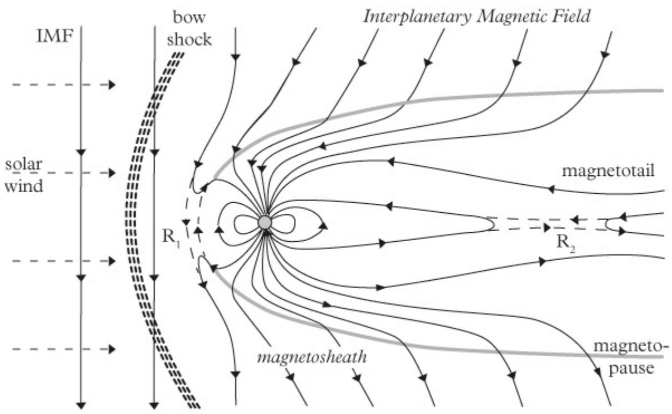

Figure 2.9.: Schematic of Earth's magetosphere to illustrate the effects of solar wind. Here the supersonic plasma from the solar wind compresses the atmosphere into a bow shock. The Earth's magnetic field subsequently redirects the solar wind to flow around the planet. Taken from [Lowrie, 2023].

Charged particles, mainly protons and electrons, from the solar wind can pass through the magnetopause and become trapped in the magentosphere by the magnetic field lines. The zone where this is happening is known as a "Van Allen radiation belt". Earth has two Van Allen radiation belts at different heights. The inner Van Allen radiation belt is located at 1000 - 10 000 km above the Earth's surface, the outer 13 00 - 60 000 km above the Earth's surface (see Figure 2.10) ([Lowrie, 2023]).

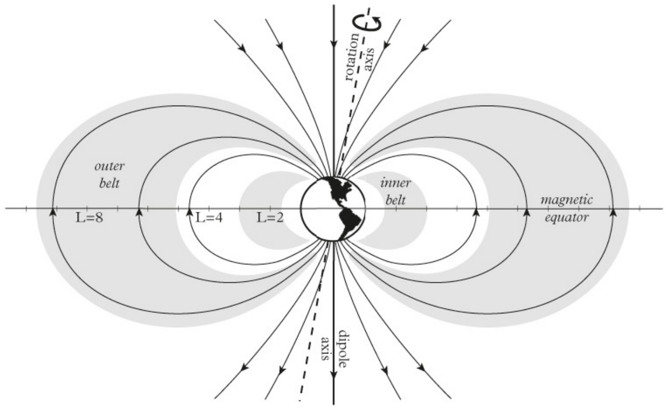

Figure 2.10.: Schematic of Earth's Van Allen Radiation Belts. Here the positions of the two radiation belts are given in terms of L-shells. The L-shells describe sets of magnetic field lines occupying the same regions in the space around Earth. Taken from [Lowrie, 2023].

2.3.2. South Atlantic Anomaly

The South Atlantic Anomaly (SAA) as depicted in Figure 2.11 is a region of the Earth's magnetic field located between $-50°$ and $0°$ latitude and $-90°$ and $+40°$ longitude ([Nasuddin et al., 2019]). Within the region, Earth's inner Van Allen radiation belt comes closest to the surface at the lowest altitude of 200 km, resulting in a lower geomagnetic field intensity compared to similar latitudes. This is a result of the previously discussed geomagnetic dynamo (see Chapter 2.3) as within the region of the SAA the flow patterns of the liquid outer core produce a reversely polarized magnetic flux at the core's surface leading to a local intensity minimum and an increase in magnetic flux. The flow patterns are not consistent and are subject to change over periods of time. These changes occur relatively quickly, resulting in a movement of the anomaly of 0.06° N and 0.28° W per year according to [Anderson et al., 2018] as well as an increase in area ([Lowrie, 2023]). The location of the peak flux is close to the field intensity minimum and currently situated over Brazil. [Trivedi et al., 2005] suggest that in 2002 the measured minimum of $22,850$vnT was located at 26° South and 54° West, shifting westward by 0.204° per year as seen in Figure 2.12 ([Anderson et al., 2018]).

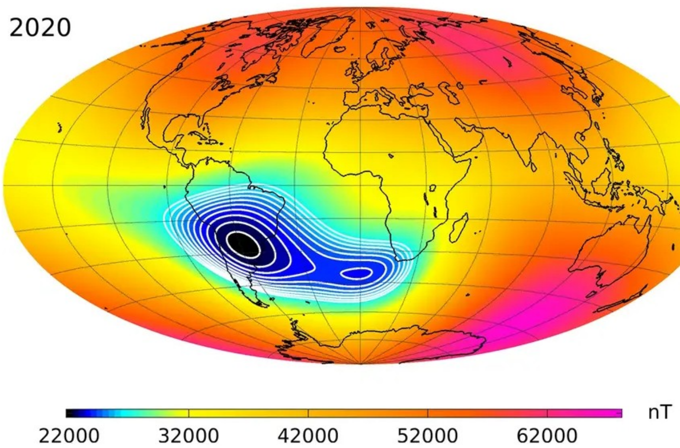

Figure 2.11.: The shape SAA (blue contours) in the year 2020. Image taken from [Finlay et al., 2020].

Spacecrafts in a Low Earth Orbit (LEO) are subjected to these higher radiation levels when passing through the SAA which can reach up to 413 μSv/day according to [Badhwar et al., 1999] risking damage to the onboard electronic systems. Damage to hardware can result from Single-Event Upsets (SEUs), which are changes in the state of a micro-electronic device, caused by the interaction of the device with a charged particle, e.g. a cosmic ray ([Binder et al., 1975]). To prevent damage to hardware, most non-essential satellite components are powered down during the passing of the anomaly. Data acquired inside the SAA was not linked down and discarded by CHEOPS until March 2025. In CHEOPS's seeing cosmic ray hits on the CCD is an unwanted byproduct of data acquisition ([Benz et al., 2020]).

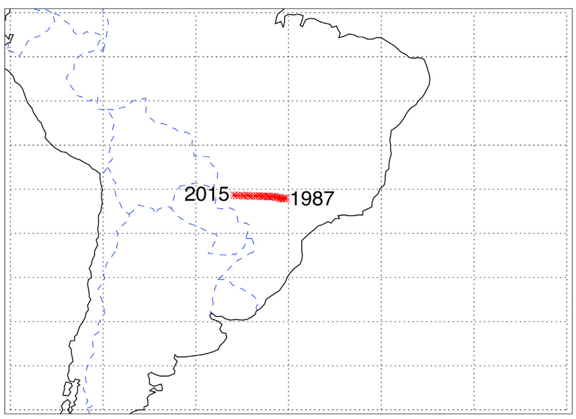

Figure 2.12.: Movement of the minimum of the SAA's field intensity.. Image taken from [Anderson et al., 2018].

2.3.3. Auroral Zones

The regions around the Earth's poles where auroras are most commonly observed are known as auroral zones. These regions are located between the latitudes of 65° and 75° north and south. The locations where auroras are observed at a given time are referred to as the auroral oval due to its distinct oval shape ([Feldstein, 1964], [Akasofu, 2015]). Figure 2.13 depicts the shapes of the auroral zone in pink and the auroral oval in green.

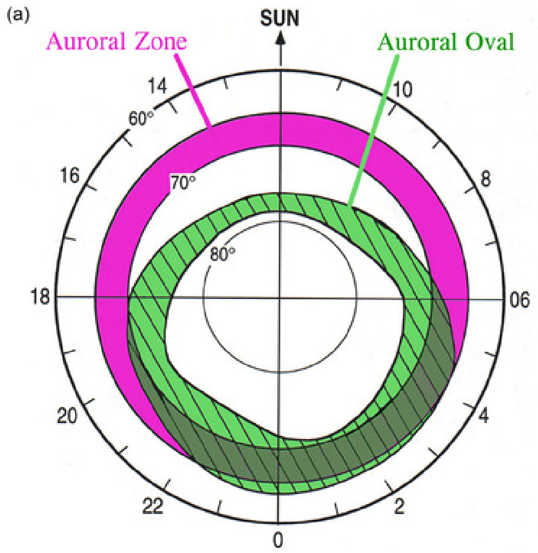

Figure 2.13.: Comparison of the auroral zone and the auroral oval in degrees of latitude. Taken from [Akasofu, 2015].

2.3.4. The K-index

The K-index is a global measurement to characterise variations in geomagnetic activity. It was first described by Julius Bartels in 1939 ([Bartels et al., 1939]) and is measured over a timespan of three hours. The index scale reaches from 0 to 9 based on the intensity of the geomagnetic activity, where any index above 5 indicates a geomagnetic storm. It also determines where auroras are most likely to be observed. There are several derived indices from the K-index. Most notably the Kp-index (short for planetary K-index), and ap-index (short for planetary a-index). According to [Bartels et al., 1939], the Kp-index is determined by calculating the weighted average of the K-indices from 13 observatories located at mid-latitudes. The ap-index is calculated by taking the three-hour amplitude of the K-index at one geomagnetic observatory ([Clúa de Gonzalez et al., 1993]).

3. Methodology

As described in Chapter 2.1 the CHEOPS satellite is designed to observe transit lightcurves of exoplanets around bright stars (Gmag <12). While the satellite passed the SAA no science data was down linked until March 2025, as images taken during SAA crossings are polluted due to cosmic rays. Data was only downlinked by the satellite, up until it reached the edges of the anomaly and not within. Since early March 2025 data collected during SAA crossings is also down linked, as it could hold scientific value. This provides the opportunity to investigate data from passes through the SAA. Before, data from inside the SAA existed only (i) sparsely when performing instrument monitoring, (ii) once due to the use of a incorrect, out of phase, orbit file, and (iii) in summer 2024, to actually map the SAA in order to refine the exclusion SAA mask.

The boundaries of the anomaly appear to be changing. CHEOPS's virtually consistent data acquisition makes it possible to study the potential changes over the course of the satellites' lifespan. The observations on the edges and within the SAA present an opportunity to characterise the anomaly by computing the cosmic ray density and using this as a metric. Within the usual data processing pipeline, cosmic rays are corrected for, so the final data product does not contain cosmic rays or any other bad/hot pixels. Therefore, identifying and counting the cosmic rays requires a different data processing pipeline, applied directly to the raw, uncorrected data.

This chapter introduces the workflow of the newly, for this specific research case, developed processing pipeline starting from the raw images and ending in a comprehensive world map at CHEOPS orbit height of $\sim$ 700 km of a binned average per area of the number of cosmic rays, the cosmic ray density, as well as the percentage of pixels affected by cosmic rays. Using these, the contour of the SAA as well as other magnetic field anomalies can be traced over the course of 4.5 years of data collection since the satellite began its science operation at the end of March 2020.

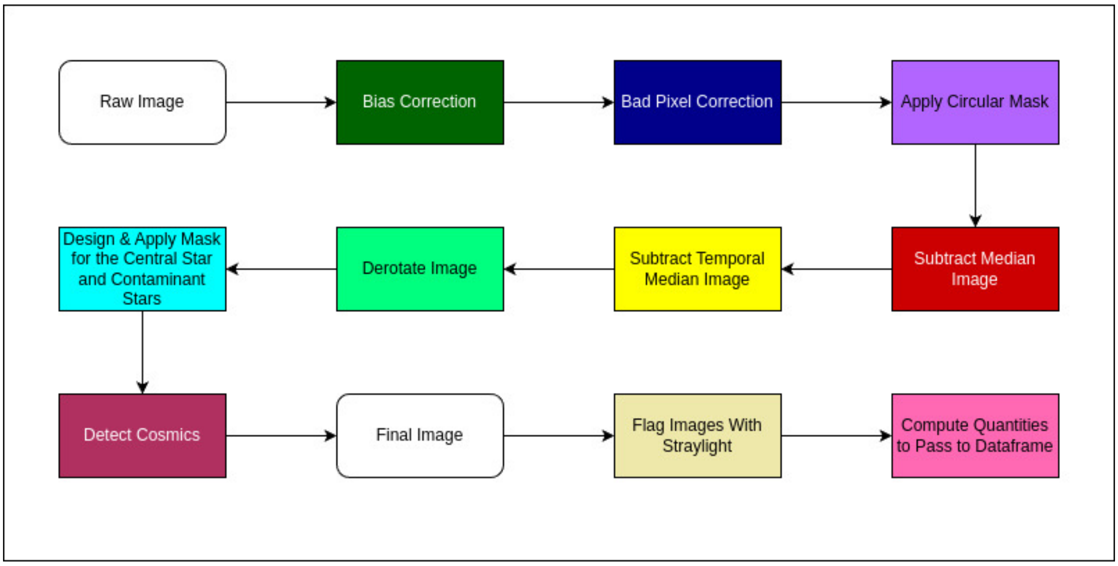

Figure 3.1.: Flowchart of the data processing pipeline. The individual processing steps are colour coded and explained in detail in the corresponding sections.

Figure 3.1 depicts a schematic representation of the newly developed processing pipeline, starting from the raw image SubArrays (see Sections 2.1.3.1 and 2.1.4.2) and ending in a final, corrected image. This image can be used to compute properties and quantities, such as the number of cosmic rays. The pipeline was developed around the idea, that cosmic rays appear in the image as small clusters of bright pixels. When all other bright clusters of pixels of known origin (e.g. the central star or contaminant stars) are masked, the remaining clusters should be cosmic rays. This section details the data processing pipeline as seen in the aforementioned figure. The first part of the new processing pipeline consists of five preprocessing steps, beginning with obtaining the square 200 × 200 pixel raw images from CHEOPS (see Figure 3.2). The preprocessing starts with the bias correction ( ) where the image gets corrected for the base read-out noise level (see Section 3.1.1.1). Subsequently, the image is corrected for different types of bad pixels ( ) not only to improve image , but also to prevent misidentification of cosmic rays further down the line (see Section 3.1.1.2). Step three of the preprocessing is the application of the circular mask ( ), which transforms the initial square image into a circular image (see Section 3.1.1.3)). The last two steps of the preprocessing are the subtraction of the median image (, see Section 3.1.1.4) and the subtraction of the temporal median (, see Section 3.1.1.4) which constitute the background correction. The last preprocessing step is necessary to correct for changes in the background noise over the course of one science visit. When these preprocessing steps are done, the images are derotated ( ), to be able to mask any contaminant stars in the subsequent processing (see Section 3.1.2). The next step designs and applies the mask for the central star and any contaminant stars (, see Section 3.1.3).Once all stars are masked, the final step of the pipeline commences: the detection of cosmic rays (see), resulting in the final image (see Section 3.1.4).

Once all images of a science visit have been processed, the pipeline features two more steps before data analysis is possible. Firstly, images contaminated by straylight have to be flagged ( ), in order to treat them separately later on (see Section 3.1.5). The final step of the pipeline now handles the computation of interesting properties and quantities such as the percentage of pixels affected by cosmic rays (see) as described in Sections 3.2.1, 3.2.2, 3.2.3 and 3.2.4. The data are subsequently converted into a `pandas` dataframe to be analysed afterwards (see Sections from 3.2.5).

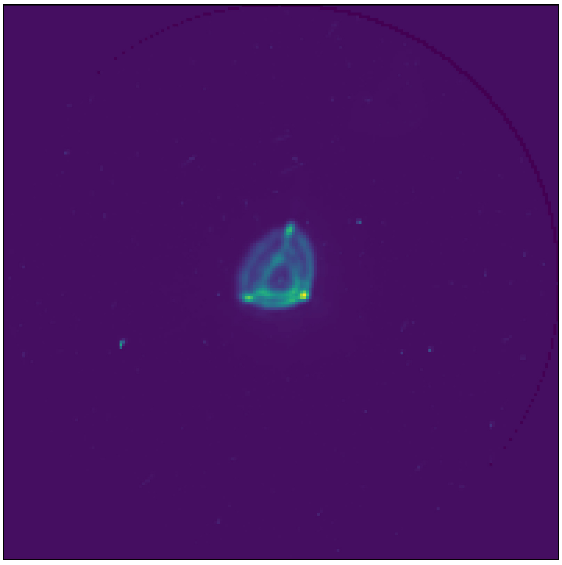

Figure 3.2.: Original SubArray of the target AU Mic, with an exposure time of 5 s and a total exposure time of 35 s.

3.1. Data Processing

3.1.1. Preprocessing

In contrast to the usual data processing process, which would usually undergo several stages of processing and corrections to ensure high-quality light curve data, this case of science requires starting from the raw data product. The data used come in the form of 200 x 200 pixel data cubes of SubArrays, each cube being a part of the full 1024 x 1024 pixel CCD frame, with the target star in the centre (see Figure 2.4). Here, the number of SubArrays in the cube depends on the length of the observation run and the exposure time of each frame. Before an algorithm for the detection of cosmic rays can be applied, a number of preprocessing steps have to be performed to prepare the data. As part of the preparation corrections have to be performed to correct for the bias, bad pixels and background noise.

3.1.1.1. Bias Correction

The first property the image is to be corrected for is the bias. It is corrected by taking the left overscan pixels outside the CCD into account. A mean over the left overscan and the blank left pixels is calculated to give the bias value of each SubArray as seen in Listing 3.1. As stated in [Hoyer, S. et al., 2020] for CHEOPS this value should fall around ~ 609 Analog-to-Digital Units (ADUs) per readout. ADU is defined as "the output voltage from a given pixel [...] converted to a digital number" according to [Howell, 2006]. The author states that in order to produce 1 ADU the amount of required voltage is defined by the gain of the CCD (see Chapter 2.1.3.3) , which is determined by the output electronics. Usually, the value of the gain is given in the amount of electrons needed to produce one ADU step. In the case of the CHEOPS CCD the gain value is equal to 0.5111. The obtained bias value is subsequently subtracted from the SubArrays' pixel values before the remaining corrections are applied.

```python
def bias_correction(overscan_left, blank_left, image):
subarray = image.copy().astype('float64')

mean_overscan = []
mean_blank = []
mean_general = []
corrected_array = []

for i in range(len(overscan_left)):
    mean_overscan.append(np.nanmean(overscan_left[i]))
    mean_blank.append(np.nanmean(blank_left[i]))

if len(mean_overscan) == len(mean_blank):
    for i in range(len(mean_overscan)):

        mean = (mean_overscan[i] + mean_blank[i])/2
        mean_general.append(mean)

for i in range(len(subarray)):
    corrected_array.append(subarray[i] - mean_general[i])

corrected_array = np.array(corrected_array)
return corrected_array
```

Listing 3.1: The bias correction function.[2]

3.1.1.2. Bad Pixel Correction

A bad pixel map from specific dark observations, henceforth referred to as weekly dark images, is created on a weekly basis by the CHEOPS Instrument team identifying five different types of bad pixels: totally dead pixels, partially dead pixels, hot pixels, saturated pixels and Random Telegraphic Signal (RTS) pixels ([Bekkelien, 2023]). Dead pixels refer to any CCD pixel, being unresponsive to light and therefore measuring no signal despite being subjected to a light source. According to [Fortier, A. et al., 2024] dead pixels are classified as either completely unresponsive to light, and therefore being described as totally dead, or having a lower sensitivity to light and subsequently producing a lower signal output compared to the neighbouring pixels, being described as partially dead. Hot pixels are defined as pixels with an elevated dark current, contributing noise to CHEOPS' photometric data.

If a hot pixel is detected to have varying dark current levels over time, it is known as a RTS pixel which is able to retain charges and release them over time, leading to the presence of so-called charge traps within the pixel. Lastly, a saturated pixel is defined as a pixel permanently saturated to its maximum capacity and therefore not able to capture any more photons. All the previously mentioned types of bad pixels are regularly mapped and monitored ([Fortier, A. et al., 2024]).

To identify bad pixels, different procedures are in place for the different types of bad pixel. [Fortier, A. et al., 2024] illustrate the process as follows: dead pixels, hot pixels and saturated pixels can be identified using the aforementioned weekly dark images. As CHEOPS is not equipped with a shutter, true dark images cannot be obtained, but will always feature a zodiacal light component. In the absence of a shutter, the dark images are captured using reasonably empty regions of the sky instead. Here, two sets of ten full frame images with exposure times of 60 s and 0.001 s respectively are acquired, the pointing being shifted between the images to prevent possible sources of contamination, i.e. field stars, to appear in the same CCD spot.

The resulting dark image is then suitable to be used for measuring the aforementioned types of bad pixels. In order to measure RTS pixels, a longer timeframe is necessary. Therefore, observations to detect RTS pixels are only performed four times per year. During these observations, a suitable dark region is observed continuously for ten CHEOPS orbits, equating to an approximate time of 8 h. With an exposure time of 60 s per frame, approximately 1000 images are captured, out of which 50 to 80 % are used for the detection of RTS pixels.

According to [Fortier, A. et al., 2024] at the time of publication there have been no identifications of totally dead, partially dead or saturated pixels. To qualify as a hot pixel, the authors define the flux of pixel to exceed 3 e^{-} s^{-1} when a flux close to 0 is expected. According to this definition, [Fortier, A. et al., 2024] count 110 000 hot pixels in the full frame image and 3 800 hot pixels in the SubArray.

They also classify any hot pixel as a RTS pixel if its dark current varies within 8 h. Hereby jumps in the lightcurve of the hot pixels are searched for where even a single jump is sufficient to classify the corresponding hot pixel as a RTS pixel. In order to correct for the various types of bad pixels in addition to the bad pixel map, the dark frame image is also necessary to be used. Within the bad pixel map each pixel is assigned a value between -2 and 2 according to its type. The value of 0 is reserved for "good pixels" ([Bekkelien, 2023]), with the intention of ignoring these types of pixels in the bad pixel correction. The remaining pixel types can be categorised into dead pixels, including the subtypes totally dead pixels and partially dead pixels, hot pixels, saturated pixels and RTS pixels. These pixel types are assigned the values of -2 & -1, 1, 2 and 3 respectively.

```
def bad_pixel_correction(new_bad_pixel_map, new_dark_frame, image):
    bad_pixel_map = new_bad_pixel_map.copy().astype('float64')
    dark_frame = new_dark_frame.copy().astype('float64')
    subarray = image.copy().astype('float64')

    coordinates_non_zero_elements = []
    for i in range(len(bad_pixel_map)):
        for j in range(len(bad_pixel_map[i])):
            if bad_pixel_map[i][j] != 0:
                coordinates_non_zero_elements.append((i,j))

    readout_noise = 3.5
    corrected_image = [layer[:] for layer in subarray]

    for (x,y) in coordinates_non_zero_elements:
        for z in range(len(subarray)):
            value = subarray[z][x][y]
            if value > 0:
                corrected_image[z][x][y] = corrected_image[z][x][y] -
   dark_frame[x][y]
            elif value < 0:
                corrected_image[z][x][y] = corrected_image[z][x][y] -
   readout_noise

    corrected_image = np.array(corrected_image)
    return corrected_image
```

Listing 3.2: The bad pixel correction function.[2]

A function (see Listing 3.2) ensures that every SubArray is corrected for all possible types of bad pixels. Within the bad pixel function, pixels are corrected based on their assigned numeric bad pixel value using either the corresponding dark frame value, or the read-out noise, taken from [Hoyer, S. et al., 2020] and set to 3.5 ADU per pixel. As shown below, if the numeric bad pixel value is >0 the corresponding dark frame value is used. Since hot, saturated and RTS pixels characteristically possess high dark currents, removing the excess dark current gives the legitimate flux of the pixel. This hold true for all bad pixels except the RTS pixels, which can have different values than stated in the bad pixel map.

If the numeric bad pixel value is smaller than 0, the readout noise is used to correct for the respective bad pixel types, as dead pixels can subsequently be treated as noise and won't produce negative outliers. The actual correction is performed by first identifying the type of bad pixel and subsequently subtracting the corresponding correction value. As stated in [Fortier, A. et al., 2024] no saturated pixels as well as dead pixels are expected, therefore corrections should only apply to hot pixels and RTS pixels.

3.1.1.3. Application of the Circular Mask

Before any further processing is performed, the square 200 × 200 pixel SubArray is transformed into a circular image with a radius of 100 pixel using a circular mask. Listing 3.3 depicts the function that transforms the square images. Starting with calculating the centre of the SubArray, the function then calculates the distance of each point to the centre and subsequently creates a circular mask with a radius of 100 pixel.

```
def create_circular_mask(size, radius):

# Build circular mask
center_x, center_y = size // 2, size // 2
# Create a grid of (x,y) coordinates
y, x = np.ogrid[:size, :size]
# Calculate the distance of each point from the center
distance_from_center = np.sqrt((x - center_x)**2 + (y - center_y)**2)
# Create a mask for points within the radius
mask_circular = distance_from_center > radius
print(mask_circular)
# Apply the mask to the array

return mask_circular
```

Listing 3.3: The function to transform the 200 × 200 pixel SubArray images into circular images with a radius of 100 pixel.[1]

3.1.1.4. Background Correction

Before the images can be derotated, the background has to be corrected for. Since a singular CHEOPS science visit on average takes 8 h ([Benz et al., 2020]), there will be changes in the background noise level throughout the images of a visit. The data structure of all the circular images of a particular science visit will henceforth be referred to as a data cube. To obtain a coherent background noise level throughout the data cube, the median of each image inside the cube is computed and subsequently subtracted from the image as depicted in Figure 3.3 and Listing 3.4. This operation will reduce the background noise of each image. To reduce the background noise of each pixel throughout the data cube, a temporal median is calculated.

```python
def subtract_median_image(images, circular_mask):

    median_images = images.copy().astype('float64')

    for i in range(len(images)):
        mask_zeros = median_images[i] != 0
        median_image = np.nanmedian(median_images[i][mask_zeros])
        median_images[i][mask_zeros] = median_images[i][mask_zeros] - median_image

    median_images = np.abs(median_images)
    return median_images
```

Listing 3.4: Background correction: subtraction of the median image.[2]

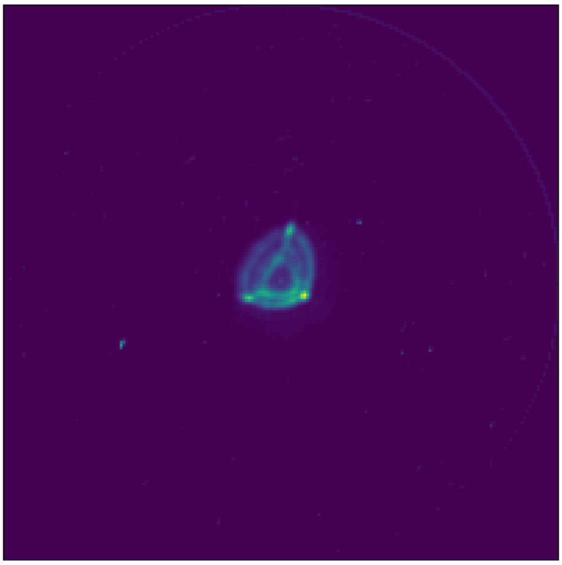

Figure 3.3.: SubArray of AU Mic with the median value removed.

As a first step, the median value per pixel is computed along the temporal axis of the data structure, resulting in one additional image where every pixel value is the median value of all the corresponding pixels in the data cube as depicted in Figure 3.4 and Listing 3.5. In the second step, this image is subsequently subtracted from all the images in the data cube.

```python
def subtract_temporal_median_image(images):
    '''
    Compute the median for all pixels through the cube to get the median image and remove it from each image in the data cube
    '''
    median_subtracted_images = images.copy().astype('float64')

    median_image_per_pixel = np.nanmedian(median_subtracted_images, axis=(0))

    #subtract median image from each image in the data cube
    for i in range(len(median_subtracted_images)):
        median_subtracted_images[i] = median_subtracted_images[i] - median_image_per_pixel

    median_subtracted_images = np.abs(median_subtracted_images)

    return median_subtracted_images
```

Listing 3.5: Background correction: subtraction of the median of every pixel in the data cube.[2]

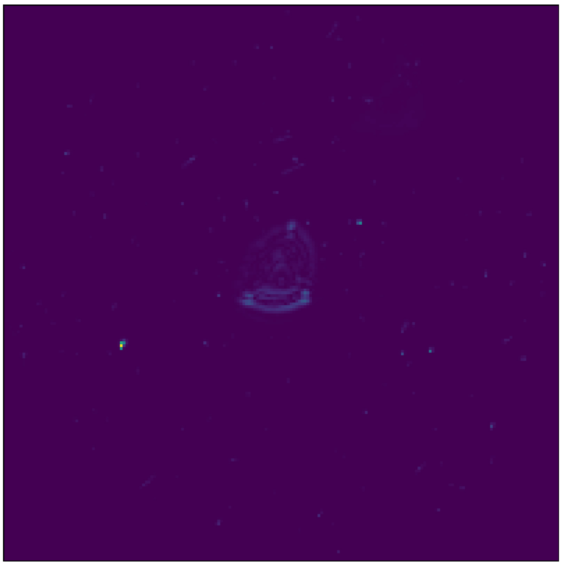

Figure 3.4.: SubArray of AU Mic with the median pixel value removed.

3.1.2. Derotation

Once these corrections have been performed, every image of the data cube is derotated. The method described below is used for visits outside the SAA. Derotation of the images is necessary as CHEOPS is nadir locked (see Chapter 2.1.1), meaning the satellite rotates around its pointing axis in order to provide a thermally stable environment ([Fortier, A. et al., 2024]).

Although the central star remains stable, due to nadir locking the background will rotate corresponding to the satellite's roll angle. As potential cosmic ray hits are instantaneous, the process of derotation will not affect them. To successfully mask contaminant stars, every SubArray image is derotated according to the corresponding roll angle. First, the roll angle for each SubArray image is read from the lightcurve file before setting the first of those angles as the reference. Using the python library OpenCV a 2×3 transformation matrix is computed, which is then used to rotate the image (see Listing 3.6). To actually rotate the image a method called affine transformation is used, which mathematically corresponds to a linear transformation followed by a vector addition and is represented by the following matrix

$$\mathbf{dst}(x, y) = \mathbf{src}(M_{11}x + M_{12}y + M_{13}, M_{21}x + M_{22}y + M_{23})$$

where **dst** is the ouput image, **src** is the input image and M is the 2×3 transformation matrix ([Bradski, 2000]). Figure 3.5 depicts an image after the derotation process.

```python
 def derotate_images(attitude_file, images, nb_images, height_images, width_images):

 images = images.astype(np.float64)
 roll_angle = read_lc(attitude_file)

 derotated_openCV_images = np.zeros((nb_images, width_images, height_images), dtype=np.float64)
 first_image_angle = roll_angle[0]

 # Derotate each image
 for i,image in enumerate(images):
     rotate_by = -(roll_angle[i] - first_image_angle)
     rotation_matrix = cv2.getRotationMatrix2D((width_images / 2, height_images / 2), rotate_by, 1)
     #rotated_image = cv2.warpAffine(image, rotation_matrix, (width_images, height_images))
     rotated_image = cv2.warpAffine(image, rotation_matrix, (width_images, height_images), flags=cv2.INTER_NEAREST)
     derotated_openCV_images[i] = rotated_image

 return derotated_openCV_images
```

Listing 3.6: The derotation function.[3]

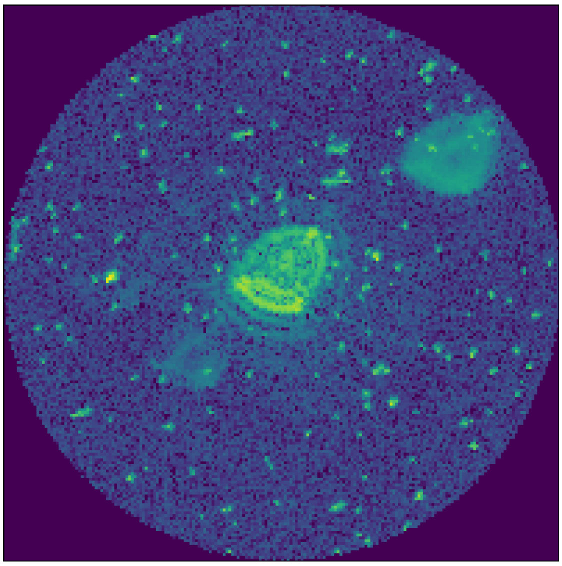

Figure 3.5.: Derotated SubArray of AU Mic.

3.1.3. Masking of the Central Star and Contaminants

After derotation, the central star and contaminant stars are masked. The general idea is to mask all pixels in the images that belong to the central star or are part of any contaminant background star. The remaining pixels with a value greater than the average background therefore should be cosmic rays.

Listing 3.7 illustrates the procedure of masking the central star as well as possible contaminant backgroud stars. The image used in the process of masking is the derotated image with a corrected background (see Figure 3.5). The first operation to be performed is to mask the central star with a circular mask. This is done using the same function (Listing 3.3) as in the beginning of the data processing (see Chapter 3.1). The radius of the mask for the central star is set to 25 pixels. The reason being that, as seen in Figure 2.3, 90% of the energy of CHEOPS' PSF is concentrated within a radius of 16.5 pixels.

To ensure the entire extent of the star is covered by the mask, a radius of 25 pixels is chosen. If necessary, the mask can be enlarged using the `dilate` function from the `OpenCV` library to fully encompass the central star. The second step is to mask possible contaminant stars using previously calculated thresholds for visits inside and outside the SAA.

```python
def create_contaminant_mask(derotated_openCV_images, edges_mask,
    saa_or_science, enlarge_mask = True, inspect_threshold = False,
    threshold = 0):

    image_for_mask = np.nanmedian(derotated_openCV_images, axis=(0)) #
    median

    [...]

    if saa_or_science == 'SAA':
        mask = image_for_mask > threshold
    else:
        mask_central_star = create_circular_mask(np.shape(
    derotated_openCV_images)[1], 25)
        mask = (image_for_mask > threshold) | ~mask_central_star


    med_or_mean = 'median'

    mask = mask.astype(np.float64)

    final_mask = mask

    if enlarge_mask:
        # Define the kernel for dilation
        kernel = np.ones((3,3), dtype=np.float64)
        extension_mask = 2
        enlarged_mask = cv2.dilate(mask, kernel, iterations=
    extension_mask) == 1
        final_mask = enlarged_mask

    [...]

    return final_mask, threshold
```

Listing 3.7: The function to create the masks for the central star and the contaminant stars.[3]

$$\text{threshold}_{\text{n}} = \text{threshold}_{\text{n-1}} \cdot \sqrt{\text{n}_{\text{exp}}} \tag{3.1}$$

Starting from the base noise level in both cases, 6.5 and 10 for visits inside and outside the SAA respectively, the threshold is subsequently corrected as illustrated in equation 3.1, where n_{exp} is the number of stacked images. The equation, uses the stacking order (see Section 2.1.4.2) to determine the masking threshold. The stacking order scales with the number of images, by co-adding pixel by pixel, resulting in the detected signal increasing linearly and the noise increasing in quadrature. Taking the squareroot of the stacking order adjusts the detection threshold to match the original noise level in the stacked image. This ensures the masking criteria to be kept statistically consistent.

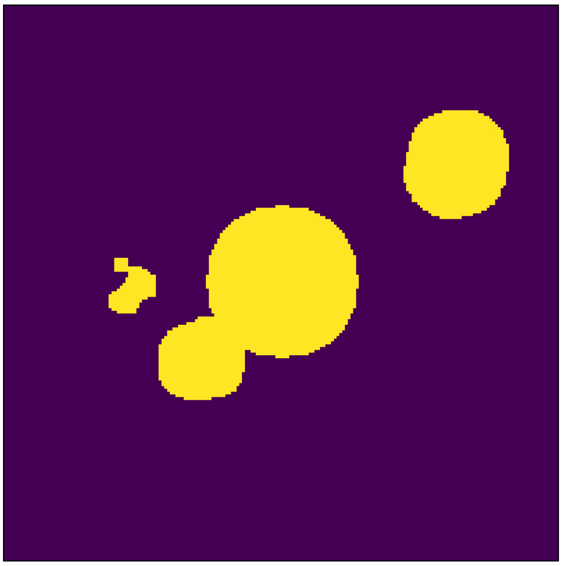

Figure 3.6.: Designed mask for AU Mic.

Pixels with values above these thresholds that are not already masked as part of the central star are defined as contaminants and masked. Figure 3.6 depicts mask designed for the central and contaminant stars, which is then used to mask the image. The resulting masked image is shown in figure 3.7.

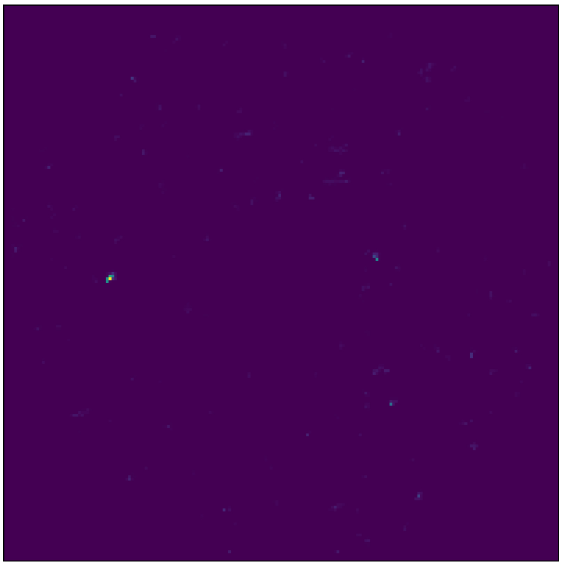

Figure 3.7.: Masked SubArray of AU Mic.

3.1.4. Detection of Cosmic Rays

With the preprocessed SubArrays, cosmic rays can now be detected as illustrated in Listing 3.8. To detect cosmic rays, the previously masked SubArrays are converted into binary images using the `threshold` function of the aforementioned `OpenCV` library ([Bradski, 2000]). The `threshold` function returns a binary image using a predefined threshold for cosmic rays of 250 on gray scale from 0 (black) to 255 (white). The grey scale values of the individual pixels in the original image are converted from a 16-bit range into an 8-bit range using the scaling factor $\frac{255}{65535}$. The values 255 and 65535 represent the maximum possible values for the 8-bit greyscale and the 16-bit ADU values respectively.

```
def detect_cosmics(masked_images, threshold):

    # convert masked images to binary
    binary_images = masked_images.copy()
    for i,image in enumerate(binary_images):
        _, img = cv2.threshold(image, threshold, 255, cv2.THRESH_BINARY)
        binary_images[i] = img

    # Initialize the counter of cosmics per image
    loc_cosmics  = []
    stats_cosmics = []
    centroids_cosmics = []

    [...]

    for i,image in enumerate(binary_images):
        _, labels, stats, centroids = cv2.connectedComponentsWithStats(
       image.astype(np.uint8))
        loc_cosmics.append(labels)
        stats_cosmics.append(stats)
        centroids_cosmics.append(centroids)


    return binary_images, loc_cosmics, stats_cosmics, centroids_cosmics
```

Listing 3.8: The function to detect cosmic rays from the masked images.[1]

At this stage, the threshold was defined by trial and error. Chosing a lower threshold would result in a higher number of false positive detections, whereas a higher threshold would lead to cosmic rays with lower ADU values not being detected. This threshold is again corrected using the stacking order as seen in equation 3.2, where $\mathrm{n_{exp}}$ is the number of stacked images. This equation uses a threshold defined in terms of ADU.

$$\text{threshold} = \text{threshold} \cdot \left(\frac{255}{65535 \cdot \mathrm{n_{exp}}} \right) \tag{3.2}$$

The resulting binary image, every pixel below the cosmic ray threshold is considered part of the background and only the pixels with values above are considered as cosmic rays. Using the `OpenCV` ([Bradski, 2000]) function `connectedComponentsWithStats` the cosmic rays are identified from the binary image.

The function scans binary images and groups pixels into components based on the number of adjacent pixels with the same binary value. `connectedComponentsWithStats` then returns information about the number of identified cosmic rays, their location and their centroid. Although all of the different properties are calculated, only the number and location of cosmic rays are used for further analysis. Other useful quantities for analysis such as the number of electrons and flux of the cosmic rays, the density of cosmic rays or the number of pixels of the largest cosmic are calculated later on (see Section 3.2). The final image with all identified cosmic rays is shown in Figure 3.8.

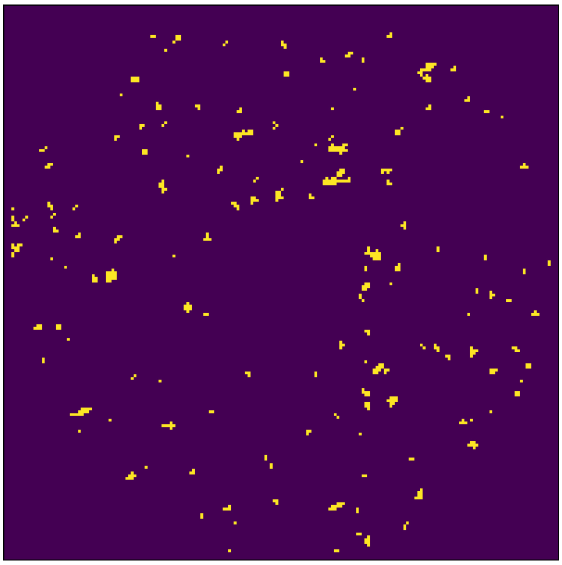

Figure 3.8.: Detected cosmics in the SubArray of AU Mic.

3.1.5. Stray Light

```python
def remove_straylight_new(masked_images,edges_circular_mask,
    contaminant_mask,loc_cosmics):

    # Now not taking into account the masked (circular subArray, masked
    stars + CR) pixels
    masked_array = masked_images.copy()


    mean_per_image_stars_mask = []
    mean_per_image_full_cosmics_mask = []
    for i,image in enumerate(masked_array):
        ## Full mask (circular subArray + stars + cosmics)
        cosmics_mask = loc_cosmics[i] > 0
        mask_stars = edges_circular_mask | contaminant_mask.astype(bool)
        image[mask_stars] = np.nan # convert to nans the pixels outside
    the circular crop of the subArray and the masked stars
        mean_per_image_stars_mask.append(np.nanmean(image)) # mean with
    the stars masked
```

```
        # Now set to nan the cosmic affected pixels as well
        image[cosmics_mask] = np.nan # convert to nans the pixels affected by cosmics
        mean_per_image_full_cosmics_mask.append(np.nanmean(image)) # mean with the stars masked

    # compute percent increase of mean with the star mask vs the full mask
    percent_increase_star_masked_vs_cosmic_masked = ((np.array(mean_per_image_stars_mask)/np.array(mean_per_image_full_cosmics_mask))-1)*100

    #calculate mean of new array
    mean_visit_stars_mask = np.nanmedian(mean_per_image_stars_mask)
    mean_visit_full_cosmics_mask = np.nanmean(mean_per_image_full_cosmics_mask)

    thresh_mean_cosmic_mask = np.mean(mean_visit_full_cosmics_mask)+5
    thresh_diff = 200

    # Create binary array to flag straylight images -> straylight images are flagged as 1
    # Flag points as stray light if they show a large mean and a small diff between the star masked images and the full masked (inc. cosmics) images
    straylight_binary_array = (mean_per_image_full_cosmics_mask > thresh_mean_cosmic_mask) & (percent_increase_star_masked_vs_cosmic_masked < thresh_diff)

    # background_threshold = mean_new + 10 #arbitrary number for now -> see what will filter stray light the best
    # straylight_binary_array = (median_per_image > background_threshold)

    return straylight_binary_array
```

Listing 3.9: The function to flag images contaminated by stray light.[3]

Before the data is analysed, images contaminated with stray light have to be flagged in order to handle the concerning images separately (see Listing 3.9 for the illustration of the process). In this context stray light occurs when the telescope's LOS is close to the Earth's atmosphere and sunlight is simultaneously reflected off the atmosphere. When an image is contaminated with stray light, the mean ADU value of the background of the image in question is significantly higher compared to the previous image.

The analysis for stray light contamination is performed on the resulting images from the last preprocessing step with a masked central star, masked background stars, and identified cosmic rays. The first step is to also mask the identified cosmic rays using the location property computed previously (see Section 3.1.4). Once these cosmic rays have been masked, two different means are computed: one for the image with only the stars masked (referred to as stellar mask) and one with stars and cosmic rays masked (referred to as full mask).

Afterwards the increase (in percent) of the first mean compared to the second mean is computed. Once this has been done, the mean of the entire data cube with masked stars and cosmic rays is computed, from which subsequently the mean threshold of the mask with cosmic rays is calculated. Before the final step of the flagging process, a threshold, is set to constrain the maximum difference between the images with stars masked and the images with stars and cosmic rays masked. This threshold is set to a value of 200, which was determined by trial and error. Setting the threshold to a higher value can result in images with a high number of cosmic rays being flagged as stray light whereas using a smaller threshold can lead to stray light images not being flagged as such. Lastly as mentioned the final binary array is computed in which it is determined whether or not an image is contaminated by stray light.

In the last step images are flagged as cosmic rays if they fulfill the following criteria: (i) the mean of the image is large compared to the threshold of the full mask and (ii) the difference between the image with a stellar mask and the image with a full mask is small. The resulting binary array indicates whether the corresponding images are contaminated by stray (array entry value 1) not contaminated images have the array entry value 0.

3.2. Analysis

Once all cosmic rays have been identified and counted, different properties can be calculated and inferred, such as the surface density of detected cosmic rays, the flux of the cosmic rays as well as the percentage of pixels of an SubArray affected by cosmic rays (see in Figure 3.1). The calculation of these properties can be seen in Listing 3.10. Sections 3.2.1, 3.2.2 and 3.2.3 detail the process of calculation for each of those properties respectively. Additionally, the number of electrons and flux of the cosmic rays can be computed, as well as investigated how solar activity affects the number of cosmic rays.

```
def cosmics_metrics(visit_labeled_cosmics, visit_info_cosmics,
    nb_non_masked_pixels, pixel_size, total_exp_time):

    nb_cosmics_arr = np.array([])
    nb_pixels_largest_cosmics_arr = np.array([])
    percentage_cosmic_pixels_arr = np.array([])
    density_cosmics_arr = np.array([])

    for image_info_cosmic in visit_info_cosmics:


        cosmics_stats = image_info_cosmic[1:,-1]
        if (len(cosmics_stats) == 0) or (len(cosmics_stats[cosmics_stats
    != 1]) == 0):
            nb_cosmics_arr = np.append(nb_cosmics_arr,0)
            nb_pixels_largest_cosmics_arr = np.append(
    nb_pixels_largest_cosmics_arr,0)
```

```
            percentage_cosmic_pixels_arr = np.append(percentage_cosmic_pixels_arr,0)
            density_cosmics_arr = np.append(density_cosmics_arr,0)
            continue
        else:
            stats_no_1_pix = cosmics_stats[cosmics_stats != 1] # exclude single pixels
            # nb_cosmics
            nb_cosmics = len(stats_no_1_pix)
            nb_cosmics_arr = np.append(nb_cosmics_arr,nb_cosmics)
            # largest cosmic
            nb_pixels_largest_cosmics = np.max(stats_no_1_pix)
            nb_pixels_largest_cosmics_arr = np.append(nb_pixels_largest_cosmics_arr, nb_pixels_largest_cosmics)
            # percentage affected pixels
            nb_pix_affected_no_1_pix = np.sum(stats_no_1_pix)
            percentage_cosmic_pixels = (nb_pix_affected_no_1_pix/nb_non_masked_pixels)*100
            percentage_cosmic_pixels_arr = np.append(percentage_cosmic_pixels_arr, percentage_cosmic_pixels)
            # density cosmics
            cm2_analysed = nb_non_masked_pixels*((pixel_size*1e2)**2) # cm2
            density_cosmics = nb_cosmics/cm2_analysed/total_exp_time
            density_cosmics_arr = np.append(density_cosmics_arr, density_cosmics)

    # percentage affected pixels per sec
    percentage_cosmic_pixels_per_sec_arr = percentage_cosmic_pixels_arr/total_exp_time

    return nb_cosmics_arr, density_cosmics_arr, nb_pixels_largest_cosmics_arr, percentage_cosmic_pixels_arr, percentage_cosmic_pixels_per_sec_arr
```

Listing 3.10: The function to obtain different properties of cosmic rays.[1]

3.2.1. Number of Cosmic Rays

The first of the aforementioned properties being inferred is the number of cosmic rays in every SubArray. A detection is in this case defined as an area of continuous pixels above the predefined threshold (see Section 3.1.4: single pixels above the threshold are disregarded and flagged as a so-called non-detection. To obtain the number of cosmic rays and determine, whether or not a cosmic ray qualifies as a detection, the code shown in Listing 3.10 is used. Within the function, the number of cosmic rays is calculated using the number of foreground pixels returned from the `detect_cosmics` function (see Section 3.1.4 and Listing 3.8). However, the function returns a result in which every pixel detected is counted as cosmic ray, therefore the single hits have to be filtered out, as mentioned above. Additionally, the number of pixels of the largest cosmic is calculated by returning the maximum value of the previously computed array.

3.2.2. Cosmic Ray Density

Listing 3.10 illustrates the calculation of the density of cosmic rays in lines 30 - 33. To calculate the density of cosmic rays, the area of the image without masked pixels is calculated in square centimetres as seen in equation 3.3. The pixel size of the CCD is 13×10^{-6} m according to [Cessa et al., 2017].

$$\text{analysed cm}^2 = \text{number of unmasked pixels} \times (\text{pixel size} \times 100)^2 \tag{3.3}$$

Afterwards the number of detected cosmic rays is divided by the previously calculated area and by the total exposure time, giving the density of cosmic rays in terms of hits $\text{cm}^{-2}\ \text{s}^{-1}$.

3.2.3. Percentage of Pixels affected by Cosmic Rays

The last calculated property, the percentage of pixels affected by cosmic rays makes use of the previously calculated number of cosmic rays of the entire image. As depicted in Listing 3.10, lines 26 - 29, the number of pixels within the detected cosmic ray hits (cosmic rays consisting of more than one pixel) is computed. To subsequently calculate the percentage of pixels affected by cosmic rays the aforementioned value is divided by the number of unmasked pixels in the image and multiplied by 100. At the end this value is divided by the total exposure time of the image, to obtain the percentage of pixels affected by cosmic rays per second.

3.2.4. Flux of the Cosmic Rays

To get an estimation of the photoelectronic flux of the cosmic rays in the CCD image the number of collected electrons per pixel has to be calculated. Afterwards, this value is divided by the exposure time of the image. Listings 3.11 and 3.12 illustrate this process. Starting from obtaining the ADU for each pixel this value is then multiplied by the CCD gain in order to obtain the actual number of electrons collected (see Listing 3.11). This value is subsequently summed for every pixel in a detected cosmic ray. In order to obtain the actual photoelectronic flux, the resulting sum has to be divided by the exposure time of the image (see Listing 3.12). As with CHEOPS images the stacking order (see Chapter 2.1.4.2) of the images has to be taken into account to get the actual exposure time for each image. The value obtained at the end is the photoelectronic flux in terms of $e^{-}\ \text{s}^{-1}$ pixel^{-1}.

```
def calculate_electrons(adu, gain):
number_of_electrons = []
sum_electrons = []
for group in adu:
    group_electrons = []
    electrons = 0
    for i in group:
        electron_count = gain*i
        electrons += electron_count
```

```
            group_electrons.append(electron_count)
        number_of_electrons.append(group_electrons)
        sum_electrons.append(electrons)

    return number_of_electrons, sum_electrons
```

Listing 3.11: The function to obtain the number of electrons per cosmic ray.[2]

```
def calculate_flux(adu, gain, exposure_time, stacking_order):
    exp_time = exposure_time/stacking_order
    pixel_flux = []
    flux_cosmic = []
    for group in adu:
        group_values = []
        sum_fluxes = 0
        for i in group:
            flux = (i*gain)/exp_time
            sum_fluxes += flux
            group_values.append(flux)
        flux_cosmic.append(sum_fluxes)
        pixel_flux.append(group_values)

    flux_cosmic = np.array(flux_cosmic)

    return(pixel_flux, flux_cosmic)
```

Listing 3.12: The function to obtain the estimated flux per cosmic ray.

3.2.5. Size of the SAA and the Auroral Zones

The properties calculated above (number of cosmic rays, cosmic ray density and the percentage of pixels affected by cosmic rays) can then be plotted and mapped to investigate changes in size of the SAA and the auroral zones. In order to map the data it is binned and interpolated in order to estimate missing or unknown data points. Listing 3.13 illustrates the binning and interpolation function. Firstly, the data is binned using the `scipy.stats` function `binned_statistic_2d` with the median and a bin size of five. This returns a bidimensional binned array for the dataset. The median is used to avoid outliers

After the array was flattened and potential NaN's (Not a Number) have been removed, the geographic coordinates of the satellite's position, given in latitude and longitude, are converted into 3D cartesian coordinates. This step is done to be able to calculate geometric areas more easily in km^2. In the last step the interpolation is done using a `RBFInterpolator`.

```python
def bin_data_polar(x,y,c,interp_grid_size = 2.5, lon_min = None, lon_max
    = None, lat_min = None, lat_max = None, type = None,):
    from scipy.interpolate import RBFInterpolator

    # set bins and mask SAA contour
    if lon_min is None and lon_max is None:
        lon_min, lon_max = -180, 180
    else:
        lon_min = lon_min
        lon_max = lon_max

    if lat_min is None and lat_max is None:
        lat_min, lat_max = -90, 90
    else:
        lat_min = lat_min
        lat_max = lat_max

    bin_size = 5
    x_bins = np.arange(lon_min, lon_max + bin_size, bin_size)
    y_bins = np.arange(lat_min, lat_max + bin_size, bin_size)

    # bin data
    ret = binned_statistic_2d(x,y,c, statistic='median', bins=[x_bins,
    y_bins])
    statistic = ret.statistic.T
    x_edges = ret.x_edge
    y_edges = ret.y_edge

    # compute bin centers
    bin_centers_x = (x_edges[:-1] + x_edges[1:]) / 2
    bin_centers_y = (y_edges[:-1] + y_edges[1:]) / 2
    X, Y = np.meshgrid(bin_centers_x,bin_centers_y)

    # flatten the arrays
    points_lonlat = np.column_stack([X.ravel(), Y.ravel()])
    values = statistic.ravel()

    # remove NaNs
    mask = ~np.isnan(values)
    valid_points_lonlat = points_lonlat[mask]
    valid_values = values[mask]

    # convert valid lon/lat points into 3D cartesian
    valid_lats = valid_points_lonlat[:, 1]
    valid_lons = valid_points_lonlat[:, 0]
    valid_points_cartesian = latlon_to_cartesian(valid_lats, valid_lons)

    # define finer interpolation grid
    finer_x = np.arange(lon_min, lon_max + interp_grid_size,
    interp_grid_size)
    finer_y = np.arange(lat_min, lat_max + interp_grid_size,
    interp_grid_size)
    Finer_X, Finer_Y = np.meshgrid(finer_x, finer_y)
```

```python

    # convert finer interpolation grid to 3D cartesian
    finer_lats = Finer_Y.ravel()
    finer_lons = Finer_X.ravel()
    finer_cartesian = latlon_to_cartesian(finer_lats, finer_lons)


    # RBF interpolation in cartesian 3D
    interpolator = RBFInterpolator(valid_points_cartesian, valid_values, kernel='linear', smoothing =0)
    finer_values = interpolator(finer_cartesian)
    interpolated = finer_values.reshape(Finer_X.shape)

    lon_mesh, lat_mesh = Finer_X, Finer_Y

    if type == 'density_cosmics':
        # set low values to 1
        mask_low_values = interpolated < 1
        interpolated[mask_low_values] = 1
    elif type in ('percentage_cosmics', 'percentage_cosmics_per_s'):
        # set low values to 0.01
        mask_low_values = interpolated < 0.01
        interpolated[mask_low_values] = 0.01
    elif 'SAA' in (type or ''):
        return interpolator
    else:
        raise ValueError("Please set type to convert low values, conversion ignored")


    return interpolated, bin_centers_x, bin_centers_y, lon_mesh, lat_mesh
```

Listing 3.13: The function to bin and interpolate the data.[3]

To investigate the change in size to the SAA and the auroral zones, the binned and interpolated data of the percentage of cosmic rays are now plotted on a map projection corresponding to the region of interest. In the case of the SAA the Plate carrée projection is used, in the case of the northern and southern auroral zone the north polar- and south polar stereo projections respectively. Utilising a `matplotlib contour` plot, different contours corresponding to different percentages of cosmic rays are drawn. Subsequently, the sizes of the enclosed contours are computed in two ways as illustrated in Listings 3.14 and 3.15.

```python
def area_in_degrees(paths):
    """
    Function to compute the spherical area of polygon.
    """
    area_individual_polygons = []

    for path in paths:
        if path is not None:
            vertices = path.vertices
            codes = path.codes
```

```
            indices = np.where(codes == PATH.MOVETO)[0]
            vertices_segments = np.split(vertices, indices)[1:]

            [...]

            for vertices in vertices_segments:
                area = Polygon(vertices[1:]).area
                area_individual_polygons.append(area)


            area_individual_polygons = np.array(area_individual_polygons)
            area_individual_polygons = -np.sort(-area_individual_polygons)

            total_area_deg = 0
            if len(area_individual_polygons) > 0:
                first_item = area_individual_polygons[0]
                total_area_deg = area_individual_polygons[0]
                for i in range(1, len(area_individual_polygons)):
                        if area_individual_polygons[i] > 0.1*first_item or area_individual_polygons[i] == first_item:
                            total_area_deg += area_individual_polygons[i]
                        elif area_individual_polygons[i] == 0:
                            total_area_deg = 0
                        else:
                            total_area_deg -= area_individual_polygons[i]


            return total_area_deg

        else:
            return 0.0
```

Listing 3.14: The function to compute the spherical area of a polygon in square degrees.[2]

To compute the area in square degrees, as depicted in Listing 3.14, the coordinates of the contour have to be obtained first. For this operation, geographic coordinates (longitude and latitude) are used. The coordinates can be obtained by using the `contour` function, which returns a list of paths with coordinates corresponding to the different contour segments.

Using the list of paths and the `Polygon` function from the `shapely.geometry` library ([Gillies et al., 07]) different polygons are computed according to the number of contours per percentage level. In certain regions, particularly near the poles, a contour may contain one or more, contour(s) within itself, these are referred to as "holes" or "islands" where the area of these contours is lower of higher respectively. It is therefore necessary to subtract the area of a hole and add the area of an island, in order to obtain an accurate area.

The area of the polygons are computed using the corresponding operation from the `shapely` library. In order to identify the holes, the list of contour areas for a specific percentage of pixels affected by cosmic rays is sorted by area size.

The largest of these areas is used as a baseline to compare the others against it and identify if they should be subtracted or added to the total area. The idea is to subtract any area below a certain threshold, in percent of the largest area, from the total. At the time of writing, a threshold of 10% was implemented. This threshold results in areas smaller than 10% of the largest area being considered holes. The areas of identified holes are subtracted from the total area, while all other identified areas are added to the total area.

```
def area_in_kilometres(paths, radius):
    """
    Function to compute the spherical area of a polygon.
    """
    geod = Geodesic(radius, 0) #spherical model with no flattening
    poly = geod.Polygon()
    area_individual_polygons = []
    perimeter_individual_polygons = []

    for path in paths:
        if path is not None:
            total_area_km = 0.0
            vertices = path.vertices
            wrapped_vertices = [(wrap_longitude(lat), wrap_latitude(lon)) for lat, lon in vertices]
            codes = path.codes
            indices = np.where(codes == PATH.MOVETO)[0]
            vertices_segments = np.split(wrapped_vertices, indices)[1:]

            [...]

            for vertices in vertices_segments:
                poly.Clear()
                for pts in vertices[:-1]:
                    poly.AddPoint(pts[1], pts[0])


                _, perimeter, area = poly.Compute()
                perimeter = perimeter/1e3
                perimeter_individual_polygons.append(perimeter)
                area_individual_polygons.append(area)

            area_individual_polygons = np.array(area_individual_polygons)
            area_individual_polygons = -np.sort(-area_individual_polygons)

            if len(area_individual_polygons) > 0:
                first_item = area_individual_polygons[0]
                total_area_km = area_individual_polygons[0]
                for i in range(1, len(area_individual_polygons)):
                    if area_individual_polygons[i] > 0.1*first_item or area_individual_polygons[i] == first_item:
                        total_area_km += area_individual_polygons[i]
                    else:
```

```
                    total_area_km -= area_individual_polygons[i]

        return perimeter_individual_polygons, total_area_km/1e6
    else:
        return 0.0
```

Listing 3.15: The function to compute the spherical area of a polygon in square kilometres.[2]

The process of computing the areas in square kilometres is similar to the one computing the area in square degrees, but has to be treated separately. For this process to work as intended (as seen in Listing 3.15) the orbit height of CHEOPS has to be taken into account. To perform this calculation it is assumed that the satellite's orbit is spherical at an orbit height of 700 km, so the area is calculated along a sphere with a radius of Earth's radius + CHEOPS' orbit height. Therefore, in the beginning of the calculation a spherical model of the aforementioned radius without flattening is computed using the `Geodesic` function of the `geographiclib` library ([Karney, 2023]).

Using the `Path` method from the contour plots, described above, and the `Polygon` function from the `geographiclib` library, again different polygons are computed in accordance with the respective contour. The existence of holes as islands is treated in the same was as in the case of the area computation in square degrees. In this function, in addition to the area, the perimeter of the contours can be computed with the aforementioned library.

3.2.6. Change in location of the SAA and the Auroral Zones

To evaluate the change in location of both the SAA and auroral zones, the previously computed contours and their paths (see Section 3.2.5) are utilised as follows: As illustrated in Listing 3.16 the geographic coordinates are split into longitude and latitude. Subsequently the northernmost, easternmost, southernmost and westernmost coordinates are computed by taking the maximum and minimum values respectively from the longitude and latitude values of the contours.

```
def location_change(paths):
for path in paths:
    vertices = path.vertices
    lon = vertices[:,0]
    lat = vertices[:,1]

    # measure change in location
    north = np.max(lat) if lat.size > 0 else 0
    south = np.min(lat) if lat.size > 0 else 0
    east = np.max(lon) if lon.size > 0 else 0
    west = np.min(lon) if lon.size > 0 else 0
    coords = (north, east, south, west)

return coords
```

Listing 3.16: The function to compute the northernmost, southernmost, westernmost and easternmost points of the previously computed contours.[2]

To evaluate the change in location from within the SAA a representative point is calculated from the four coordiantes above. The computation has been done using the midpoint formula as depicted in equation 3.4. To simplify the calculation it was assumed that the coordinates are located in a plane.

$$x_{\text{mid}} = \frac{x_1 + x_2}{2} \tag{3.4}$$

3.2.7. Cosmic Rays and the Solar Cycle

The last property, to be examined, is whether the solar cycle has an effect of the density of cosmic rays within the SAA. Therefore, the solar Kp- and ap-indices, a representation of the sun's activity (see Chapter 2.3.1), are obtained from the Helmholtz Centre for Geosciences ([Matzka et al., 2021]). Using their database, the daily Kp- and ap-indices over the 4.5 years of data are retrieved and binned for different timeframes ranging from daily to monthly. Both indices can be plotted separately and each can be compared with the mean density of cosmic rays.

The mean density of cosmic rays is computed by firstly computing the density of cosmic rays in general (see Section 3.2.2). The data are subsequently binned and interpolated within the geographical coordinates of the SAA using the function depicted in Listing 3.13. Lastly the mean from the binned data is computed using the `np.nanmean` function to disregard potentially occurring NaNs.

4. Results and Analysis

This chapter presents the results and data analysis performed to be able to answer the previously posed research questions. The original research question posed is how the size and location of the SAA change over the course of 4.5 years and also whether similar anomalies are present on the globe at CHEOPS orbit height and if so how they behave. During the development of the processing pipeline, additional research questions emerged, such as whether possible correlations exist between the behaviour of the SAA and the solar cycle as well as how the fluxes of the detected cosmic rays generally behave.

It was found that the SAA is not the only region of the Earth's magnetic field that warrants a closer inspection. As the investigated phenomenon is also in part responsible for the occurrence of auroras, the auroral zones around the poles present similarly interesting targets.

To characterise the development of the size and location of the SAA and auroral zones, the percentage of pixels affected by cosmic rays is mapped on a world map according to the position of the satellite. As mentioned in Chapter 3 and section 3.2.5 data inside the SAA was not available through most of the evaluated timespan from 1st July 2020 to 31st December 2024, therefore, most data retrieved and used, stem from the edges of the anomaly. With the help of the sparse data from inside the anomaly and the data from the edges, data inside the SAA was interpolated.

From there, different predetermined filters were applied to further narrow down the investigated parameters. The filters include but are not limited to the timeframe, geographical location, inclusion of stray light images and property to investigate (e.g. density of cosmic rays). The data were subsequently looked at in different time intervals to determine whether a change in size and or location was discernible.

4.1. Characterisation of the South Atlantic Anomaly

The following sections detail the results of the characterisation of the SAA concerning the change of size as well as the change in location. The percentage of pixels (in the following "pixel percentages") affected by cosmic rays was investigated in different time intervals of 6 months, 12 months and 4.5 years. Five different pixel percentages, 0.1%, 1%, 2%, 5% and 10%, were chosen in order to investigate the aforementioned properties. These percentages were kept constant throughout the different time intervals, even when no contour could be drawn due to a lack of data. For the purpose of analysis, the 0.1% contour is chosen for subsequent comparisons, as it provides a comprehensive look at the

SAA compared to the most recent published data (see Figure 2.11). In order to analyse changes in size of the contours, we track their surface area (in square degrees). The raw data tables in Appendix A.1 also give the measured areas in km^2 The figures within this section depict the data measured over the globe. The numeric data was calculated using SAA data truncated between the latitudes -55° and 10°.

4.1.1. Change in Size

As described above, a change in size throughout the 4.5 years of observation was observed first qualitatively via the images and later analysed quantitively by comparing the percentages of pixels affected by cosmic rays. The detailed procedure is described in Section 3.2.3.

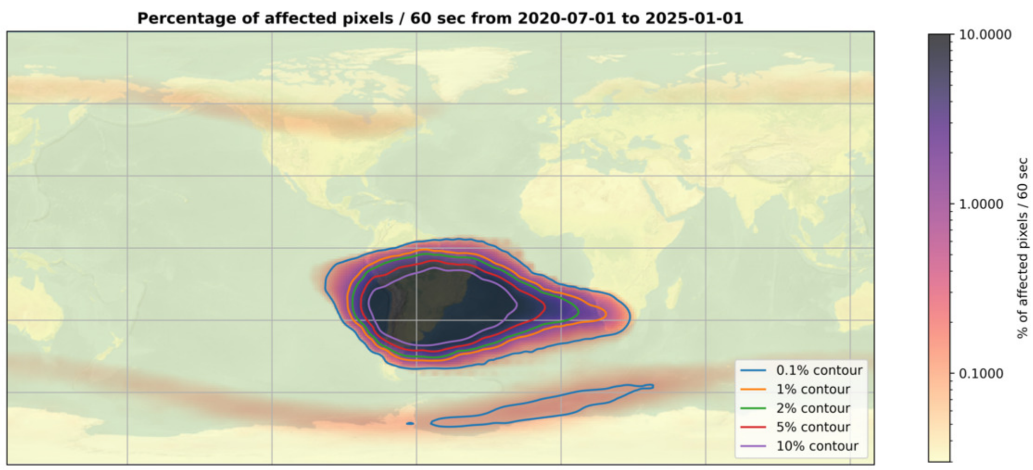

Figure 4.1.: Percentage of affected pixels per minute during SAA visits over the course of 4.5 years. The blue outermost contour corresponds to a percentage of 0.1% of pixels affected by cosmic rays. The other orange, green, red and purple contours cossrespond to percentages of 1%, 2%, 5% and 10% of pixels affected by cosmic rays respectively.

Figure 4.1 depicts the size of the SAA using all available data over 4.5 years of data acquisition. It is apparent that, as mentioned above, the 0.1% contour is the most suitable to draw conclusions. As suggested in Table A.5 and the area of the 0.1% contour is measured to span 4597.64 deg^2.

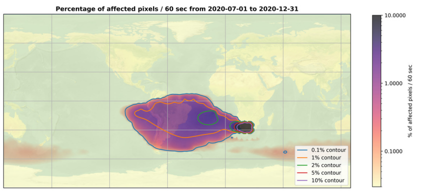

(a) 01-07-2020 to 31-12-2020

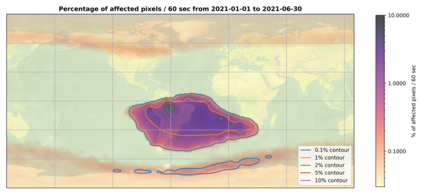

(b) 01-01-2021 to 30-06-2021

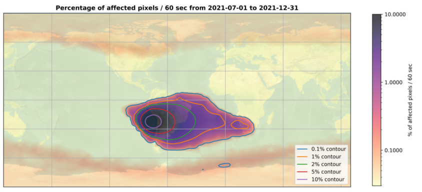

(c) 01-07-2021 to 31-12-2021

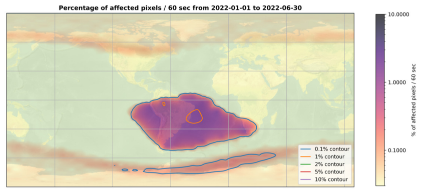

(d) 01-01-2022 to 30-06-2022

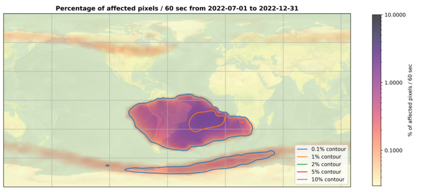

(e) 01-07-2022 to 31-12-2022

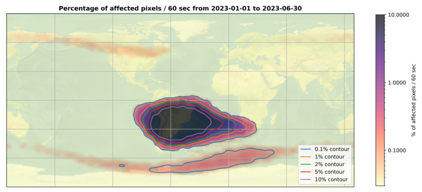

(f) 01-01-2023 to 30-06-2023

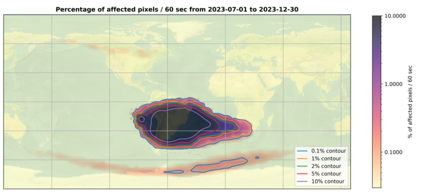

(g) 01-07-2023 to 31-12-2023

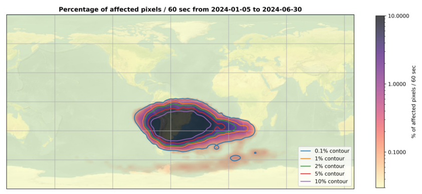

(h) 01-01-2024 to 30-06-2024

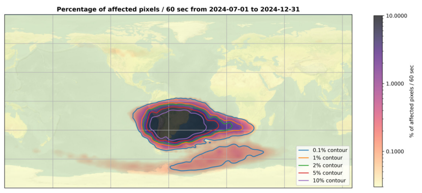

(i) 01-07-2024 to 31-12-2024

Figure 4.2.: Percentages of pixels affected by cosmic rays normalised per minute during SAA visits at 6-month intervals. The blue outermost contour corresponds to a percentage of 0.1% of pixels affected by cosmic rays. The other orange, green, red and purple contours cossrespond to percentages of 1%, 2%, 5% and 10% of pixels affected by cosmic rays respectively.

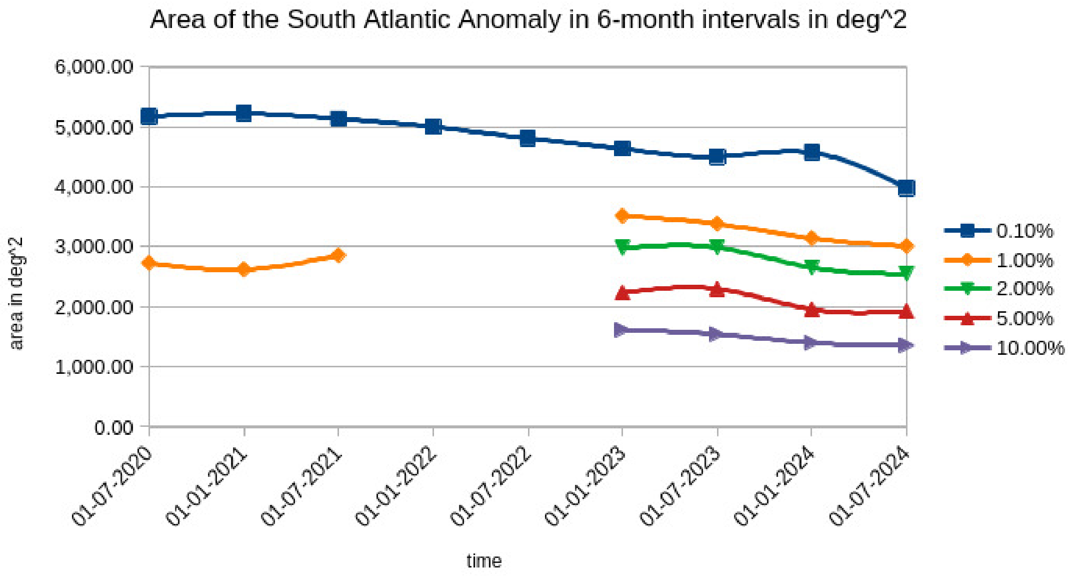

Figure 4.3.: Change in size of the SAA in square degrees over 4.5 years of observation at 6-month intervals. Data points that proved inconclusive were removed. The blue graph corresponds to the 0.1% contour. The other orange, green, red and purple grpahs cossrespond to the 1%, 2%, 5% and 10% contours respectively.

Figure 4.2 depicts the development of the SAA at 6 month intervals. It is noticeable that not every contour could be drawn for every year (see Figures 4.2d and 4.2e) or are somewhat inconclusive (see Figure 4.2a) due to no data collected from within the SAA and only interpolating the data from the edges.

When inspecting the data at 6 month intervals (see Figure 4.2) and Figure 4.4 it is apparent, that the size decreases over time. According to the criteria mentioned above, the area of the SAA in the first half of 2021 is measured to be 5225.79 deg^2. Over time the area is steadily decreasing with only a small increase being observed in the first half of 2024. Until the end of 2024, the area has decreased to 3981.57 deg^2, which marks approximately a 23% decrease in area over these 3.5 years. When taking into account the data for 2020 and 2022, the trend is similarly observable.

4.1.2. Change in Location

Alongside the change in size, the change in location of the SAA was investigated using its geographic coordinates. As described in Section 3.2.6 the northernmost, easternmost, southernmost and westernmost coordinates of the anomaly were measured. Similarly to the change in size, the locations were computed for the aforementioned five different pixel percentages of 0.1%, 1%, 2%, 5% and 10% as well as at the intervals of 6 months, 12 months and the entire data set of 4.5 years.

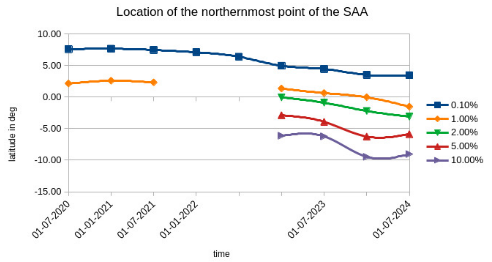

(a) Latitude coordinate of the northernmost point.

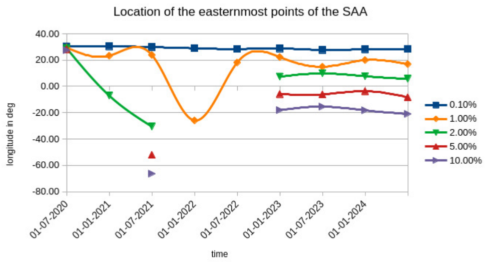

(b) Longitude coordinate of the easternmost point.

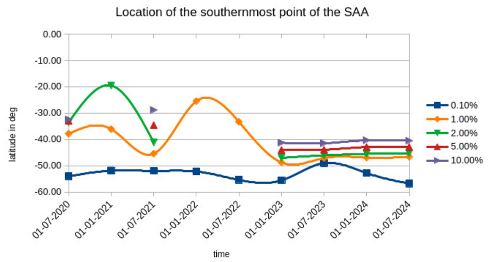

(c) Latitude coordinate of the southernmost point.

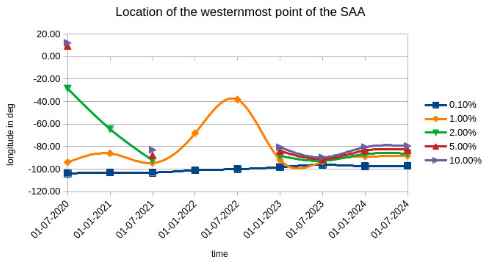

(d) Longitude coordinate of the westernmost point.

Figure 4.4.: Coordinates of the most northern, eastern, southern and western points of the SAA at 6-month intervals. The blue graph corresponds to the 0.1% contour. The other orange, green, red and purple grpahs cossrespond to the 1%, 2%, 5% and 10% contours respectively.

Figure 4.4 depicts the changes in location of the four cardinal directions from north (Figure 4.4a) to south (Figure 4.4c). Inspecting the 0.1% contour and excluding the years of 2020 and 2022 as before only minor changes in location are present. As illustrated in Table A.8 the northernmost point follows a southward trend and and changes by an average of 0.88° northward per half-year going from a maximum latitude of 7.64° in the first half of 2021 to a minimum of 3.45° in the second half of 2024. Taking into account the previously excluded years 2020 and 2022, this trend continues steadily and the semiannual average only decreases slightly to 0.52° southward. Investigating the southernmost point and using the previous constraints reveals a non-steady behaviour with a northward trend in the years 2020, 2021 and 2022 and a southward trend in the years 2023 and 2024. Over these data points, the location of the southernmost point changes by an average of 0.86° northward semiannually. Taking all data points into account, the semiannual average decreases to 0.27° northward. Figures 4.4b and 4.4d depict the changes in location of the easternmost and westernmost points of the SAA. Using the 0.01% contour and taking only the years 2021, 2023 and 2024 into account, the location of the easternmost point does not change significantly and only moves by a semiannual average of 0.42° westward. Looking at the entirety of the data reveals that the semiannual average decreases to 0.24° westward. The location of the westernmost point is changing the most throughout the 4.5 years of data using the previously mentioned constraints. There is a steady eastward trend of, on average, -1.18° semiannually using only the data of 2021, 2023 and 2024. Analysing the whole data this average decreases to -0.85° eastward, still marking the largest change in location.

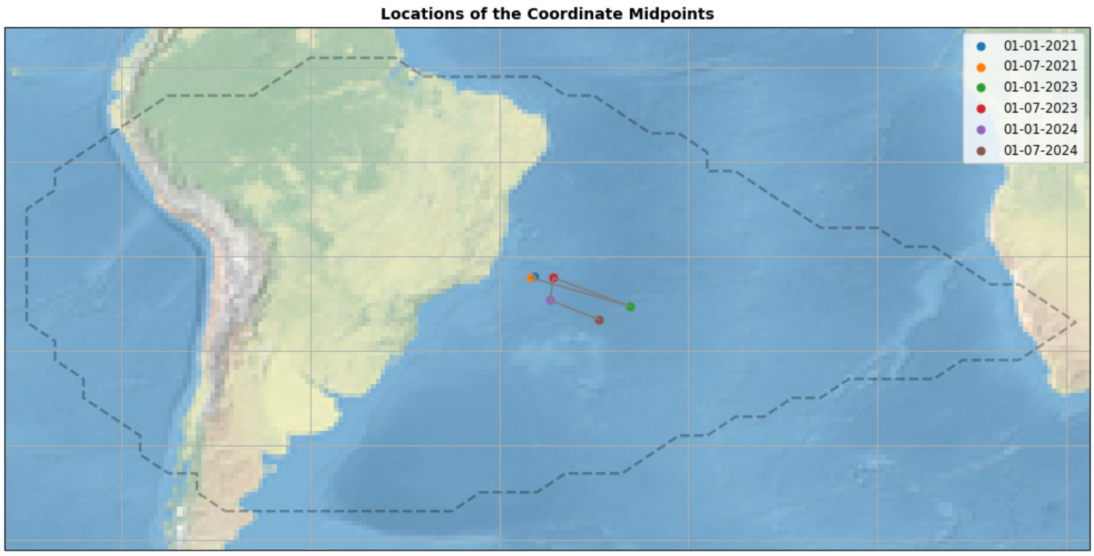

Figure 4.5.: Locations of the midpoints of the northernmost, easternmostm, southernmost and westernmost coordinates for the years 2021, 2023 and 2024 in 6-month intervals. The dashed line represents the contour of the SAA mask used by CHEOPS until March 2025. The light grey lines represent the path of the movement.

Figure 4.5 depicts the locations of the calculated midpoints of the northernmost, easternmost, southernmost and westernmost coordinates for the years 2021, 2023 and 2024 in 6-month intervals. The years of 2020 and 2022 were excluded from the plot because no data within the SAA was acquired during those years. The location data for all years can be found in Table A.7. It is apparent that the midpoints move in a zig-zag pattern, therefore not providing a conclusive trend in a singular direction.

4.2. Characterisation of the Auroral Zones

Figures 4.11 and 4.6 depict five different percentages chosen to investigate the change in size of the auroral zones over the Arctic and Antarctic. Different percentages are chosen for the two different zones to accommodate the different geomagnetic properties, leading to more or less cosmic rays to be detected. In the case of the arctic auroral zone, where data was analysed between the latitudes of 90° N and 50° N, the following percentages were initially chosen: 0.05%, 0.06% and 0.07%. Since in some cases there were not enough data points to facilitate comprehensive contours for the three mentioned percentages, two additional percentages were calculated in these cases: 0.03%, 0.04%. However, because these smaller percentages come close to the value of noise, they were only computed if necessary.

For the antarctic auroral zone, data was analysed between the latitudes of 90° S and 50° S. 0.075%, 0.08%, 0.09%, 0.1%, and 0.125% were the percentages chosen for the antarctic auroral zone. Similarly to the characterisation of the SAA, different time intervals of 6-months, 12-months and 4.5 years were analysed with the results being presented in the following sections.

4.2.1. Antarctic Auroral Zone

To characterise the antarctic auroral zone, the aforementioned percentages of 0.075%, 0.08%, 0.09%, 0.1% and 0.125% were used to characterise the changes in size and location. The data were analysed and interpolated between latitudes 50° S and 90° S. Similarly to before, the data was analysed in different time intervals of 6-months and 12-months as well as over the 4.5 years of data acquisition.

4.2.1.1. Change in Size

Figure 4.6 shows 4.5 years of data, inspecting the size of the antarctic auroral zone. When investigating the size of the southern auroral zone, the 0.075% and 0.08% contours are used to determine potential changes in size. These percentages represent a visual estimate of the location of the antarctic auroral zone. In the case of the entire 4.5 years of data, those areas, as illustrated in Table A.15, measure 1287.71 deg^2 and 1113.81 deg^2 respectively.

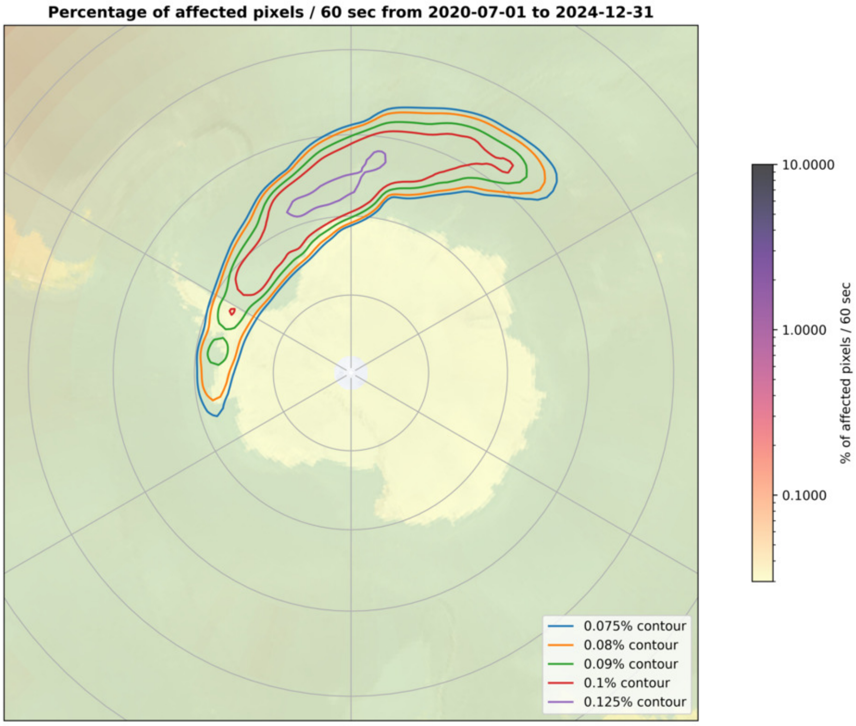

Figure 4.6.: Percentage of affected pixels per minute during flights over the antarctic over 4.5 years of data acquisition. The blue outermost contour corresponds to a percentage of 0.075% of pixels affected by cosmic rays. The other orange, green, red and purple contours cossrespond to percentages of 0.08%, 0.09%, 0.1% and 0.125% of pixels affected by cosmic rays respectively.

As depicted in Figures 4.7 and 4.8 and illustrated in Figure 4.9 the general size of the antarctic auroal zone grows and shrinks periodically every two years. Although due to unexpected behaviour of the antarctic auroral zone in 2024 the data points from that year were disregarded in the analysis. Within this year the antarctic auroral zone moves northward so much so that it moves outside the investigated latitude.

As seen in Figures 4.7a,4.7b and 4.7c the background density of cosmic rays is much higher in comparison to the following years. Investigating the 0.075% and 0.08% contours at 6-month intervals,a similar behaviour is revealed both throughout the years as well as in comparison to the other percentages. The area measurements vary between a maximum of 2565.95 deg^2 and 2286.89 deg^2 in 2020 and a minimum of 1166.67 deg^2 and 853.30 deg^2 in the second half of 2021 for the 0.075% and 0.08% contours respectively.

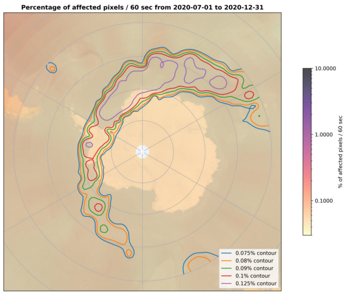

(a) 01-07-2020 to 31-12-2020

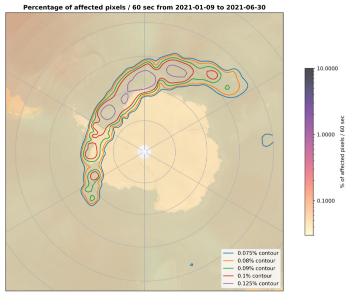

(b) 01-01-2021 to 30-06-2021

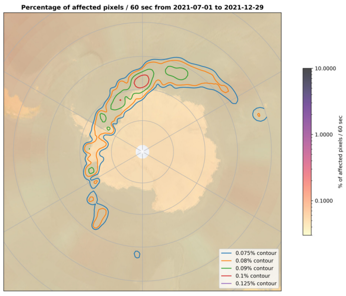

(c) 01-07-2021 to 31-12-2021

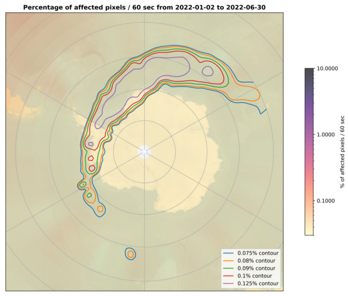

(d) 01-01-2022 to 30-06-2022

Figure 4.7.: Percentages of pixels affected by cosmic rays normalised per minute during SAA visits at 6-month intervals from 01-07-2020 to 30-06-2022.. The blue outermost contour corresponds to a percentage of 0.075% of pixels affected by cosmic rays. The other orange, green, red and purple contours correspond to percentages of 0.08%, 0.09%, 0.1% and 0.125% of pixels affected by cosmic rays respectively.

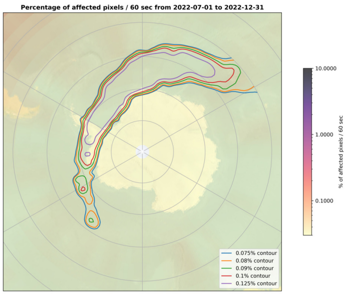

(a) 01-07-2022 to 31-12-2022

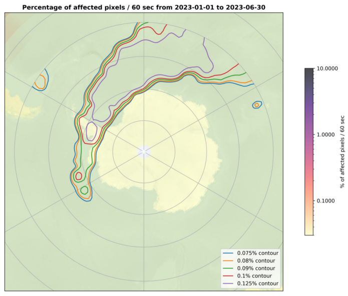

(b) 01-01-2023 to 30-06-2023

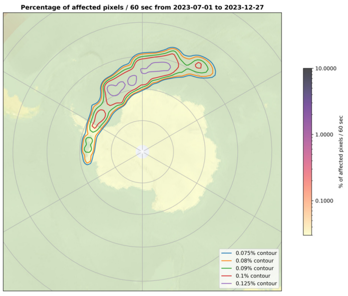

(c) 01-07-2023 to 31-12-2023

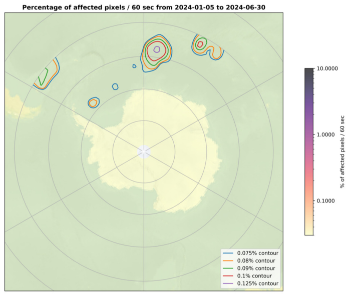

(d) 01-01-2024 to 30-06-2024

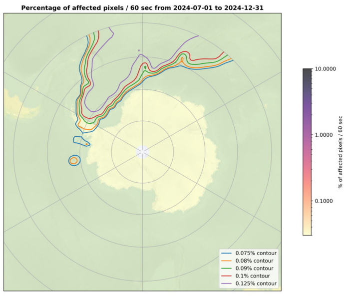

(e) 01-07-2024 to 31-12-2024

Figure 4.8.: Percentages of pixels affected by cosmic rays normalised per minute during SAA visits at 6-month intervals 01-07-2022 to 31-12-2024. The blue outermost contour corresponds to a percentage of 0.075% of pixels affected by cosmic rays. The other orange, green, red and purple contours correspond to percentages of 0.08%, 0.09%, 0.1% and 0.125% of pixels affected by cosmic rays respectively.

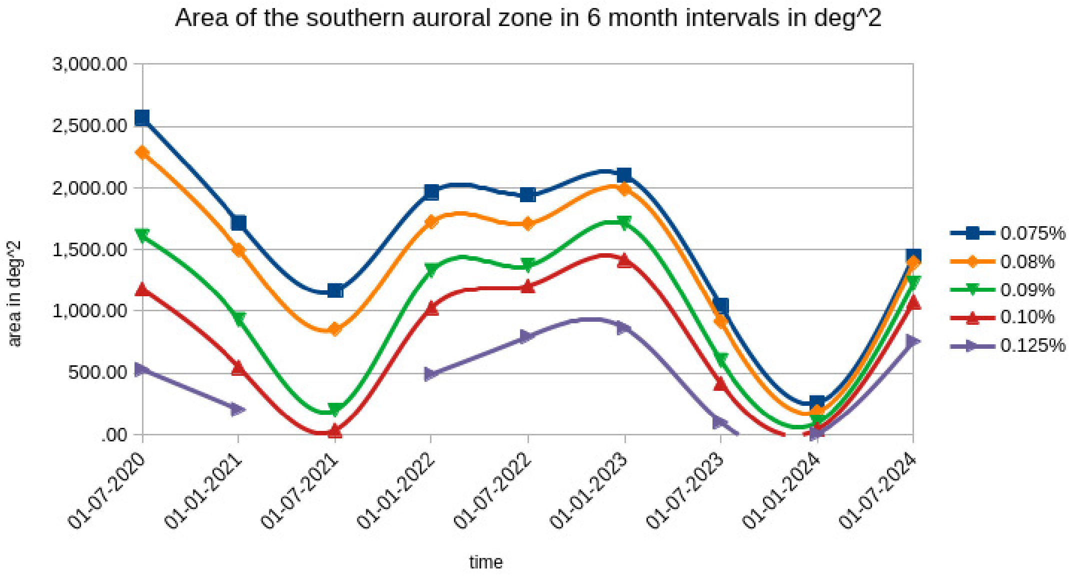

Figure 4.9.: Change in size of the southern auroral zone in square degrees over 4.5 years of observation in 6-month intervals. The blue graph corresponds to the 0.075% contour. The other orange, green, red and purple grpahs cossrespond to the 0.08%, 0.09%, 0.1% and 0.125% contours respectively.

Disregarding the data from 2024, the area of the 0.075% and 0.08% contours first decrease until the second half of 2021 before increasing again and remaining stable during 2022 and the first half of 2023. Towards 2024 another decrease in area is observable. This trend is noticeable throughout the different contours, with the exception of the 0.125% contour for which no data were available in the second half of 2021.

4.2.1.2. Change in Location

Similarly to the SAA the northernmost, easternmost, southernmost, and westernmost points of the different contours were computed. The antarctic auroral zone can be described as a circle, therefore,in this case, it is expected that the easternmost and westernmost points converge. As suggested in Figures 4.7 and 4.8, visually this is not the case. However, as seen in Figures 4.10b and 4.10d both points are almost converging at $\pm 180°$ in the beginning and throughout the years approaching each other, with the tendency to move toward and in some cases intersecting the prime meridian. The development over time of both coordinates look similar although mirrored. Furthermore, it is apparent that all contours display a similar behaviour. Investigating the northernmost point it is discernible that there are contours not reaching the northern boundary of 50°, especially in the year 2021. However, for the other data points the two contours of interest, 0.075% and 0.08%, reach the northern boundary in all but one case (0.08% contour in the first half of 2023) as seen in Table A.17.

The behaviour of the southernmost point is equal for the three contours 0.075%, 0.08%, and 0.09%. In this case, it moves northward throughout the years. For the two higher percentages, the locations fluctuate between moving north and coming back south before eventually moving northward again.

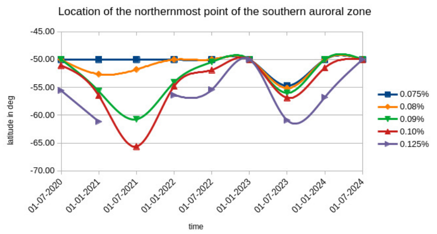

(a) Latitude coordiante of the northernmost point.

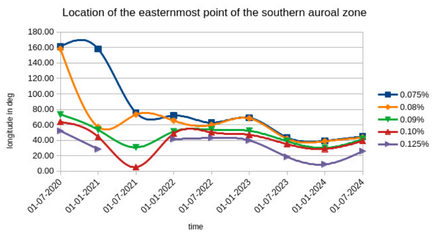

(b) Longitude coordiante of the easternmost point.

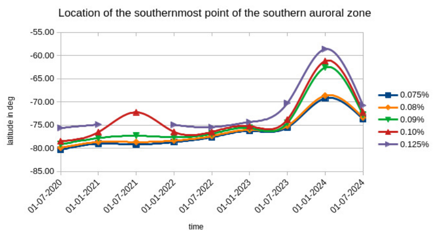

(c) Longitude coordiante of the southernmost point.

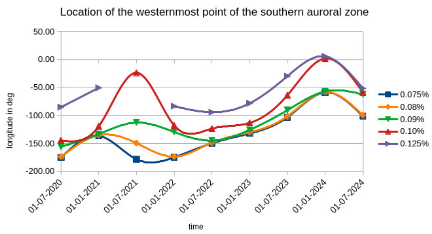

(d) Longitude coordinate of the westernmost point.

Figure 4.10.: Coordinates of the most northern, eastern, southern and western points of the southern auroral zone at 6-month intervals. The blue graph corresponds to the 0.075% contour. The other orange, green, red and purple grpahs cossrespond to the 0.08%, 0.09%, 0.1% and 0.125% contours respectively.

4.2.2. Arctic Auroral Zone

The arctic auroral zone was characterised based on a potential change in size and location. As mentioned above, the percentages used to investigate these properties range from 0.05% to 0.07% with two additional percentages 0.03%, 0.04% added if necessary.

4.2.2.1. Change in Size

Figure 4.11 shows the size of the arctic auroral zone using the entirety of the data calculated over the timespan of 4.5 years. Noticeably, the contours are cut off at a latitude of 50° due to the restriction of the interpolation as well as the chosen percentages do not exceed 0.05%. For the analysis of a change in size the 0.04% contour is chosen as this seems to trace the auroral oval the best (see Chapter 2.3.3).

From this point onward visually tracing the auroral oval to compare the change in size is necessary as not all plots have comparable data in the same percentage. As a quantitative comparison, the 0.05% percentage will be showcased, despite the vast range of values, due to all plots containing contours at this percentage.

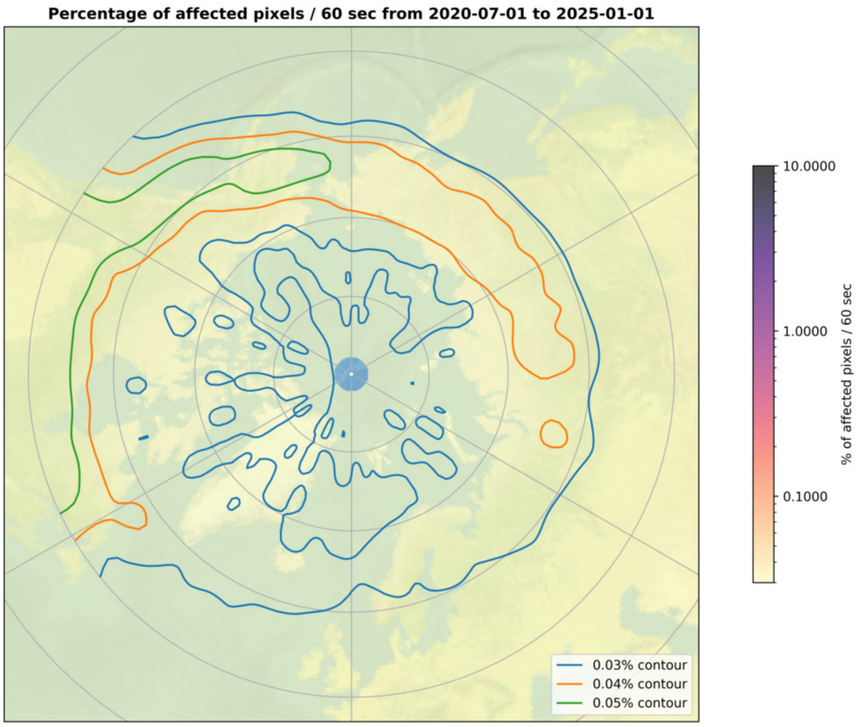

Figure 4.11.: Percentage of affected pixels per minute during flights over the arctic over 4.5 years of data acquisition. The blue outermost contour corresponds to a percentage of 0.03% of pixels affected by cosmic rays. The other orange and green contours cossrespond to percentages of 0.04% and 0.05% of pixels affected by cosmic rays respectively.

As illustrated in Table A.24, the area of the 0.04% contour is measured to be 845.05 deg^2. In comparison, the 0.05% contour has a measured area of 499.96 deg^2. Figure 4.12 depicts all half-yearly data with enough cosmic rays to plot and measure the different percentage contours. The second halfs of 2023 and 2024 (see Figure 4.12g) are the only ones where it was necessary to compute the contours for the two additional percentages of 0.03% and 0.04%. Figure 4.13 illustrates the evolution of the size of the arctic auroral zone.

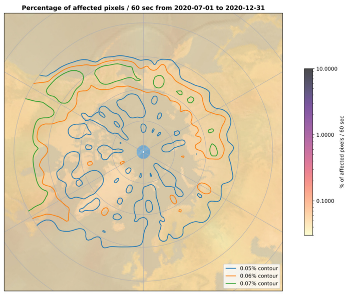

(a) 01-07-2020 to 31-12-2020

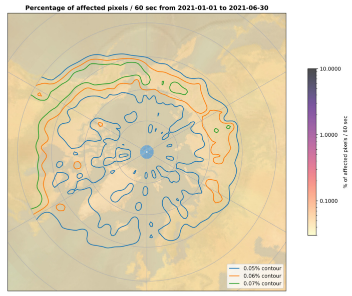

(b) 01-01-2021 to 30-06-2021

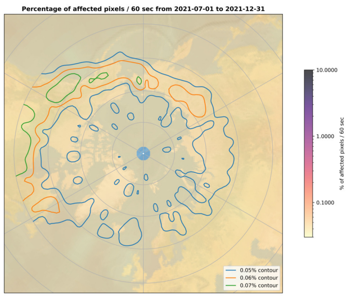

(c) 01-07-2021 to 31-12-2021

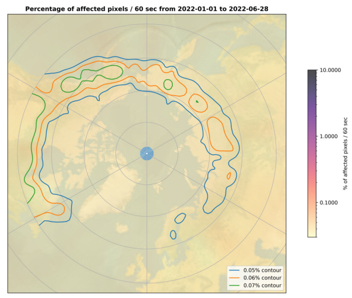

(d) 01-01-2022 to 30-06-2022

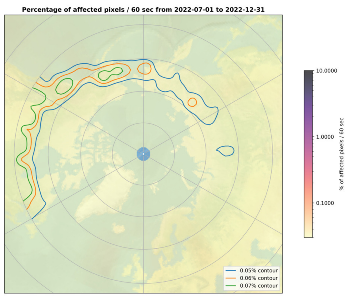

(e) 01-07-2022 to 31-12-2022

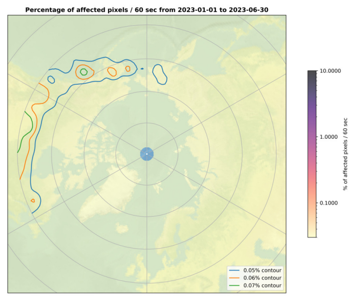

(f) 01-01-2023 to 30-06-2023

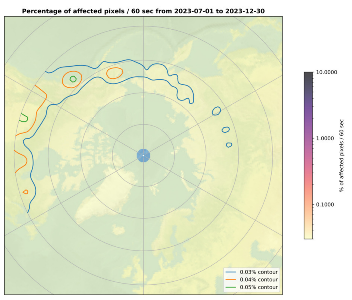

(g) 01-07-2023 to 31-12-2023

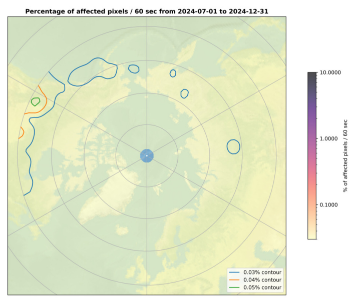

(h) 01-07-2024 to 31-12-2024

Figure 4.12.: Percentages of pixels affected by cosmic rays normalised per minute during SAA visits at 6-month intervals. From 2020 to the first half of 2023 the blue outermost contour corresponds to a percentage of 0.05% of pixels affected by cosmic rays. The other orange and green contours correspond to percentages of 0.06% and 0.07% of pixels affected by cosmic rays respectively.

Certain timeframes (the years 2023 and 2024) have to be excluded due to insufficient or inconclusive data. Only the data from the years of 2020, 2021 and 2022 were considered based on a visual inspection of the auroral zone. It is apparent, from the plot, that the size descreases over time, especially when looking at the 0.05% and 0.06% contours, which are present in all three images. Table A.20 quantitively describes the evolution. Looking at the aforementioned 0.05% contour values to compare the difference in size it reveals a decrease of 1845.53 deg^2 from the maximum in 2020 (1851.73 deg^2) to the minimum in the second half of 2024 (6.43 deg^2). From the visual inspection of the auroral oval, the percentages that match the best are 0.06%, 0,05% and 0.03% for the years 2020 and 2022 respectively. Comparing those, the areas are calculated to be 813.38 deg^2 and 956.92 deg^2 respectively, revealing an increase in size by 143.54 deg^2 followed by a significant decrease of 317.98 deg^2 as seen in Table A.22.

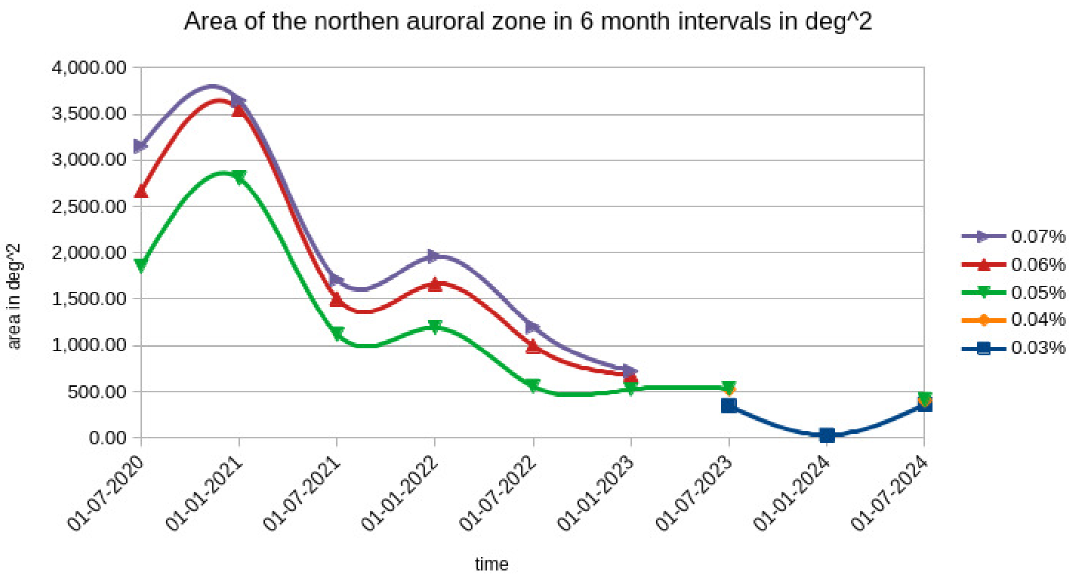

Figure 4.13.: Change in size of the northern auroral zone in square degrees over 4.5 years of observation in 6-month intervals. For the first half of 2024, there was insufficient data to analyse the area. The blue graph corresponds to the 0.03% contour. The other orange, green, red, and purple graphs cossrespond to the 0.04% and 0.05% contours respectively.

For 2020 and the two half years of 2021 the 0.06% contour is considered a suitable visual representation of the auroral oval, as well as the 0.05% contour for the two half-years of 2022. Visually, the contours appear to not change significantly in size, especially after the first half of 2021 but as illustrated in Table A.20, there are significant changes in size present. When looking at Figure 4.13 it is apparent, that a fluctuation in size with a general downward trend is present throughout the time intervals as well as percentages, whether inspecting the visual auroral ovals or the common 0.05% percentage contours.

Considering the quantitative data from the visual inspection (0.06% from 2020 to 2021, 0.05% for 2022), the maximum area is 1188.46^2 measured in the first half of 2022. The minimum area is measured in the second half of 2021 with an area of 385.35 deg^2. In between the maximum and minimum area, significant fluctuations occur, especially between the first half of the respective year and the second half of the respective year. As mentioned above, a general downward trend is observable over all. Similarly, this general downward trend with fluctuations between the first and second half of the respective years is noticeable regarding the 0.05% percentage.

4.2.2.2. Change in Location

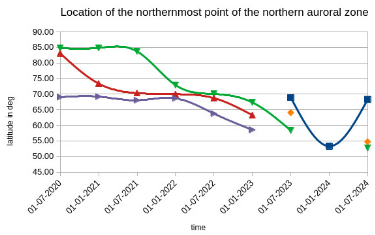

(a) Latitude coordinate of the northernmost point.

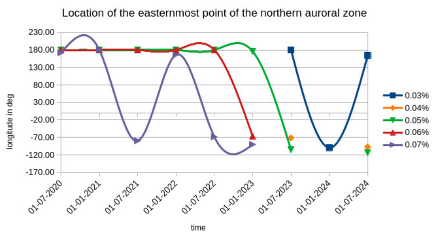

(b) Longitude coordinate of the easternmost point.

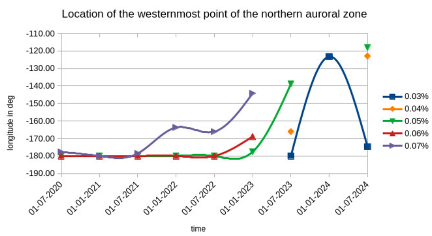

(c) Longitude coordinate of the westernmost point.

Figure 4.14.: Coordinates of the most northern, eastern, and western points of the northern auroral zone at 6-month intervals. No plot of the southernmost point was attached, as the data was only interpolated up to a latitude of 50°. The blue graph corresponds to the 0.03% contour. The other orange, green, red, and purple graphs cossrespond to the 0.04% and 0.05% contours respectively.

To evaluate the change in location of the northern auroral zone, the northernmost, easternmost and westernmost points are computed. The value for the southernmost point is computed as well, but as seen in Table A.26 it does not change over the course of the years or the different percentages. Similarly to the characterisation of the size only the data from the years 2020 to 2022 is taken into account due to insufficient data. Over the three observed cardinal directions, a change in location is discernible, especially considering the northernmost point of the auroral zone, which is wandering south.

As the auroral zone is generally considered to be a circle around the pole, the eastern and western points are expected to converge, which is generally true for certain lower percentages. Using the same constraints as above, the measured data suggest otherwise, giving two distinct points that change location over time but seem to approach one another, with the easternmost point approaching negative and the westernmost point approaching more positive longitudes. This is illustrated in Figure 4.14.

4.3. Other Properties of Cosmic Rays

4.3.1. Flux of Cosmic Rays

The photoelectric flux of cosmic rays was measured as described in Section 3.2.4 with the data points being depicted in Figure 4.15. The flux of each detected cosmic ray is plotted as a histogram with 100 bins. In total, the flux of 18449 cosmic rays over 42 singular science visits spaces out over the entire 4.5 years being measured. The plot shows the great span of fluxes between 0.00 and 1 200 000 e^{-} s^{-1} pixel^{-1}. Most of the fluxes measured lie between 0.00 and 200 000 e^{-} s^{-1} pixel^{-1} with some high-flux outliers above.

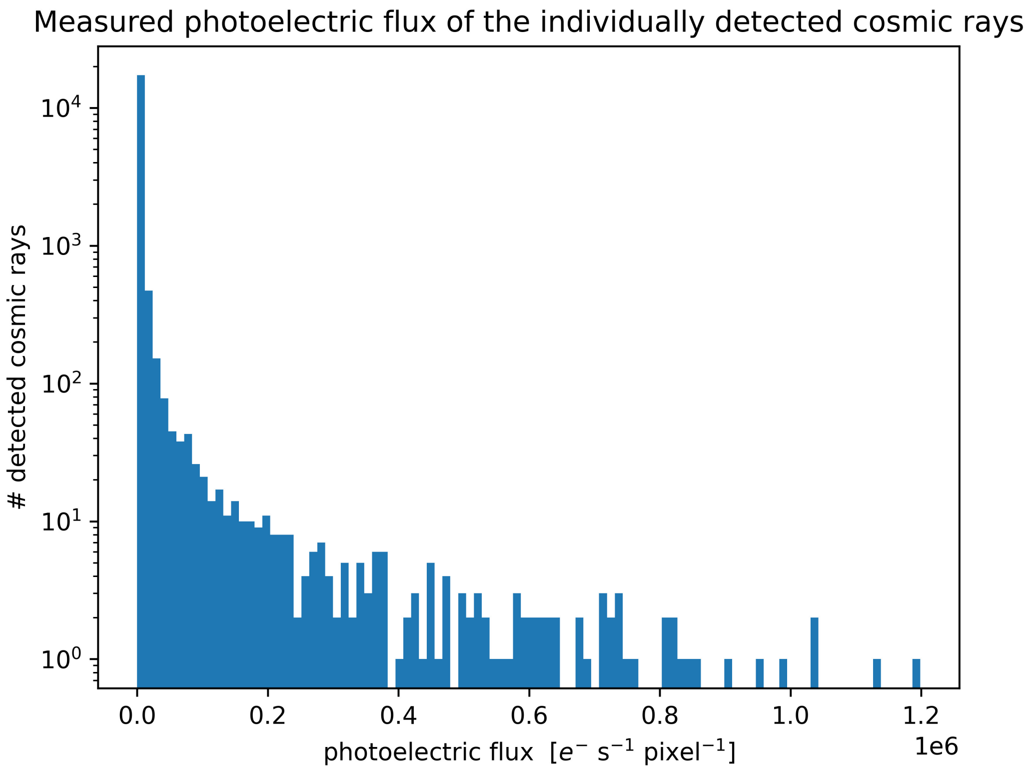

Figure 4.15.: Histogram of the fluxes of the detected cosmic rays.

4.3.2. Cosmic Rays and the Solar Cycle

To investigate if the mean density of cosmic rays is impacted by the solar cycle, the aforementioned property was plotted against two different indices quantifying fluctuations in the Earth's magnetic field (see Chapter 2.3.4) over the 4.5 years of observation. All the data were binned for different time intervals from daily to monthly as described in Chapter 3.2.7.

4.3.2.1. Kp-Index

The planetary K-index (Kp-index) has been plotted alongside the mean cosmic density in the aforementioned time bins as depicted in Figure 4.16. The grey lines depict the evaluation of the Kp-index whereas the blue lines represent the mean density of cosmic rays. From 2020 to 2024, the Kp-index is expected to behave in an upward trend due to the 11-year solar cycle approaching a solar maximum in 2024, which is apparent from all three images. However, significant increases in mean cosmic ray density are likewise represented as increases in the Kp-index. This is best represented by the weekly binning, but also noticeable in the daily and monthly bins. Two geomagnetic storms in 2024 are clearly visible when looking at the Kp-index, but also when investigating the mean cosmic ray density in the weekly bins.

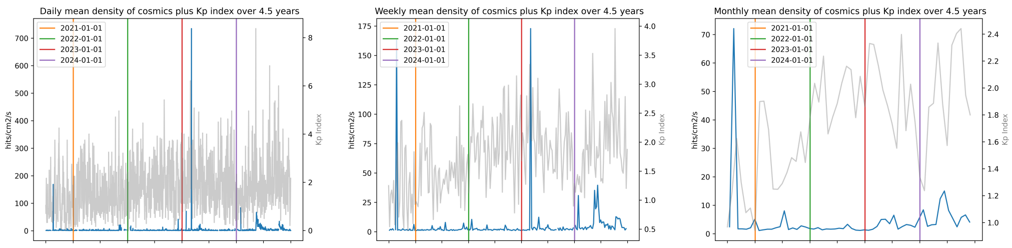

(a) Daily binning. (b) Weekly binning. (c) Monthly binning.

Figure 4.16.: The mean density of cosmic rays over the timespan of 4.5 years plus the solar Kp-index. The different plots illustrate the data in different bins reaching from daily to monthly.

4.3.2.2. ap-Index

Similarly to the Kp-index, the planetary a-index (ap-index) was investigated. As both indices trace geomagnetic activity, the behaviour of the ap-index is expected to be alike. Figure 4.17 portrays the mean density of cosmic rays and the ap-index in differently timed bins. Compared to the behaviour of the mean density of cosmics next to the Kp-index, the mean density of cosmics trace higher ap-indices even better. This is again particularly noticeable when looking at the weekly binning (Figure 4.17b). Especially apparent is an increase in cosmic ray density just after major geomagnetic storms in May and October 2024.

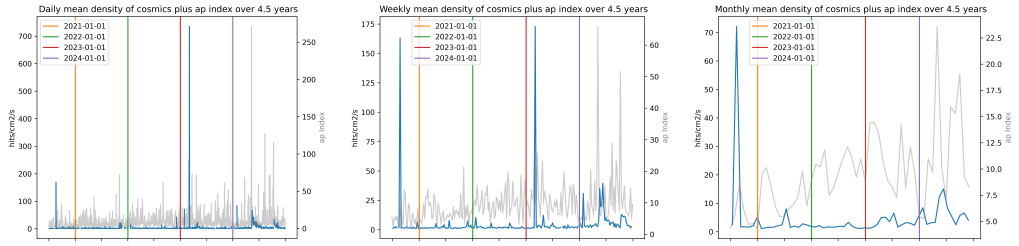

(a) Daily binning. (b) Weekly binning. (c) Monthly binning.

Figure 4.17.: The mean density of cosmicrays over the timespan of 4.5 years plus the solar ap-index. The different plots illustrate the data in different bins reaching from daily to monthly.

5. Discussion

The purpose of this thesis is to characterise the SAA and other regions of interest on the globe at the altitude of CHEOPS by using leftover cosmic ray data from the CHEOPS satellite. This chapter discusses the findings related to the characterisation of the aforementioned SAA and how these fit into the current understanding of the anomaly. In addition,a discussion of the findings connected to the characterisation of the northern- and southern auroral zones is is presented. Furthermore, the analysis of the overall fluxes of the detected cosmic rays as well as correlations between the occurrence of cosmic rays and the solar activity are discussed. The chapter concludes with a discussion of challenges encountered in any step of the process.

The discussions within this chapter are designed to answer the following research questions:

1. Are the sizes of the SAA and the auroral zones changing over time? If so, how?
2. Are the locations of the SAA and the auroral zones changing over time? If so, how?
3. Is there a correlation between the solar cycle and the occurrence of cosmic rays?
4. How are the fluxes of the cosmic rays distributed?

It was found that over the course of 4.5 years of data acquisition, not only the SAA but also both auroral zones show significant decreases in size. Additionally, all the investigated regions display changes in location. The auroral zones around the poles were found to move toward the equator, whereas the SAA moves in a southwesterly direction. Examinations of the occurrence of cosmic rays in relation to the solar cycle reveal that instances of heightened solar activity results in a higher measured density of cosmic rays. Lastly, it was found that the flux of the detected cosmic rays can go as high as 31 521 536.25 e^{-} s^{-1} pixel^{-1}, with the vast majority of the fluxes not exceeding 200 000 e^{-} s^{-1} pixel^{-1}.

5.1. Characterisation of the South Atlantic Anomaly

Investigating the SAA over 4.5 years revealed a 23% decrease in area over the time span of 4 years, excluding data where no data from the inside of the SAA was available. This finding directly contradicts studies done by [Pavón-Carrasco and De Santis, 2016] and [Amit et al., 2021] among others, which agree on a growth of the anomaly. However, the aforementioned studies all investigate the growth over multiple decades or centuries, leading to the assumption that the finding presented in this thesis is a short-term observation. [Fürst et al., 2009] mentions an anti-correlation between the solar activity and the extent of the SAA due to the increased solar radiation compressing the magnetosphere.

This compression subsequently reduces the volume of the Van Allen radiation belts, pushes them closer to Earth's surface resulting in a shrinkage in surface area of the SAA. This opens a possible explanation for the findings of this thesis, as the solar cycle approached a maximum in 2024, coinciding with the strongest decrease in size over the observed timeframe. It also has to be taken into account, that for the years where no SAA data was available, the edge of the 0.1% contour might occasionally penetrade the interpolation zone.

This leads to a potential artificial expansion or reduction of the 0.1% contour. Similarly in the second half of 2024, the northward movement of the southern auroral zone leads to it meging into the southern region of the SAA. During this period an indentation in the southern part of SAA is present, which is a possible consequence of high solar activity, rather than a decrease trend. As previously mentioned, there was no data acquired from within the SAA in the year of 2022 as well as the second half of 2020, which marks the start of the performed analysis.

Nevertheless, none of the acquired data suggest an increase in size. Looking at the development of the location of the SAA it was found that the anomaly moved in a southeasterly direction over the time period of 4.5 years. This finding directly contradicts [Anderson et al., 2018], [Yue et al., 2024] and [Casadio and Arino, 2011], which all agree on a drift to the northwest by 0.277°W and 0.064°N per year as found in [Anderson et al., 2018]. The discrepancy with the finding in this thesis can be explained in multiple ways. Firstly, the aforementioned studies were conducted over multiple decades instead of only 4.5 years, making this finding, a steady southeast drift, to potentially be a short-term phenomenon. Secondly, the mentioned studies measure the change in location by evaluating the positions of either the centre of the SAA ([Anderson et al., 2018]), the local minima ([Yue et al., 2024]) or the location of the highest intensity of the solar particle flux ([Casadio and Arino, 2011]).

As this thesis determined the change in location based on the changes of the northernmost, easternmost, southernmost and easternmost points of the outer contour it is possible that individual points on the inside move towards the northwest while the outermost contour moves toward the southeast.

To investigate whether a point from inside the SAA would behave differntly from the outercontours, a representative midpoint from the northernmost, easternmost, southernmost and westernmost point was calculated for every year and it's change in location invesstigated. As no data within the SAA was taken during the years 2020 and 2022, they were excluded from the investigation. This was done because the outer countour for these years are a sole product of interpolation. It was found that the movement of these representative midpoints follows a zigzag pattern and therefor proves inconclusive to the investigation. For a more conclusive result a computation of the barycenter, the point of the maximum or minimum field intensity would be necessary. These computations could not be carried out within the timeframe of this work.

Having observed a decrease in size as mentioned above is conclusive with the finding of a southeast motion of the northern- and westernmost points, while the southern- and easternmost points move toward the northwest, leading to an inevitable decrease in size. Therefore, the possibility persists that both findings are correlated.

5.2. Characterisation of the Auroral Zones

5.2.1. Antarctic Auroral Zone

The 4.5 year analysis of the antarctic auroral zone revealed a stark decrease in size between July 2020 and December 2023. This finding directly contradicts [Zossi et al., 2020] stating that the southern auroral oval is steadily increasing in size. As the size of the auroral zones is measured using the occurrences of cosmic rays, it is to be expected to increase with increasing solar activity, due to particles being able to penetrate lower latitudes and therefore causing the auroral oval to expand. Data from the year 2024 were not taken into account when size comparisons were made due to an unexpected lack of detected cosmic rays between the latitudes of 90° S and 50° S. Furthermore, it was discovered that the location of the southern aurora zone changes over the observed period. Specifically, the auroral zone moves northward towards the equator.

The lack of detected cosmic rays in the aforementioned latitudes is explained by the increase in solar activity, as the solar cycle approached its maximum in 2024, leading to the auroral ovals moving equatorward ([Kataoka, Ryuho and Nakano, Shin'ya, 2021]), which was observed in the 4.5 year data as previously mentioned. As with an increase in solar activity and subsequent increase in solar cosmic rays, an increase in size is probable, as in this case only the cosmic rays associated with the auroral zone in the aforementioned region between latitudes 90° S and 50° S were detected.

This assumption especially holds merit when inspecting the previously disregarded data from 2024, where it is apparent that the southern auroral zone has significantly moved equatorward. The reason for not investigating lower latitudes was the effort to separate data originating from the southern auroral zone from data originating from the SAA, since its southern offshoots dip into the region around 50° S, adding difficulty distinguishing the two regions.

5.2.2. Arctic Auroral Zone

The investigated arctic auroral zone displays the same behaviours as the antarctic auroral zone. Similarly, data from 2024 were disregarded due to a lack of detected cosmic rays. Specifically, the measured area significantly decreased in size and is subject to an even greater decrease than its south pole counterpart. This finding, contrary to the antarctic auroral zone, agrees with [Zossi et al., 2020]. Although, as previously mentioned an increase in solar activity with a similar increase in solar cosmic rays should lead to an increase in size of the auroral zones. However, similarly to its southern hemispheric counterpart, the arctic auroral zone was found to move south towards the equator. This means that the arctic auroral zone moves out of the observed latitudes between 90° N and 50° N, leading to a decrease in area.

As mentioned above, the equatorward movement of the auroral zones is a result of the increasing solar activity and, therefore, higher occurrences of geomagnetic storms and solar flares. Furthermore, when looking at the different percentages used to find the contours mapping the area, two of those (0.03% and 0.04%) must be approached with caution. Using those very low percentages can mean that no cosmic ray might have been detected, but noise instead. Numerically, the lowest used percentage of 0.03% corresponds to 20 pixels above the used cosmic ray threshold. As single-pixel hits are disregarded, this would lead to a maximum of 10 2-pixel cosmic rays. Since it is possible to have as many higher noise pixels, this percentage leads to inconclusive results, which were therefore only computed when higher percentages of cosmic rays were not available, which was especially true for the data in late 2023 and 2024 as mentioned above.

5.3. Other Cosmic Ray Properties

5.3.1. Flux of Cosmic Rays

The fluxes of individual cosmic rays were calculated for a small sample of the dataset, consisting of 42 science visits over the span of 4.5 years of data observations. It was found that within those 42 science visits, 18449 individual cosmic rays were detected, and a histogram of the fluxes plotted (see Figure 4.15). The histogram reveals a strong decrease in detected electrons between 0.00 and 200 000 ,e^- s^{-1} pixel^{-1}, where most fluxes appear to be distributed between. Some higher flux outliers are present, but since this property was measured before straylight images were flagged, there is the possibility that those outliers are images contaminated by straylight.

About 4% of the entire data examined are considered contaminated by stray light, giving merit to this theory. Within the timeframe of this work it was not possible to exclude any supposed cosmic rays with unusually large pixel numbers.

5.3.2. Cosmic Rays and the Solar Cycle

Investigating the relation between the 11-year solar cycle and the amount of detected cosmic rays over the 4.5 years of data acquisition revealed what was physically expected: an increase in solar activity leads to an increase in cosmic ray density. The density of the cosmic rays was found to correlate with the planetary K- and a-indices, which indicate fluctuations in geomagnetic activity relating to solar activity. It was especially apparent that an increase in cosmic ray density could be observed right after a known geomagnetic storm, which agrees with [Ye et al., 2022]. In addition, a general trend in cosmic ray density can be correlated to the aforementioned Kp- and ap-indices, as corroborated by [Uga et al., 2023].

5.4. Challenges

During the development process of both the detection pipeline and the subsequent data analysis, several challenges arose along the way. While most of them have been resolved, some of them have been put on hold and will require more work in the future. The main challenges, that are still unresolved involve various chosen thresholds (see Sections 3.1.4, 3.1.3 and 3.1.5). The different thresholds involve the threshold to determine when a pixel is considered a cosmic ray, the threshold to determine when a contaminant star is masked, and the threshold defining when an image is flagged as stray light. All of those thresholds have to be determined in different ways for each science visit to ensure the highest quality data.

In the current state, all of these thresholds have largely been determined by trial and error. An attempt was made to find the threshold responsible for determining when a pixel is masked due to belonging to the central or a contaminant star by fitting a histogram of the data. Since this distribution varies drastically case by case, all major statistical fits did not cover the majority of the data. A custom fit would have to be produced for every science visit, which was determined to be out of scope for this thesis, but will be pursued further in the future.

For the purpose of a working pipeline, a threshold based on the stacking order of the images. As mentioned above, the other two thresholds were determined by visual analysis of the data to determine a threshold that fits most science cases by hand. Different thresholds were manually tested and evaluated based on visual examination of either how many cosmic rays were detected and not detected or if an image was correctly or incorrectly flagged as stray light. In the future a method has to be found to determine these thresholds automatically case by case.

Another challenge that arose was the flagging of straylight images. The first attempt was to take the median image, excluding all images above a certain threshold. However, this approach cannot distinguish between an image contaminated by stray light and an image with a large number of cosmic rays. As described in Chapter 3.1.5 the images currently flagged as straylight are determined by computing the mean of the pixels in the image with only the stars masked and subtracting the mean of the pixels in the image with the stars and cosmic rays masked.

The last major challenge was the computation of the area of the contours drawn (see Chapter 3.2.5). Although the area computation itself did not present much of a challenge, the use of different map projections resulted in distorted areas around the poles. This was especially true when the area was computed in square kilometres. This area distortion was the result of the binning and interpolating function not accounting for the geographical distortion around the poles as well as the presence of multiple, in some cases, nested contours. The first issue was solved by transforming the geographical coordinates into cartesian coordinates before binning and interpolating. This operation successfully omits the distortion around the poles, while similarly not changing the result for the rest of the globe.

The second issue that had to be dealt with was multiple, in some cases nesting, contours appearing for the same percentage. To accurately measure the total area, the area of those contours has to be either added or subtracted from the total. Several different approaches have been tested to handle the multiple contours. Those contours can be categorised as either a landmass (the largest area), an island (a smaller area outside the landmass), a lake (an area inside the landmass or island), and an island inside a lake. One approach was using Green's Theorem ([Green, 2008]), to identify the contours as different paths in different directions, and calculating the area by integrating.

This approach was pushed to its limits when the aforementioned concept of islands and lakes was introduced. The concept used in the final pipeline (see Chapter 3.2.5) defines a threshold, and any contour below this threshold is subtracted, all others are added. This causes problems in cases where lakes are larger than the threshold or islands smaller than the threshold. At this stage, it is assumed that there are no islands smaller than the threshold, and if so, the area gain would be insignificant. Islands within lakes are not dealt with at this stage. Improving this area calculation is subject to further development.

6. Conclusion and Outlook

6.1. Conclusion

This thesis aimed to characterise the South Atlantic Anomaly using cosmic ray data from the CHEOPS satellite. The main research questions this thesis was intended to answer are the following:

1. Are the sizes of the SAA and the auroral zones changing over time? If so, how?
2. Are the locations of the SAA and the auroral zones changing over time? If so, how?
3. Is there a correlation between the solar cycle and the occurrence of cosmic rays?
4. How are the fluxes of the cosmic rays distributed?

Although the satellite was not designed for detecting cosmic rays, it was possible to develop a data processing pipeline to detect cosmic rays in CHEOPS' raw data over the course of 4.5 years of data acquisition. The raw images are first corrected for bias and bad pixels before transforming the square images into circular images. Subsequently, the circular images are corrected for background fluctuations and derotated afterwards. The last step before any cosmic rays are detected consists of designing and applying a mask for the central and possible contaminant stars.

After the cosmic rays have been detected, images contaminated by stray light are flagged and different properties, such as the density of cosmic rays, the photoelectric flux of the individual cosmic rays and the percentage of pixels affected by cosmic rays are calculated to characterise the regions mentioned in the research questions. To investigate the change in area as well as location, the percentage of pixels affected by cosmic rays was calculated and mapped relative to the satellite's position after undergoing several binning and interpolating steps.

The contours of different percentages representing different outlines of the investigated regions were drawn and the area as well as the northernmost, easternmost, southernmost and westernmost points were calculated. It was found that over the investigated time frame of 4.5 years, the SAA as well as the auroral zones decrease in size. Besides the arctic auroral zone, these findings contradict previous long-term studies of the subject spanning multiple centuries. This might be the result of the increasing solar activity over the years.

All three regions experience changes on location, where both auroral zones drift towards the equator, which is to be expected during periods of heightened solar activity. The contours of the SAA were found to continuously drift to the southeast, contradicting previous long-term studies, suggesting the SAA drifting to the northwest. This unexpected finding might be explained by the choice of how the location change was investigated.

Previous studies examined the change in location from within the SAA, whereas in the case of this thesis the outer contour was investigated; therefore, both observations might be true. A correlation between the solar activity and the mean density of cosmic rays was found, indicating an increase in the mean density of cosmic rays after phases of higher geomagnetic activity and also generally over the years of increasing solar activity. These results are in accordance with the hypothesis.

This research has shown that it is possible to accurately characterise basic properties of the SAA and the auroral zones by investigating cosmic rays, a data byproduct from a satellite not developed for measuring cosmic rays. The findings show clear changes in area and location, as well as correlations between solar activity and the density of cosmic rays. Moreover, it was possible to find changes and trends in the investigated characteristics over a relatively short time span. Therefore, this thesis proves the possibility of gaining scientifically interesting data from often overlooked data byproducts.

6.2. Outlook

To conclude, an outlook on future improvements to the pipeline and analysis to increase the quality of data and results even further. Some of these improvements have already been discussed in Chapter 5, but will be mentioned again for completion.

- In the future, only data from within the SAA could be taken into account in order to improve consistency among the data. This would exclude the possibility of the outermost contour falling into the interpolation zone and therefore distorting the final data.
- Inside the bad pixel correction function, currently, bad pixels with a value <0 are replaced by noise. To further improve data quality, the noise could be replaced by the average value of the neighbouring pixels.
- As mentioned in Chapter 5.4, the thresholds for the stellar masks, the cosmic ray detection as well as the stray light flagging are currently determined by trial and error as well as through visual examinations and are subsequently used for all images. In the future, methods have to be developed and refined to automatically determine these thresholds in a case-by-case scenario. As work has already been done on the masking threshold, this can be carried out further. Possible methods for the other two thresholds have to be developed.
- The computation of the areas of the contours is currently inhibited where the contours have other contours nested inside them. Currently, this is dealt with the method described in Chapter 3.2.5, which is prone to errors. In the future, an algorithm to distinguish between the outer and nested contours could be developed, in order to increase accuracy within the area computation.
- When investigating the change in location of the SAA, the outermost contour is currently used. For a more comprehensive analysis, a point inside the SAA will have to be investigated. A possibility could be, to compute the location of the barycentre and investigate changes in its location.
- Lastly, when investigating the distribution of cosmic ray fluxes, it would provide a more comprehensive look to change the computed unit from e^- s^{-1} pixel^{-1} to e^- s^{-1} cm^{-2}. Furthermore, as discussed in Chapter 5.3.1, currently these data points are not corrected for possible stray light images. The idea is to exclude uncommonly large cosmic rays from the data set, which will require modifying the measuring process in the future.

Bibliography

[Akasofu, 2015] Akasofu, S.-I. (2015). Paradigm transitions in solar–terrestrial physics from 1900: my personal view. *History of Geo- and Space Sciences*, 6:23–43.

[Amit et al., 2021] Amit, H., Terra-Nova, F., Lézin, M., and Trindade, R. I. (2021). Non-monotonic growth and motion of the South Atlantic Anomaly. *Earth Planets and Space*, 73(1).

[Anderson et al., 2018] Anderson, P., Rich, F., and Borisov, S. (2018). Mapping the south atlantic anomaly continuously over 27 years. *Journal of Atmospheric and Solar-Terrestrial Physics*, 177:237–246. Dynamics of the Sun-Earth System: Recent Observations and Predictions.

[Asquier et al., 2015] Asquier, J., Corral Van Damme, C., Isaak, K., Rando, N., Safa, F., and Southworth, R. (2015). CHEOPS – First ESA small Scientific Mission.

[Badhwar et al., 1999] Badhwar, G., Kushin, V., Akatov, Y. A., and Myltseva, V. (1999). Effects of trapped proton flux anisotropy on dose rates in low earth orbit. *Radiation Measurements*, 30(3):415–426.

[Bartels et al., 1939] Bartels, J., Heck, N. H., and Johnston, H. F. (1939). The three-hour-range index measuring geomagnetic activity. *Terrestrial Magnetism and Atmospheric Electricity*, 44(4):411–454.

[Beck et al., 2017] Beck, T., Plesseria, J.-Y., Pagano, I., Wildi, F., Gambicorti, L., Broeg, C., Cessa, V., Fortier, A., Piazza, D., Ehrenreich, D., Magrin, D., Peter, G., Steller, M., Kovacs, Z., Ragazzoni, R., and Benz, W. (2017). The cheops (characterising exoplanet satellite) mission: telescope optical design, development status and main technical and programmatic challenges. page 245.

[Becker Tjus and Merten, 2020] Becker Tjus, J. and Merten, L. (2020). Closing in on the origin of galactic cosmic rays using multimessenger information. *Physics Reports*, 872:1–98. Closing in on the origin of Galactic cosmic rays using multimessenger information.

[Bekkelien, 2023] Bekkelien, A. (2023). CHEOPS Data Products Definition Document. Technical report, University of Geneva.

[Benz et al., 2020] Benz, W., Broeg, C., Fortier, A., Rando, N., Beck, T., Beck, M., Queloz, D., Ehrenreich, D., Maxted, P. F. L., Isaak, K. G., Billot, N., Alibert, Y., Alonso, R., António, C., Asquier, J., Bandy, T., Bárczy, T., Barrado, D., Barros, S.

C. C., Baumjohann, W., Bekkelien, A., Bergomi, M., Biondi, F., Bonfils, X., Borsato, L., Brandeker, A., Busch, M.-D., Cabrera, J., Cessa, V., Charnoz, S., Chazelas, B., Collier Cameron, A., Corral Van Damme, C., Cortes, D., Davies, M. B., Deleuil, M., Deline, A., Delrez, L., Demangeon, O., Demory, B. O., Erikson, A., Farinato, J., Fossati, L., Fridlund, M., Futyan, D., Gandolfi, D., Garcia Munoz, A., Gillon, M., Guterman, P., Gutierrez, A., Hasiba, J., Heng, K., Hernandez, E., Hoyer, S., Kiss, L. L., Kovacs, Z., Kuntzer, T., Laskar, J., Lecavelier des Etangs, A., Lendl, M., López, A., Lora, I., Lovis, C., Lüftinger, T., Magrin, D., Malvasio, L., Marafatto, L., Michaelis, H., de Miguel, D., Modrego, D., Munari, M., Nascimbeni, V., Olofsson, G., Ottacher, H., Ottensamer, R., Pagano, I., Palacios, R., Pallé, E., Peter, G., Piazza, D., Piotto, G., Pizarro, A., Pollaco, D., Ragazzoni, R., Ratti, F., Rauer, H., Ribas, I., Rieder, M., Rohlfs, R., Safa, F., Salatti, M., Santos, N. C., Scandariato, G., Ségransan, D., Simon, A. E., Smith, A. M. S., Sordet, M., Sousa, S. G., Steller, M., Szabó, G. M., Szoke, J., Thomas, N., Tschentscher, M., Udry, S., Van Grootel, V., Viotto, V., Walter, I., Walton, N. A., Wildi, F., and Wolter, D. (2020). The cheops mission. *Experimental Astronomy*, 51(1):109–151.

[Binder et al., 1975] Binder, D., Smith, E. C., and Holman, A. B. (1975). Satellite anomalies from galactic cosmic rays. *IEEE Transactions on Nuclear Science*, 22(6):2675–2680.

[Bonomi et al., 2020] Bonomi, G., Checchia, P., D'Errico, M., Pagano, D., and Saracino, G. (2020). Applications of cosmic-ray muons. *Progress in Particle and Nuclear Physics*, 112:103768.

[Bradski, 2000] Bradski, G. (2000). The OpenCV Library. *Dr. Dobb's Journal of Software Tools*.

[Casadio and Arino, 2011] Casadio, S. and Arino, O. (2011). Monitoring the south atlantic anomaly using atsr instrument series. *Advances in Space Research*, 48(6):1056–1066.

[Cessa et al., 2017] Cessa, V., Beck, T., Benz, W., Broeg, C., Ehrenreich, D., Fortier, A., Peter, G., Magrin, D., Pagano, I., Plesseria, J.-Y., Steller, M., Szoke, J., Thomas, N., Ragazzoni, R., and Wildi, F. (2017). CHEOPS: a space telescope for ultra-high precision photometry of exoplanet transits. In Sodnik, Z., Cugny, B., and Karafolas, N., editors, *International Conference on Space Optics — ICSO 2014*, volume 10563, page 105631L. International Society for Optics and Photonics, SPIE.

[Clúa de Gonzalez et al., 1993] Clúa de Gonzalez, A. L., Gonzalez, W. D., Dutra, S. L. G., and Tsurutani, B. T. (1993). Periodic variation in the geomagnetic activity: A study based on the ap index. *Journal of Geophysical Research: Space Physics*, 98(A6):9215–9231.

[Dawson, 2007] Dawson, B. R. (2007). Hybrid performance of the pierre auger observatory.

[Feldstein, 1964] Feldstein, Y. I. (1964). Auroral morphology, I. The location of the auroral zone. *Tellus A Dynamic Meteorology and Oceanography*, 16(2):252–257.

[Finlay et al., 2020] Finlay, C., Kloss, C., Olsen, N., Hammer, M., Tøffner-Clausen, L., Grayver, A., and Kuvshinov, A. (2020). The chaos-7 geomagnetic field model and observed changes in the south atlantic anomaly. *Earth, Planets and Space*, 72.

[Fortier, A. et al., 2024] Fortier, A., Simon, A. E., Broeg, C., Olofsson, G., Deline, A., Wilson, T. G., Maxted, P. F. L., Brandeker, A., Collier Cameron, A., Beck, M., Bekkelien, A., Billot, N., Bonfanti, A., Bruno, G., Cabrera, J., Delrez, L., Demory, B.-O., Futyan, D., Florén, H.-G., Günther, M. N., Heitzmann, A., Hoyer, S., Isaak, K. G., Sousa, S. G., Stalport, M., Turin, A., Verhoeve, P., Akinsanmi, B., Alibert, Y., Alonso, R., Bánhidi, D., Bárczy, T., Barrado, D., Barros, S. C. C., Baumjohann, W., Baycroft, T., Beck, T., Benz, W., Bíró, B. I., Bódi, A., Bonfils, X., Borsato, L., Charnoz, S., Cseh, B., Csizmadia, Sz., Csányi, I., Cubillos, P. E., Davies, M. B., Davis, Y. T., Deleuil, M., Demangeon, O. D. S., Derekas, A., Dransfield, G., Ducrot, E., Ehrenreich, D., Erikson, A., Fariña, C., Fossati, L., Fridlund, M., Gandolfi, D., Garai, Z., Garcia, L., Gillon, M., Gómez Maqueo Chew, Y., Gómez-Muñoz, M. A., Granata, V., Güdel, M., Guterman, P., Hegedüs, T., Helling, Ch., Jehin, E., Kalup, Cs., Kilkenny, D., Kiss, L. L., Kriskovics, L., Lam, K. W. F., Laskar, J., Lecavelier des Etangs, A., Lendl, M., Lopez Pina, A., Luntzer, A., Magrin, D., Miller, N. J., Modrego Contreras, D., Mordasini, C., Munari, M., Murray, C. A., Nascimbeni, V., Ottacher, H., Ottensamer, R., Pagano, I., Pál, A., Pallé, E., Pasetti, A., Pedersen, P. P., Peter, G., Petrucci, R., Piotto, G., Pizarro-Rubio, A., Pollacco, D., Pribulla, T., Queloz, D., Ragazzoni, R., Rando, N., Rauer, H., Ribas, I., Sabin, L., Santos, N. C., Scandariato, G., Schanche, N., Schroffenegger, U., Scutt, O. J., Sebastian, D., Ségransan, D., Seli, B., Smith, A. M. S., Southworth, R., Standing, M. R., Szabó, Gy. M., Szakáts, R., Thomas, N., Timmermans, M., Triaud, A. H. M. J., Udry, S., Van Grootel, V., Venturini, J., Villaver, E., Vinkó, J., Walton, N. A., Wells, R., and Wolter, D. (2024). Cheops in-flight performance - a comprehensive look at the first 3.5 yr of operations. *A&A*, 687:A302.

[Freiherr von Forstner, Johan L. et al., 2021] Freiherr von Forstner, Johan L., Dumbović, Mateja, Möstl, Christian, Guo, Jingnan, Papaioannou, Athanasios, Elftmann, Robert, Xu, Zigong, Christoph Terasa, Jan, Kollhoff, Alexander, Wimmer-Schweingruber, Robert F., Rodríguez-Pacheco, Javier, Weiss, Andreas J., Hinterreiter, Jürgen, Amerstorfer, Tanja, Bauer, Maike, Belov, Anatoly V., Abunina, Maria A., Horbury, Timothy, Davies, Emma E., O'Brien, Helen, Allen, Robert C., Bruce Andrews, G., Berger, Lars, Boden, Sebastian, Cernuda Cangas, Ignacio, Eldrum, Sandra, Espinosa Lara, Francisco, Gómez Herrero, Raúl, Hayes, John R., Ho, George C., Kulkarni, Shrinivasrao R., Jeffrey Lees, W., Martín, César, Mason, Glenn M., Pacheco, Daniel, Prieto Mateo, Manuel, Ravanbakhsh, Ali, Rodríguez Polo, Oscar, Sánchez Prieto, Sebastián, Schlemm, Charles E., Seifert, Helmut, Tyagi, Kush, and Yedla, Mahesh (2021). Radial evolution of the april 2020 stealth coronal mass ejection between 0.8 and 1 au - comparison of forbush decreases at solar orbiter and near the earth. *A&A*, 656:A1.

[Fürst et al., 2009] Fürst, F., Wilms, J., Rothschild, R. E., Pottschmidt, K., Smith, D. M., and Lingenfelter, R. (2009). Temporal variations of strength and location of the south atlantic anomaly as measured by rxte. *Earth and Planetary Science Letters*, 281(3–4):125–133.

[Garzon et al., 2017] Garzon, J., Collazo, J., Cuenca-García, J., Castro, D., Otero, J., Yermo, M., Blanco, J., Kurtukian-Nieto, T., Morozova, A., Pais, M. A., Blanco, A., Fonte, P., Lopes, L., Kornakov, G., Álvarez Pol, H., Cabanelas, P., Pazos, A., Seco, M., Riádigos, I., and Taboada, J. (2017). Tragaldabas. first results on cosmic ray studies and their relation with the solar activity, the earth magnetic field and the atmospheric properties.

[Gillies et al., 07] Gillies, S. et al. (2007–). Shapely: manipulation and analysis of geometric objects.

[Green, 2008] Green, G. (2008). An essay on the application of mathematical analysis to the theories of electricity and magnetism.

[Hanslmeier, 2020] Hanslmeier, A. (2020). *Einführung in Astronomie und Astrophysik*. Springer Berlin Heidelberg Imprint: Springer Spektrum, Berlin Heidelberg, 4th ed. 2020 edition.

[Heitzmann and Pevestorff, 2025] Heitzmann, A. and Pevestorff, L. (2025). Cheopscosmics.

[Howell, 2006] Howell, S. B. (2006). *Handbook of CCD Astronomy*. Cambridge Observing Handbooks for Research Astronomers. Cambridge University Press.

[Hoyer, S. et al., 2020] Hoyer, S., Guterman, P., Demangeon, O., Sousa, S. G., Deleuil, M., Meunier, J. C., and Benz, W. (2020). Expected performances of the characterising exoplanet satellite (cheops) - iii. data reduction pipeline: architecture and simulated performances. *A&A*, 635:A24.

[Karney, 2023] Karney, C. F. F. (2023). Geographiclib python package. Version 2.0; `https://pypi.org/project/geographiclib/`.

[Kataoka, Ryuho and Nakano, Shin'ya, 2021] Kataoka, Ryuho and Nakano, Shin'ya (2021). Auroral zone over the last 3000 years. *J. Space Weather Space Clim.*, 11:46.

[Lowrie, 2023] Lowrie, W. (2023). *The Earth's Magnetic Field*. Oxford University Press.

[Matzka et al., 2021] Matzka, J., Bronkalla, O., Tornow, K., Elger, K., and Stolle, C. (2021). Geomagnetic Kp Index.

[McPherron,] McPherron, R. geomagnetic field.

[Merrill and McElhinny, 1983] Merrill, R. T. and McElhinny, M. W. (1983). The earth's magnetic field: Its history, origin and planetary perspective. *International Geophysics Series*, 32.

[Nasuddin et al., 2019] Nasuddin, K., Abdullah, M., and Abdul Hamid, N. S. (2019). Characterization of the south atlantic anomaly. *Nonlinear Processes in Geophysics*, 26:25–35.

[Pavón-Carrasco and De Santis, 2016] Pavón-Carrasco, F. J. and De Santis, A. (2016). The south atlantic anomaly: The key for a possible geomagnetic reversal. *Frontiers in Earth Science*, Volume 4 - 2016.

[Spatschek, 2018] Spatschek, K.-H. (2018). *Astrophysik : Eine Einführung in Theorie und Grundlagen*. Springer Berlin Heidelberg : Imprint: Springer Spektrum,, Berlin, Heidelberg :, 2nd ed. 2018. edition.

[Ting, 2013] Ting, S. (2013). The alpha magnetic spectrometer on the international space station. *Nuclear Physics B - Proceedings Supplements*, 243-244:12–24. Proceedings of the IV International Conference on Particle and Fundamental Physics in Space.

[Trivedi et al., 2005] Trivedi, N., Pathan, B., Schuch, N. J., Barreto, M., and Dutra, L. (2005). Geomagnetic phenomena in the south atlantic anomaly region in brazil. *Advances in Space Research*, 36(10):2021–2024. Solar Wind-Magnetosphere-Ionosphere Dynamics and Radiation Models.

[Uga et al., 2023] Uga, C., Giri, A., Adhikari, B., Mosisa, E., Gashu, C., and An, C. (2023). Variations of cosmic ray intensity with the solar flare index, coronal index, and geomagnetic indices: Wavelet and cross correlation approaches. *Physics of Plasmas*, 30:83901.

[University of Geneva and University of Bern, 2023] University of Geneva and University of Bern (2023). CHEOPS mission extended.

[Ye et al., 2022] Ye, Q., Wang, C., He, F., Xue, B., and Zhang, X. (2022). The frequency-domain characterization of cosmic ray intensity variations before forbush decreases associated with geomagnetic storms. *Space Weather*, 20(3):e2021SW002863. e2021SW002863 2021SW002863.

[Yue et al., 2024] Yue, Y., Gao, J., He, F., Wei, Y., Cai, S., Wang, H., Wang, Y., Rong, Z., Yao, Z., Lin, W., and Pan, Y. (2024). Evolution and disappearance of the paleo-west pacific anomaly: Implications to the future of south atlantic anomaly. *Physics of the Earth and Planetary Interiors*, 353:107214.

[Zossi et al., 2020] Zossi, B., Fagre, M., Amit, H., and Elias, A. G. (2020). Geomagnetic field model indicates shrinking northern auroral oval. *Journal of Geophysical Research: Space Physics*, 125(8):e2019JA027434. e2019JA027434 2019JA027434.

Acronyms

ADU	Analog-to-Digital Unit. 22, 32, 34, 37
AIMO	Advanced Inverted Mode Operation. 6
AMS-02	Alpha Magnetic Spectrometer. 13
BCA	Baffle and Cover Assembly. x, 6, 8
BEE	Back End Electronics. 6, 9
BEO	Back End Optics. 6
CCD	Charged Coupled Device. x, 3, 5–10, 17, 21–23, 37
CHEOPS	CHaracterizing ExOPlanet Satellite. i, ii, iv, x, 1–10, 17, 19, 20, 22, 23, 25, 27, 29, 37, 43, 45, 51, 65, 71
CoRoT	COnvection, ROtation and planetary Transits. 8
DRP	Data Reduction Pipeline. 6
ESA	European Space Agency. i, ii, 3, 4
FPM	Focal Plane Module. 7, 9
HZE	Highly Ionizing Raidation. 11
IFSW	In-Flight Software. 9
ISS	International Space Station. 13
LEO	Low Earth Orbit. ii, 4, 6, 17
LOS	Line Of Sight. 5, 34
NaN	Not a Number. 38, 44
NASA	National Aeronautics and Space Administration. 1
OTA	Optical Telescope Assembly. x, 6, 8
PSF	Point Spread Function. x, 5, 6, 10, 29
RMS	Root Mean Square. 5

RTS	Random Telegraphic Signal. 23–25
SAA	South Atlantic Anomaly. i, ii, iv, v, vii, x, xi, 1, 2, 15–17, 19, 27, 29, 30, 38, 40, 43–52, 54–56, 59, 65–68, 71–73, 81, 82, 84–86
SEM	Sensor Electronics Module. 6, 9
SEU	Single-Event Upset. 17
TTV	Transit-Time Variation. 10

A. Appendix

A.1. South Atlantic Anomaly

A.1.1. RAW Data Tables

Table A.1.: Size of the SAA in square degrees according to different pixel percentages in 6 months intervals. "-" indicates that no area was calculated for the given percentage.

Timeframe	0.1%	1%	2%	5%	10%
01-07-2020 to 31-12-2020	5173.56	2729.17	474.08	168.26	124.10
01-01-2021 to 30-06-2021	5225.79	2623.73	50.26	-	-
01-07-2021 to 31-12-2021	5136.46	2858.77	1782.72	720.67	173.64
01-01-2022 to 30-06-2022	5002.89	240.77	-	-	-
01-07-2022 to 31-12-2022	4809.41	565.75	-	-	-
01-01-2023 to 30-06-2023	4637.06	3515.85	2982.36	2236.47	1616.00
01-07-2023 to 31-12-2023	4504.53	3382.70	2989.14	2300.55	1542.54
01-01-2024 to 30-06-2024	4573.64	3141.34	2653.89	1957.42	1401.98
01-07-2024 to 31-12-2024	3981.57	3012.97	2550.52	1928.94	1358.09

Table A.2.: Size of the SAA in square kilometres according to different pixel percentages in 6 months intervals. "-" indicates that no area was calculated for the given percentage.

Timeframe	0.1%	1%	2%	5%	10%
01-07-2020 to 31-12-2020	70 845 051.77	38 828 320.87	6 657 121.76	2 278 200.31	1 679 244.72
01-01-2021 to 30-06-2021	71 392 849.81	37 362 541.38	761 816.52	-	-
01-07-2021 to 31-12-2021	70 252 398.78	39 849 607.95	24 902 812.37	10 143 233.07	2 448 995.56
01-01-2022 to 30-06-2022	68 126 614.52	3 479 152.20	-	-	-
01-07-2022 to 31-12-2022	65 688 178.52	7 998 180.05	-	-	-
01-01-2023 to 30-06-2023	63 591 414.51	48 112 702.40	40 933 123.79	30 833 146.81	22 333 437.58
01-07-2023 to 31-12-2023	61 382 026.89	46 473 217.16	41 159 172.84	31 796 049.55	21 323 419.24
01-01-2024 to 30-06-2024	61 895 989.27	43 071 246.19	36 452 929.89	26 902 775.96	19 283 841.89
01-07-2024 to 31-12-2024	55 976 151.70	41 400 853.97	35 083 541.24	26 555 620.71	18 702 704.75

Table A.3.: Size of the SAA in square degrees according to different pixel percentages in 12 months intervals. "-" indicates that no area was calculated for the given percentage.

Timeframe	0.1%	1%	2%	5%	10%
01-07-2020 to 31-12-2020	5173.56	2729.17	474.08	168.26	124.10
01-01-2021 to 31-12-2021	5148.93	3318.06	1977.87	762.30	178.70
01-01-2022 to 31-12-2022	4946.25	359.17	-	-	-
01-01-2023 to 31-12-2023	4643.48	3432.74	2954.41	2225.26	1588.91
01-01-2024 to 31-12-2024	4372.60	3090.49	2615.95	1959.19	1383.81

Table A.4.: Size of the SAA in square kilometres according to different pixel percentages in 12 months intervals. "-" indicates that no area was calculated for the given percentage.

Timeframe	0.1%	1%	2%	5%	10%
01-07-2020 to 31-12-2020	70 845 051.77	38 828 320.87	6 657 121.76	2 278 200.31	1 679 244.72
01-01-2021 to 31-12-2021	70 387 423.07	46 213 237.66	27 710 236.18	10 739 579.89	2 520 695.73
01-01-2022 to 31-12-2022	67 356 598.30	5 108 299.80	-	-	-
01-01-2023 to 31-12-2023	63 306 989.48	47 096 532.82	40 622 143.76	30 710 649.40	21 976 984.70
01-01-2024 to 31-12-2024	59 837 650.79	42 398 753.81	35 931 527.14	26 932 802.45	19 028 297.80

Table A.5.: Size of the SAA in square degrees according to different pixel percentages during 4.5 years of observation.

Timeframe	0.1%	1%	2%	5%	10%
01-07-2020 to 31-12-2024	4597.64	3150.29	2685.19	2010.10	1426.51

Table A.6.: Size of the SAA in square kilometres according to different pixel percentages during 4.5 years of observation.

Timeframe	0.1%	1%	2%	5%	10%
01-07-2020 to 31-12-2024	62 571 788.28	43 207 817.79	36 892 025.54	27 656 221.25	19 636 329.11

Table A.7.: Locations of the midpoints computed from Table A.8.

Timeframe	Latitude	Longitude
01-07-2020 to 31-12-2020	-23.23	-20.03
01-01-2021 to 30-06-2021	-22.11	-36.26
01-07-2021 to 31-12-2021	-22.27	-36.65
01-01-2022 to 30-06-2022	-22.57	-36.08
01-07-2022 to 31-12-2022	-24.52	-24.88
01-01-2023 to 30-06-2023	-25.34	-26.12
01-07-2023 to 31-12-2023	-22.29	-34.26
01-01-2024 to 30-06-2024	-24.66	-34.64
01-07-2024 to 31-12-2024	-26.68	-29.51

Table A.8.: Coordinates of the northernmost, southernmost, eastermost and westernmost points of the SAA in 6-month intervals for the respective pixel percentage contours. "-" indicates that no coordinates were calculated for the given percentage.

	0.1%				1%				2%				5%				10%			
Timeframe	N	E	S	W	N	E	S	W	N	E	S	W	N	E	S	W	N	E	S	W
01-07-2020 to 31-12-2020	7.57	63.83	-54.02	-103.89	2.13	29.48	-37.89	-94.08	-10.15	28.98	-33.51	-28.47	-21.90	28.31	-32.91	9.19	-22.43	27.54	-32.44	12.00
01-01-2021 to 30-06-2021	7.64	30.54	-51.86	-103.05	2.57	23.28	-36.12	-86.16	-1.77	-7.05	-19.56	-64.56	-	-	-	-	-	-	-	-
01-07-2021 to 31-12-2021	7.44	29.87	-51.97	-103.17	2.31	23.82	-45.46	-94.68	-3.88	-30.56	-41.22	-92.39	-8.98	-52.06	-34.61	-87.94	-15.43	-66.38	-28.85	-83.05
	7.08	28.98	-52.21	-101.13	-2.30	-25.93	-25.49	-68.22	-	-	-	-	-	-	-	-	-	-	-	-
01-07-2022 to 31-12-2022	6.37	50.31	-55.40	-100.07	-10.78	18.11	-33.35	-38.36	-	-	-	-	-	-	-	-	-	-	-	-
01-01-2023 to 30-06-2023	4.94	46.02	-55.58	-98.26	1.34	22.24	-48.79	-92.03	-0.06	7.40	-47.04	-88.53	-2.88	-5.79	-44.05	-83.88	-6.14	-18.04	-41.28	-80.68
01-07-2023 to 31-12-2023	4.43	27.67	-49.02	-96.20	0.62	14.90	-47.12	-93.49	-0.91	9.90	-46.08	-92.59	-3.93	-6.10	-43.95	-91.13	-6.23	-15.37	-41.49	-89.65
01-01-2024 to 30-06-2024	3.49	28.25	-52.81	-97.53	-0.04	19.97	-46.94	-88.83	-2.22	7.68	-45.50	-86.74	-6.26	-3.61	-42.92	-83.59	-9.47	-18.20	-40.34	-80.55
01-07-2024 to 31-12-2024	3.45	38.11	-56.81	-97.13	-1.54	16.91	-46.64	-88.34	-3.12	5.75	-45.25	-86.30	-5.88	-8.26	-42.91	-82.95	-9.04	-20.94	-40.52	-79.52

Table A.9.: Coordinates of the northernmost, southernmost, eastermost and westernmost points of the SAA in 12-month intervals for the respective pixel percentage contours. "-" indicates that no coordinates were calculated for the given percentage.

	0.1%				1%				2%				5%				10%			
Timeframe	N	E	S	W	N	E	S	W	N	E	S	W	N	E	S	W	N	E	S	W
2020	7.57	63.83	-54.02	-103.89	2.13	29.48	-37.89	-94.08	-10.15	28.98	-33.51	-28.47	-21.90	28.31	-32.91	9.19	-22.43	27.54	-32.44	12.00
2021	7.35	30.33	-51.99	-102.81	1.54	23.59	-45.55	-94.67	-1.78	-24.57	-41.38	-92.38	-8.93	-50.68	-34.69	-87.94	-15.37	-66.02	-28.88	-83.04
2022	6.71	28.67	-52.03	-100.51	-12.74	-0.59	-27.58	-36.14	-	-	-	-	-	-	-	-	-	-	-	-
2023	4.75	28.31	-50.59	-98.52	1.01	18.02	-47.44	-92.00	-0.51	8.52	-46.10	-88.77	-3.35	-6.28	-43.73	-84.38	-6.20	-17.74	-41.21	-80.38
2024	3.41	29.73	-53.88	-97.25	-1.05	18.82	-46.77	-88.60	-3.25	6.99	-45.41	-86.46	-6.67	-5.25	-42.91	-82.99	-9.59	-18.25	-40.32	-79.57

Table A.10.: Coordinates of the northernmost, southernmost, easternmost and westernmost points of the SAA during 4.5 years of observation for the respective pixel percentage contours.

	0.1%				1%				2%				5%				10%			
Timeframe	N	E	S	W	N	E	S	W	N	E	S	W	N	E	S	W	N	E	S	W
01-07-2020 to 31-12-2024	4.01	28.62	-50.56	-97.89	-0.61	18.66	-46.82	-88.72	-2.44	7.23	-45.48	-86.54	-5.26	-6.63	-42.98	-83.10	-8.24	-18.36	-40.48	-79.86

A.2. South Pole

A.2.1. RAW data tables

Table A.11.: Size of the antarctic auroral zone in square degrees according to different pixel percentages in 6 months intervals. "-" indicates that no area was calculated for the given percentage.

Timeframe	0.075%	0.08%	0.09%	0.1%	0.125%
01-07-2020 to 31-12-2020	2565.95	2286.89	1606.72	1179.02	528.06
01-01-2021 to 30-06-2021	1716.74	1496.30	928.60	546.53	203.98
01-07-2021 to 31-12-2021	1166.67	853.30	196.95	35.69	-
01-01-2022 to 30-06-2022	1961.99	1722.65	1328.78	1027.67	489.76
01-07-2022 to 31-12-2022	1940.88	1708.78	1368.61	1205.55	793.12
01-01-2023 to 30-06-2023	2099.12	1987.24	1708.03	1417.49	863.83
01-07-2023 to 31-12-2023	1042.00	914.68	601.24	415.08	100.24
01-01-2024 to 30-06-2024	258.21	186.20	97.52	42.69	4.42
01-07-2024 to 31-12-2024	1445.06	1393.30	1228.06	1075.64	755.72

Table A.12.: Size of the antarctic auroral zone in square kilometres according to different pixel percentages in 6 months intervals. "-" indicates that no area was calculated for the given percentage.

Timeframe	0.075%	0.08%	0.09%	0.1%	0.125%
01-07-2020 to 31-12-2020	14 618 537.64	12 905 921.88	9 124 877.70	6 774 106.60	2 990 414.77
01-01-2021 to 30-06-2021	9 387 442.53	8 172 442.53	5 013 942.79	2 985 068.57	1 141 696.12
01-07-2021 to 31-12-2021	6 080 757.78	4 503 440.55	1 140 281.57	207 023.08	-
01-01-2022 to 30-06-2022	11 523 363.26	10 062 560.73	7 634 426.89	6 003 927.65	2 809 130.17
01-07-2022 to 31-12-2022	11 677 254.85	10 222 896.48	8 225 593.75	7 183 551.19	4 759 645.76
01-01-2023 to 30-06-2023	11 994 824.70	11 496 748.93	10 442 734.08	9 211 532.52	6 104 294.31
01-07-2023 to 31-12-2023	6 194 330.43	5 437 558.88	3 685 443.59	2 130 678.26	625 422.80
01-01-2024 to 30-06-2024	2 097 205.99	1 555 178.47	797 711.12	340 076.99	36 065.54
01-07-2024 to 31-12-2024	8 257 974.16	8 150 063.19	7 478 012.32	6 776 792.58	5 305 650.00

Table A.13.: Size of the antarctic auroral zone in square degrees according to different pixel percentages in 12 months intervals.

Timeframe	0.075%	0.08%	0.09%	0.1%	0.125%
01-07-2020 to 31-12-2020	2565.95	2286.89	1606.72	1179.02	528.06
01-01-2021 to 31-12-2021	1488.13	1225.12	557.99	302.78	14.56
01-01-2022 to 31-12-2022	1976.10	1745.52	1358.92	1135.43	654.42
01-01-2023 to 31-12-2023	1530.30	1370.01	1093.49	882.21	376.30
01-01-2024 to 31-12-2024	1089.51	950.87	678.20	485.50	55.89

Table A.14.: Size of the antarctic auroral zone in square kilometres according to different pixel percentages in 12 months intervals.

Timeframe	0.075%	0.08%	0.09%	0.1%	0.125%
01-07-2020 to 31-12-2020	14 618 537.64	12 905 921.88	9 124 877.70	6 774 106.60	2 990 414.77
01-01-2021 to 31-12-2021	8 026 155.73	6 613 186.79	3 149 037.14	1 685 033.85	85 027.25
01-01-2022 to 31-12-2022	11 795 357.04	10 404 927.52	8 020 389.92	6 694 063.92	3 928 936.15
01-01-2023 to 31-12-2023	9 835 535.33	8 751 025.26	6 974 527.92	5 630 824.60	2 528 562.88
01-01-2024 to 31-12-2024	6 864 732.91	6 168 620.78	4 754 980.66	3 485 065.88	478 605.89

Table A.15.: Size of the antarctic auroral zone in square degrees according to different pixel percentages during 4.5 years of observation.

Timeframe	0.075%	0.08%	0.09%	0.1%	0.125%
01-07-2020 to 31-12-2024	1287.71	1113.81	744.55	506.13	63.68

Table A.16.: Size of the antarctic auroral zone in square kilometres according to different pixel percentages during 4.5 years of observation.

Timeframe	0.075%	0.08%	0.09%	0.1%	0.125%
01-07-2020 to 31-12-2024	7 713 108.33	6 679 216.71	4 592 021.90	3 107 358.09	389 104.23

Table A.17.: Coordinates of the northernmost, southernmost, easternmost and westernmost points of the antarctic auroral zone (latitudes between $-90°$ and $-50°$ S) in 6-month intervals for the respective pixel percentage contours. "-" indicates that no coordinates were calculated for the given percentage.

	0.075%				0.08%				0.09%				0.1%				0.125%			
Timeframe	N	E	S	W	N	E	S	W	N	E	S	W	N	E	S	W	N	E	S	W
01-07-2020 to 31-12-2020	-50.00	161.25	-80.31	-175.37	-50.00	158.20	-79.89	-174.07	-50.00	73.25	-79.14	-156.15	-51.07	63.79	-78.47	-144.55	-55.57	52.07	-75.60	-85.30
01-01-2021 to 30-06-2021	-50.00	157.98	-79.00	-136.53	-52.64	57.16	-78.62	-135.47	-55.71	53.44	-77.79	-133.43	-56.49	44.29	-76.50	-119.52	-61.16	28.43	-74.87	-50.69
01-07-2021 to 31-12-2021	-50.00	75.58	-79.17	-178.54	-51.79	73.21	-78.65	-149.69	-60.74	30.70	-77.29	-112.86	-65.63	5.18	-72.22	-23.77	-	-	-	-
01-01-2022 to 30-06-2022	-50.00	72.02	-78.65	-175.04	-50.00	65.31	-78.33	-173.79	-54.10	51.34	-77.59	-129.79	-54.80	48.58	-76.45	-118.10	-56.40	41.49	-74.93	-83.61
01-07-2022 to 31-12-2022	-50.00	62.67	-77.61	-149.89	-50.00	59.74	-77.36	-148.77	-50.44	53.62	-76.88	-145.11	-51.88	50.20	-76.45	-123.68	-55.42	43.10	-75.44	-94.42
01-01-2023 to 30-06-2023	-50.00	69.07	-76.25	-132.30	-50.00	68.31	-76.01	-130.20	-50.00	52.22	-75.62	-125.95	-50.00	47.09	-75.23	-113.48	-50.00	39.73	-74.34	-78.38
01-07-2023 to 31-12-2023	-54.69	43.51	-75.49	-103.30	-55.14	41.85	-75.17	-101.51	-56.00	38.71	-74.51	-90.65	-56.88	34.92	-73.80	-63.84	-60.92	18.47	-70.24	-29.82
01-01-2024 to 30-06-2024	-50.00	39.20	-69.22	-59.01	-50.00	38.61	-68.63	-58.52	-50.00	30.18	-62.57	-57.11	-51.49	28.79	-61.18	1.75	-56.79	8.89	-58.60	5.50
01-07-2024 to 31-12-2024	-50.00	44.76	-73.67	-101.40	-50.00	43.56	-73.38	-99.88	-50.00	41.32	-72.78	-62.37	-50.00	39.09	-72.19	-58.64	-50.00	25.86	-70.75	-51.76

Table A.18.: Coordinates of the northernmost, southernmost, eastermost and westernmost points of the antarctic auroral zone (latitudes between $-90°$ and $-50°$ S) in 12-month intervals for the respective pixel percentage contours.

	0.075%				0.08%				0.09%				0.1%				0.125%			
Timeframe	N	E	S	W	N	E	S	W	N	E	S	W	N	E	S	W	N	E	S	W
2020	-50.00	161.25	-80.31	-175.37	-50.00	158.20	-79.89	-174.07	-50.00	73.25	-79.14	-156.15	-51.07	63.79	-78.47	-144.55	-55.57	52.07	-75.60	-85.30
2021	-54.71	59.40	-78.89	-150.25	-55.55	56.35	-78.34	-135.13	-56.98	43.32	-76.32	-116.41	-60.36	30.78	-74.59	-52.16	-66.27	2.81	-68.77	-4.91
2022	-50.00	65.52	-77.74	-150.41	-50.00	59.96	-77.40	-148.28	-51.68	52.57	-76.75	-124.55	-54.04	48.94	-76.19	-99.83	-55.74	42.55	-74.98	-83.47
2023	-50.00	49.14	-75.94	-131.26	-50.49	47.30	-75.69	-127.81	-52.13	44.17	-75.18	-102.25	-53.44	41.37	-74.69	-79.84	-56.35	29.39	-73.41	-54.15
2024	-50.00	41.00	-72.40	-63.19	-50.00	39.94	-71.87	-59.53	-50.00	38.22	-70.57	-54.16	-50.00	32.48	-69.43	-50.84	-51.01	12.56	-59.58	2.80

Table A.19.: Coordinates of the northernmost, southernmost, eastermost and westernmost points of the antarctic auroral zone (latitudes between $-90°$ and $-50°$ S) during 4.5 years of observation for the respective pixel percentage contours.

	0.075%				0.08%				0.09%				0.1%				0.125%			
Timeframe	N	E	S	W	N	E	S	W	N	E	S	W	N	E	S	W	N	E	S	W
01-07-2020 to 31-12-2024	-53.63	48.17	-76.15	-107.90	-54.30	45.97	-75.76	-101.24	-55.50	41.91	-75.03	-86.56	-56.84	38.19	-74.30	-64.10	-61.79	9.34	-69.00	-21.76

A.3. North Pole

A.3.1. RAW data tables

Table A.20.: Size of the arctic auroral zone (latitudes between 50° and 90° N) in square degrees according to different pixel percentages in 6 months intervals. Areas for the percentages of 0.05% to 0.07% were calculated for all timeframes, except those with insufficient data. Additionally, areas for the percentages 0.03% and 0.04% were calculated if there was no or not enough data for 0.05%. "-" indicates that no area was calculated for the given percentage.

Timeframe	0.03%	0.04%	0.05%	0.06%	0.07%
01-07-2020 to 31-12-2020	-	-	1851.73	813.38	484.75
01-01-2021 to 30-06-2021	-	-	2802.39	742.66	99.95
01-07-2021 to 31-12-2021	-	-	1117.66	385.35	203.39
01-01-2022 to 30-06-2022	-	-	1188.46	474.96	297.76
01-07-2022 to 31-12-2022	-	-	554.99	439.89	203.05
01-01-2023 to 30-06-2023	-	-	524.93	155.38	38.41
01-07-2023 to 31-12-2023	344.05	180.06	8.88	-	-
01-01-2024 to 30-06-2024	Insufficient Data				
01-07-2024 to 31-12-2024	360.87	42.18	6.40	-	-

Table A.21.: Size of the arctic auroral zone (latitudes between 50° and 90° N) in square kilometres according to different pixel percentages in 6 months intervals. Areas for the percentages of 0.05% to 0.07% were calculated for all timeframes, except those with insufficient data. Additionally, areas for the percentages 0.03% and 0.04% were calculated if there was no or not enough data for 0.05%. "-" indicates that no area was calculated for the given percentage.

Timeframe	0.03%	0.04%	0.05%	0.06%	0.07%
01-07-2020 to 31-12-2020	-	-	36 885 886.02	10 542 228.96	2 312 248.34
01-01-2021 to 30-06-2021	-	-	10 551 441.88	11 365 602.93	9 314 748.23
01-07-2021 to 31-12-2021	-	-	10 263 612.22	8 872 031.57	1 421 402.67
01-01-2022 to 30-06-2022	-	-	12 782 436.43	11 076 140.14	1 586 966.96
01-07-2022 to 31-12-2022	-	-	9 489 724.31	2 234 844.27	851 069.30
01-01-2023 to 30-06-2023	-	-	2 660 553.45	785 940.10	301 261.88
01-07-2023 to 31-12-2023	8 518 849.19	1 385 360.28	78 849.13	-	-
01-01-2024 to 30-06-2024	Insufficient Data				
01-07-2024 to 31-12-2024	1 719 766.05	32 978.41	60 957.81	-	-

Table A.22.: Size of the arctic auroral zone (latitudes between 50° and 90° N) in square degrees according to different pixel percentages in 12 months intervals. Areas for the percentages of 0.05% to 0.07% were calculated for all timeframes, except those with insufficient data. Additionally, areas for the percentages 0.03% and 0.04% were calculated if there was no or not enough data for 0.05%. "-" indicates that no area was calculated for the given percentage.

Timeframe	0.03%	0.04%	0.05%	0.06%	0.07%
01-07-2020 to 31-12-2020	-	-	1851.73	813.38	484.75
01-01-2021 to 31-12-2021	Insufficient Data				
01-01-2022 to 31-12-2022	-	-	956.92	272.10	221.52
01-01-2023 to 31-12-2023	638.94	508.52	132.70	3.35	-
01-01-2024 to 31-12-2024	Insufficient Data				

Table A.23.: Size of the arctic auroral zone (latitudes between 50° and 90° N) in square kilometres according to different pixel percentages in 12 months intervals. Areas for the percentages of 0.05% to 0.07% were calculated for all timeframes, except those with insufficient data. Additionally, areas for the percentages 0.03% and 0.04% were calculated if there was no or not enough data for 0.05%. "-" indicates that no area was calculated for the given percentage.

Timeframe	0.03%	0.04%	0.05%	0.06%	0.07%
01-07-2020 to 31-12-2020	-	-	36 885 886.02	10 452 228.96	2 312 248.34
01-01-2021 to 31-12-2021	Insufficient Data				
01-01-2022 to 31-12-2022	-	-	12 617 106.68	8 427 600.33	1 022 533.06
01-01-2023 to 31-12-2023	11 565 542.76	2 666 248.93	422 869.82	50 478.23	-
01-01-2024 to 31-12-2024	Insufficient Data				

Table A.24.: Size of the arctic auroral zone (latitudes between 50° and 90° N) in square degrees according to different pixel percentages during 4.5 years of observation. "-" indicates that no area was calculated for the given percentage.

Timeframe	0.03%	0.04%	0.05%	0.06%	0.07%
01-07-2020 to 31-12-2024	3085.69	845.05	499.96	110.47	-

Table A.25.: Size of the arctic auroral zone (latitudes between 50° and 90° N) in square kilometres according to different pixel percentages during 4.5 years of observation. "-" indicates that no area was calculated for the given percentage.

Timeframe	0.03%	0.04%	0.05%	0.06%	0.07%
01-07-2020 to 31-12-2024	44 707 135.31	11 663 436.46	2 477 783.17	236 622.52	-

Table A.26.: Coordinates of the northernmost, southernmost, easternmost and westernmost points of the arctic auroral zone (latitudes between 50° and 90° N) in 6-month intervals for the respective pixel percentage contours. "-" indicates that no coordinates were calculated for the given percentage.

	0.03%				0.04%				0.05%				0.06%				0.07%			
Timeframe	N	E	S	W	N	E	S	W	N	E	S	W	N	E	S	W	N	E	S	W
01-07-2020 to 31-12-2020	-	-	-	-	-	-	-	-	84.74	180.00	50.00	-180.00	83.09	180.00	50.00	-180.00	69.04	171.84	50.00	-177.70
01-01-2021 to 30-06-2021	-	-	-	-	-	-	-	-	84.82	180.00	50.00	-180.00	73.38	180.00	50.00	-180.00	69.20	180.00	50.00	-180.00
01-07-2021 to 31-12-2021	-	-	-	-	-	-	-	-	83.70	180.00	50.00	-180.00	70.34	180.00	50.00	-180.00	68.03	-79.92	50.00	-178.54
01-01-2022 to 30-06-2022	-	-	-	-	-	-	-	-	72.91	180.00	50.00	-180.00	69.99	180.00	50.00	-180.00	68.66	166.49	50.00	-163.72
01-07-2022 to 31-12-2022	-	-	-	-	-	-	-	-	-	-	-	-	68.74	180.00	50.00	-180.00	63.76	-68.62	50.00	-166.10
01-01-2023 to 30-06-2023	-	-	-	-	-	-	-	-	-	-	-	-	63.26	-66.88	50.00	-168.86	58.54	-90.51	50.00	-144.19
01-07-2023 to 31-12-2023	68.88	180.00	50.00	-180.00	64.05	-71.84	50.00	-166.10	58.32	-105.60	50.00	-138.81	-	-	-	-	-	-	-	-
01-01-2024 to 30-06-2024	53.30	-99.52	50.00	-123.21	-	-	-	-	-	-	-	-	-	-	-	-	-	-	-	-
01-07-2024 to 31-12-2024	68.32	164.32	50.00	-174.72	54.69	-97.63	50.00	-122.96	52.73	-113.93	50.42	-118.09	-	-	-	-	-	-	-	-

Table A.27.: Coordinates of the northernmost, southernmost, easternmost and westernmost points of the arctic auroral zone (latitudes between 50° and 90° N) in 12-month intervals for the respective pixel percentage contours. "-" indicates that no coordinates were calculated for the given percentage.

	0.03%				0.04%				0.05%				0.06%				0.07%			
Timeframe	N	E	S	W	N	E	S	W	N	E	S	W	N	E	S	W	N	E	S	W
2020	-	-	-	-	-	-	-	-	84.74	180.00	50.00	-180.00	83.09	180.00	50.00	-180.00	69.04	171.87	50.00	-177.70
2021	Insufficient data																			
2022	-	-	-	-	-	-	-	-	70.68	180.00	50.00	-180.00	69.16	180.00	50.00	-180.00	63.71	-68.38	50.00	-164.01
2023	69.94	180.00	50.00	-180.00	65.15	177.91	50.00	-177.11	63.49	-74.79	50.00	-161.22	51.53	-103.38	50.00	-108.15	-	-	-	-
2024	Insufficient data																			

Table A.28.: Coordinates of the northernmost, southernmost, easternmost and westernmost points of the arctic auroral zone (latitudes between 50° and 90° N) during 4.5 years of observation for the respective pixel percentage contours. "-" indicates that no coordinates were calculated for the given percentage.

	0.03%				0.04%				0.05%				0.06%				0.07%			
Timeframe	N	E	S	W	N	E	S	W	N	E	S	W	N	E	S	W	N	E	S	W
01-07-2020 to 31-12-2024	87.67	180.00	50.00	-180.00	70.51	180.00	50.00	-180.00	64.75	-64.41	50.00	-174.35	53.50	-73.68	50.00	-119.03	-	-	-	-